Development of FTIR tomography for thermal-source imaging of 3D biochemical distributions in micro-samples of cells and fibers

BY

CATHERINE RUI JIN FINDLAY

A thesis submitted to the Faculty of Graduate Studies of

The University of Manitoba

in partial fulfillment of the requirements for the degree of

DOCTOR OF PHILOSOPHY

Department of Chemistry

University of Manitoba

Winnipeg, Manitoba, Canada

May 12, 2018

Table of Contents

List of Tables

List of Figures

Abstract

FTIR microspectroscopy is an established 2D hyperspectral imaging technique with which to measure distributions of biochemical functional groups (e.g. lipids, proteins, nucleic acids) within organic samples. The emergence of FTIR microtomography, first reported by Martin et al. (2013), extends image resolution to three spatial dimensions (3D). This thesis describes a generalized, laboratory-scale approach to 3D imaging with FTIR microtomography. A modified method to handle a variety of micro-sample morphologies, i.e. longer fibres (spider silk) and larger globular cells (diatoms and buccal cells), was required.

Towards this end, a motorized sample holder with increased flexibility was designed at the University of Manitoba for the collection of thermal source FTIR microtomographic data sets. A tomography accessory for microscopes (US patent No. US15065379; June, 2017) was prototyped, and assessed via imaging of a custom built size-standard phantom. The tomography accessory was further used to collect data illustrating niche applications of FTIR microtomography.

The 3D resolved FTIR spectra (voxel spectra) of a fiber and two cell types of interest, namely artificial spider silk, human buccal epithelial cells and Arctic sea ice diatoms, were characterized. The 3D distribution and abundance of compounds were reconstructed while maintaining a sub-cellular level of resolution in all three spatial dimensions. Specifically, the embedding of the silk fiber in a refractive-index matched transparent matrix reduced scatter increased the quality of 3D FTIR images. Additional fine details of these silk specimens not observable with 2D FTIR images, e.g. double-stranded morphological substructure, were captured with FTIR microtomography. The application of a coating was non-destructive and reversible. Further polarization contrast FTIR microtomographic imaging of the coated spider silk revealed sub-volumes within the fiber with differing responses to polarized IR light.

List of Published Papers

I. **In situ imaging of usnic acid in selected *Cladonia* spp. by vibrational spectroscopy,** C. R. Liao, M.D. Piercey-Normore, J.L. Sorensen, and K.M. Gough, Analyst, 135(12):3242–3248, 2010.

II. **Tissue acquisition and storage associated oxidation considerations for FTIR microspectroscopic imaging of polyunsaturated fatty acids,** D.M. Stitt, M.Z. Kastyak-Ibrahim, C.R. Liao, J. Morrison, B.C. Albensi, and K. M. Gough, Vibrational Spectroscopy, 60:16–22, 2012.

III. **Synchrotron FTIR reveals lipid around and within amyloid plaques in transgenic mice and Alzheimer's disease brain,** C.R. Liao, M. Rak, J. Lund, M. Unger, E. Platt, B.C. Albensi, C.J. Hirschmugl, and K.M. Gough, Analyst, 138:3881–1887, 2013.

IV. **Rapid biodiagnostic *ex vivo* imaging at 1 micron pixel resolution with thermal source FTIR FPA,** C R. Findlay, R. Wiens, M. Rak, J. Sedlmair, C. J. Hirschmugl, J. Morrison, CJ Mundy, M. Kansiz, and K.M. Gough, Analyst, 140:2493–2503, 2015.

V. **High spatial resolution (1.1 μm and 10 nm) polarization contrast imaging reveals pre-rupture disorder in damaged tendon,** R.A. Wiens, C. R. Findlay, S.J. Baldwin, L. Kreplak, and M.J. Lee, S.P. Veres, K.M. Gough, Faraday Discussions 187, 555-573, 2016.

VI. **FTIR imaging analysis of cell content in arctic sea-ice diatom taxa during the spring bloom near Cambridge Bay, Nunavut, Canada,** N. Pogorzelec, CJ Mundy, C.R. Findlay, K. Campbell, A. Delaforge, S. Rysgaard, K.M Gough. Marine Ecology Progress Series 569, 77-88, 2017

VII. **Thermal source Fourier Transform Infrared microtomography applied to Arctic sea ice diatom cells,** C.R. Findlay, J. Morrison, C.J. Mundy, J. Sedlmair, C.J. Hirschmugl, and K.M. Gough. Analyst, 142(4):660–669, 2017.

List of Abbreviations

3×Tg . . . . . triply transgenic mouse model of Alzheimer's disease

AD . . . . . Alzheimer's Disease

AKA . . . . . Also Known As

ATR . . . . . Attenuated Total Reflection

CAT . . . . . Computer Aided Tomography

CEOS . . . . . Centre for Earth Observation Studies

CCW . . . . . Counter Clock-Wise

CW . . . . . Clock-Wise

DIY . . . . . Do-It-Yourself

DPI . . . . . Dots Per Inch

FBP . . . . . Filtered Back-Projection

FPA . . . . . Focal Plane Array

FOV . . . . . Field of View

FSW . . . . . Filtered Seawater

FTIR . . . . . Fourier Transform Infrared

ICE-CAMPS . . . . . Ice Covered Ecosystem-CAMbridge Bay Process Study

IR . . . . . Infrared

IRENI . . . . . Infrared Environmental Imaging beamline

IRRAS . . . . . Infrared Reflection-Absorption Spectrometry

LB . . . . . Left Baseline

LE . . . . . Left Edge

LN2 . . . . . liquid nitrogen

MCT . . . . . Mercury Cadmium Telluride

NA . . . . . Numerical Aperture

NEMA . . . . . National Electrical Manufacturer Association

ONA . . . . . Observed Nuclear Area

PSM . . . . . Polystyrene Microsphere

PUFA . . . . . Poly Unsaturated Fatty Acids

PVA . . . . . Polyvinyl Alcohol

RB . . . . . Right Baseline

RE . . . . . Right Edge

Res. Pro. . . . . Agilent Resolutions Pro^{TM}

Rev. . . . . Revolutions

RMieS . . . . . Resonant Mie Scattering

U of M . . . . . The University of Manitoba

sFTIR . . . . . Synchrotron Source Fourier Transform Infrared

SRC . . . . . Synchrotron Radiation Centre

SymCH_2 . . . . . Symmetric CH_2 Stretch

TPI . . . . . Turns Per Inch

Acknowledgments

I would like to thank the following professionals who made this thesis possible:

My thesis advisor, Dr. Kathleen M. Gough, for initiating, approving, editing and supervising this research, and for her mentorship, support and consummate scientific skills.

Past and current members of the research group: Dr. Margaret Rak, Dr. Richard Weins, Dr. Marzena Kastyak, Alexandra Ciapala and Nicole Pogorzelec. Further thanks to Nicole for assistance with the preparation of Figure 5.1.

My advisory and internal examining committee: Dr. Philip Hultin, Dr. Jason Morrison, and Dr. Joseph O'Neil, for their advice and editorial comments on this thesis.

External examiner: Dr. Christian Pellerin, Chemistry, Université de Montréal.

Dr. Carol Hirschmugl, Dr. Julia Sedlmair, and Ebrahim Aboualizadeh for training and discussion at the former Synchrotron Radiation Center (SRC) regarding tomography, wire and microloop mounting and imaging of diatoms and spider silk at the Infrared Environmental Imaging (IRENI) beamline.

Dr. Mike Martin and Dr. Hans Bechtel of the Advanced Light Source (ALS, Lawrence Berkeley National Laboratory, USA) for discussions regarding FTIR microtomography and their mature and open spirit of sharing.

Diatom Project: Dr. C.J. Mundy, and Karley Campbell, and Auralie Delaforge, members of the Centre for Earth Observation Science, University of Manitoba, who enabled the Ice Covered Ecosystem-Cambridge Bay Process Study (ICE-CAMPS) 2014 diatom harvest.

Spider Silk Project: Dr. Jan K. Rainey, and Nathan Weatherbee-Martin of Dalhousie University, Nova Scotia, for spinning the artificial spider silk and providing assistance with the method section of the spider silk chapter.

Buccal Cell Project: Dr. Sabine Mai, University of Manitoba.

The administrative staff of the Chemistry Department, including Keith Travis, Sharon Mullen, Grace Ntungo, and Tricia Lewis.

Many thanks go to family: my dear parents (David and Simfay Liao), brothers (Timothy and Stephen Liao), husband (Stuart Findlay, arachnophobe) and mother-in-law (Patti Findlay), for their wisdom and patience. Thank you to Stephen for providing instruction regarding Adobe Illustrator and LaTex software, used for figure creation and thesis typesetting, respectively. Thank you to my father, David, for instruction during the machining of metal connecting pieces for tomography accessory prototypes.

Accessibility Note

Colour-blindness friendly or monotone print compatible versions of the images in this thesis can be made available upon request. Please send your requests to cathliao at gmail.com.

Chapter 1. Introduction

1.1 Infrared light

Light propagates through space as radiant waves with synchronized oscillations of electric and magnetic fields. Photons are the quanta of electromagnetic radiation and these elementary particles have energies that depend only on frequency. The energy of a photon, E, is given by the equation:

$$E = hf = h\frac{c}{\lambda} \tag{1.1}$$

where h is Plank's constant, f is the frequency associated with the light, c is the speed of light, and λ is wavelength. The spatial frequency of infrared light is reported in terms of wavenumber, $\bar{\nu}$, the number of waves in a unit distance (typically cm^{-1}) where $\bar{\nu} = \frac{1}{\lambda}$. (Atkins and de Paula, 2007).

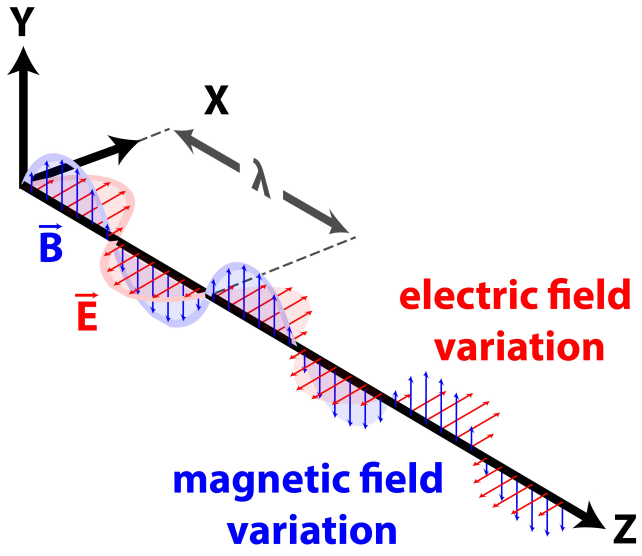

Figure 1.1: Electric (**E**), and magnetic (**B**), fields associated with a photon propagating through 3D space **(X, Y, Z)**, moving in the direction of Z at the speed of light. The wavelength, λ, is the distance between two nodes. Only one polarity of light is shown here for clarity. Artwork is based on (Atkins and de Paula, 2007) and other common depictions.

The electromagnetic spectrum includes infrared light which has energies lower than the nominal red visible region and energies higher than the microwave region (Figure 1.2). The mid-infrared region is a smaller region of energies with wavenumbers between 4000 and 200 cm^{-1} that lies within the larger infrared region (Atkins and de Paula, 2007).

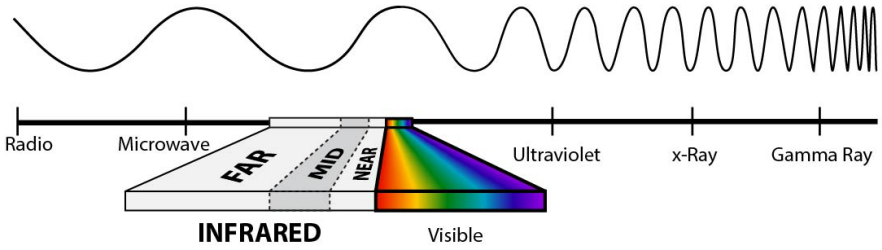

Figure 1.2: Electromagnetic spectrum. Artwork by author is based on (Atkins and de Paula, 2007) and other common depictions.

1.2 Properties of Matter and Interactions with Light

1.2.1 Vibrational Energy Levels

Molecular vibrations are periodic atomic motions that cause changes in the nuclear positions. A vibration can affect the separation of positive and negative electrical charges within a molecule, and create a change in the net dipole moment. A molecular vibration can absorb energy and increase in amplitude if the oscillating electric fields associated with an incident ray of light couple to the fluctuation in the dipole moment.

Atoms in molecules can be modeled as masses on springs (Figure 1.3) to simulate the repulsive and attractive forces they exert upon one another (Griffiths and De Haseth, 1986). In the harmonic approximation, vibrational energy, E_{v}, is given by the equation:

$$E_{\mathrm{v}} = (\mathrm{v} + \frac{1}{2})\, hf \tag{1.2}$$

where v is the vibrational quantum number, h is the Planck constant, and f is frequency.

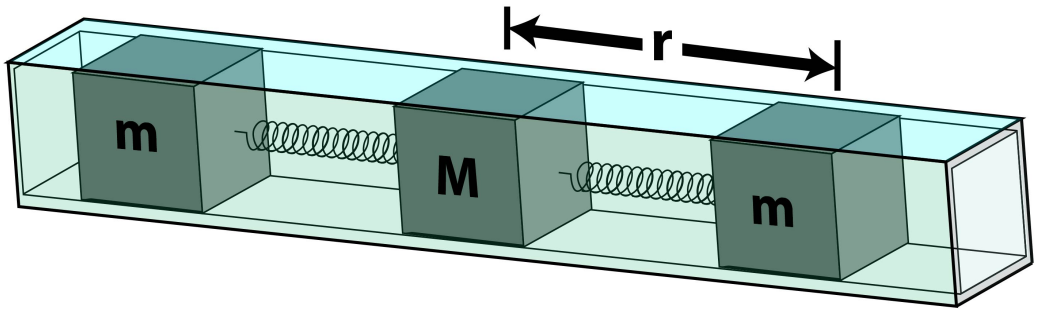

Figure 1.3: A simple mechanical system. Two objects with mass m and one central object with mass, M, are connected by springs and lie within a perfectly frictionless case – a square tube in which they can slide with piston action. The distance, r, is the equilibrium bond length between the centers of the two masses. Artwork by author based on a line-diagram found in Woodward (1972).

The vibrational energy levels are equally spaced apart in the harmonic approximation.

The actual vibrational energy levels of a molecule more closely resemble those of an anharmonic oscillator (Figure 1.4). The energy levels in a molecule become more closely spaced as v increases, until a continuum of energies is reached at virtual energy levels.[1] The energy level separation, ΔE is given by:

$$\Delta E = E_2 - E_1 \tag{1.3}$$

The energy of a photon must match the vibrational energy separation in order for excitation to a higher vibrational energy state to occur. Thermal energy, equal to kt, the product of the Boltzmann constant, k, and the temperature, t, is relatively low at room temperature. Consequently, the majority of molecules exist in their ground vibrational state. Frequencies for the transitions from the ground state, v $= 0$, to the first excited state, v $= 1$, constitute fundamental vibrational modes. As well, IR light can also excite combination and overtone vibrational modes and give rise to additional bands of absorbance in the FTIR spectra of molecules (Atkins and de Paula, 2007).

[1] A 'virtual state' is a type of quantum state that is so short-lived as to be unobservable. Raman spectroscopy involves excitation from the ground state to a virtual energy state.

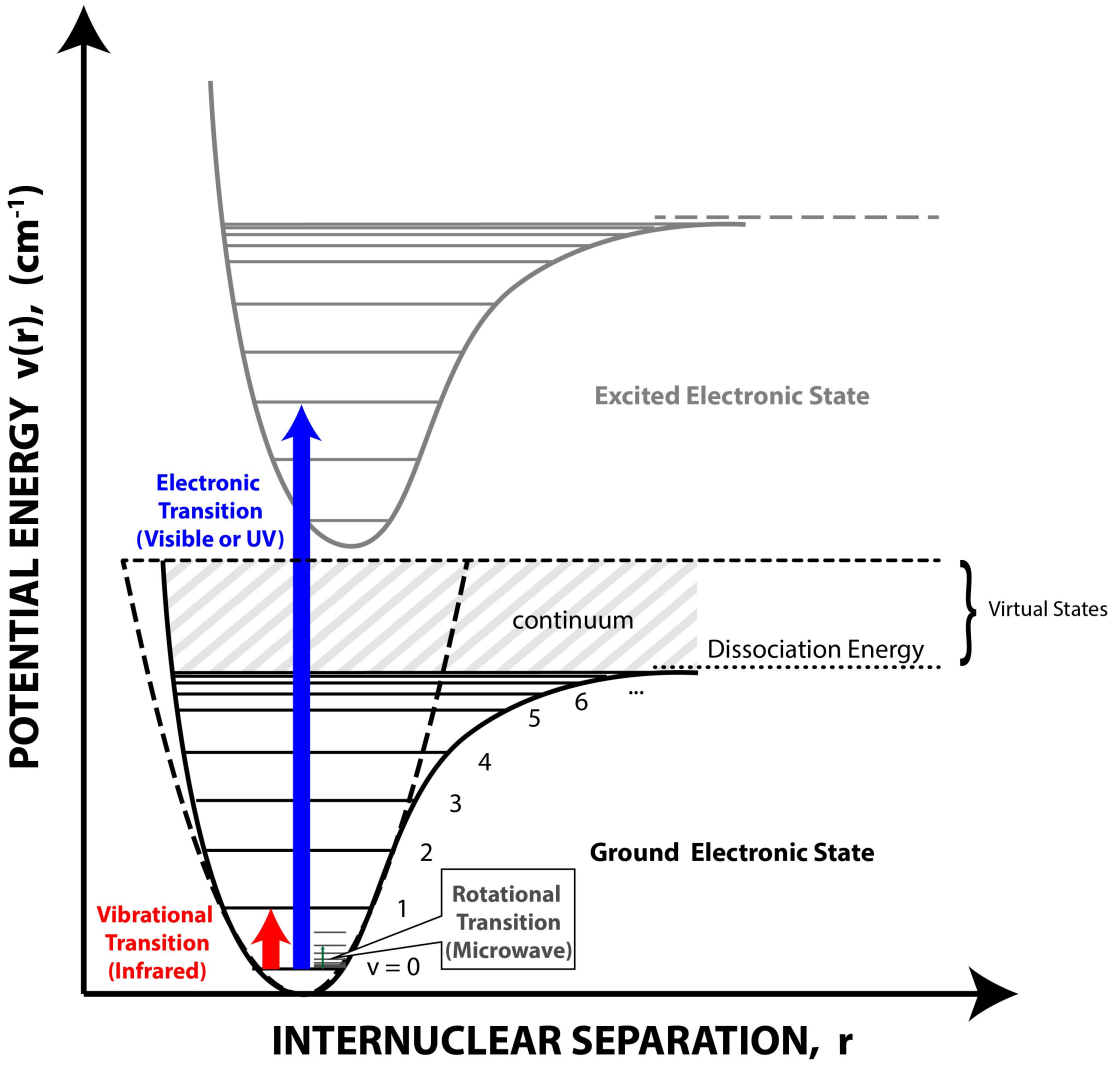

Figure 1.4: Transitions between energy levels of a molecule. Solid and dashed curves indicate potential energy associated with an anharmonic and harmonic oscillator, respectively. Artwork by author is based on Atkins and de Paula (2007), and other depictions.

Normal Modes of Vibration

The number of normal modes of vibration for a given molecule depends on two factors: 1) the degrees of freedom that exist for the atoms that comprise a molecule (Table 1.1) and 2) the molecular geometry. Each of the atoms (N in number) in a molecule can move along a set of 3 Cartesian axes defining 3D space. Of the $3N$ motions that are possible, only 3 involve centre-of-mass motion along the axes and therefore constitute molecular translations. Additionally, a non-linear molecule can rotate around all 3 Cartesian axes. In contrast, a linear molecule can only measurably rotate around 2 Cartesian axes. This is due to the inability of linear molecules to measurably rotate around their principal symmetry axis. Vibrational modes constitute the remaining degrees of freedom; thus, the number of normal modes of vibration for linear molecules is $3N-5$. In contrast, non-linear molecules have $3N-6$ normal modes of vibration (Atkins and de Paula, 2007).

Table 1.1: Degrees of freedom for linear and non-linear molecules.

Type	Molecular Geometry	
	Linear	Non-Linear
Translational	3	3
Rotational	2	3
Vibrational	3N - 5	3N - 6
Total Number	3N	3N

Normal modes of vibration can involve stretching, bending or torsion. Stretching can be symmetric or asymmetric. Bending and torsion includes twisting, wagging, scissoring and rocking motions (Griffiths and De Haseth, 1986).

1.2.2 Beer Lambert Absorption

Semi-quantitative analysis of concentration is possible when the attenuation of light by an absorptive material adheres to Beer–Lambert–Bouguer Law (Beer's Law). Beer's Law

states that the absorbance, A, is given by the following equation:

$$A = log(\frac{I_0}{I}) = \epsilon cl \tag{1.4}$$

where A is the absorbance, I_0 is the intensity of the incident light, I is the intensity of radiation exiting the sample, ϵ is the molar attenuation coefficient, l is the path-length, and c is concentration.

The attenuation coefficient[2], μ, is given by:

$$\mu = \epsilon c \tag{1.5}$$

Beer's Law can also be stated in terms of μ:

$$A = log(\frac{I_0}{I}) = \mu l \tag{1.6}$$

and we can find the equation for μ from 1.6 after taking the logarithm and rearranging:

$$\mu = \frac{1}{l} log(\frac{I_0}{I}) \tag{1.7}$$

After rearranging equation 1.6:

$$log(I_0) - log(I) = \mu l \tag{1.8}$$

$$log(I) = log(I_0) - \mu l \tag{1.9}$$

$$I = 10^{log(I_0)+(-\mu l)} \tag{1.10}$$

[2]The attenuation coefficient is not equal to the *molar* attenuation coefficient

$$I = 10^{log(I_0)} * 10^{-\mu l} \tag{1.11}$$

$$I = I_0 10^{-\mu \ell} \tag{1.12}$$

in order to find the equation for I (Seeram, 2015). The final form of the equation becomes important later to descriptions of tomography.[3]

1.2.3 Refractive Index

Refractive index is a dimensionless ratio of the velocity of light in a vacuum to the velocity in a medium. The complex refractive index, $\tilde{n}(\tilde{v})$, can be expressed as a function of wavenumber, $\bar{v}$.

$$\tilde{n}(\bar{v}) = n(\bar{v}) + i\kappa(\bar{v}) \tag{1.13}$$

where $n(\bar{v})$ is the real component of the refractive index which indicates the phase velocity. The $\kappa(\bar{v})$ is the imaginary component of the refractive index (the extinction coefficient), which indicates how much light is attenuated by a material.

The real component of refractive index can be used to describe light propagation in non-absorbing materials or negligibly absorbing materials. However, there are frequency bands where a wave is not purely propagating but is also attenuated. The addition of the complex component to the refractive index more accurately describes light propagation in absorbing materials.

Thus, refractive index increases across absorption bands for typical organic and inorganic molecular vibrations due to the addition of an overall positive contribution stemming from the complex component (Griffiths and De Haseth, 1986). This relationship between

[3]Note that I is not equal to a natural logarithm, $I_0 \mathrm{e}^{-\mu\ell}$, a published error (Seeram, 2015). The rearrangement of equations 1.6 to 1.12 is quite basic, but is shown to resolve the discrepancy with the text by Seeram (2015).

absorbance and refractive index becomes very important to the optical distortion observed in applications shown in later chapters.

1.2.4 Scattering

Scattering results from the combined effects of reflection, refraction and diffraction. The extent to which scattering may occur will be influenced by the optical properties of the sample, including refractive index. When mid-IR light is incident on the interface of an optically rare (low refractive index) and an optically dense (high refractive index) medium, there may be scattering of light (Atkins and de Paula, 2007).

The scattering of electromagnetic radiation by a spherical object, known as Mie scattering. It occurs when the scattering spherical particles have diameters that are comparable to wavelengths of incident radiation. The Lorenz-Mie-Debye solution to Maxwell's equations is used to calculate how much light at each wavelength is scattered from a sphere with a given diameter. The amount of light scattered from a sphere is not equal for all wavelengths. The resulting broad spectral baseline effects (Griffiths and De Haseth, 1986) can complicate the relation of spectra to concentration via Beer's Law (Bassan et al., 2009).

Diffraction manifests when light encounters an obstacle or a narrow aperture. In effect, light bends past opening and around edges. This occurs because of the way light transmitted through a medium (including the medium at the edge of an obstacle) propagates. The Huygens-Fresnel principle of wave propagation describes every point on a wavefront as a source of a secondary spherical wavelet. Wavelets interfere constructively and destructively with each other, and form fringed patterns, such as the Airy pattern (described later).

The finest sample detail that can be spatially resolved with far-field microscopy is no smaller than the diffraction limited spatial resolution.

$$\text{spatial resolution} = \frac{0.61\lambda}{n \sin(\theta)} \tag{1.14}$$

The denominator, $n \sin(\theta)$, is the numerical aperture of the optical system, and θ' refers to the maximal half-angle of a cone of light accepted through a lens.

The point spread function (PSF) is the response of an imaging system to a point source or point object, and can be impacted by diffraction. The Airy Pattern is the diffraction-limited PSF formed on a focal plane after light from a point source or point object is passed through a small circular aperture. The Airy pattern contains a bright central region known as the Airy disk, which is surrounded by concentric rings of decreasing intensity (Figure 1.5).

Rayleigh Criterion The Rayleigh criterion defines the requirements for two diffracting point objects to be considered resolved from one another. The Rayleigh criterion is met when the maximum of an Airy pattern lies on the first minimum of a second Airy pattern. The maxima of the two PSFs in an image must have a local minimum between them that dips to 26.3% of the maximal height in order to be considered diffraction-limited. At this point, the first minimum of one Airy pattern coincides with the maximum of another Airy pattern.[4]

[4] Among the current best observations in the literature is the resolution at the diffraction-limit achieved with wide-field FTIR microscopy at IRENI (Nasse et al., 2011b).

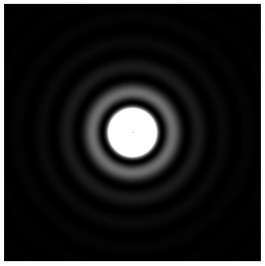

Figure 1.5: Airy-disk generated with the Matlab™ default implementation of a first order Bessel function, 'besselj()' using a Fraunhofer diffraction script (Rao, 2014).

1.3 Infrared Spectroscopy

Infrared absorbance spectroscopy is a subtype of vibrational spectroscopy. A plot of the measured amount of light absorbed (absorbance) versus wavenumber (proportional to photon energy) constitutes an infrared spectrum. Chemical functional groups absorb in characteristic regions of the infrared spectrum. Chemical species can be classified by the number and types of chemical functional groups present. The group frequencies can be the basis for structural analysis of a molecule.

Spectroscopists can conduct semi-quantitative chemical analysis of samples by measuring the distinctive signatures present in recorded spectra of heterogeneous mixtures. Features such as the quality of the spectral baseline, and multiple correlated bands from individual contributing molecules are diagnostic (Griffiths and De Haseth, 1986).

1.3.1 Non-destructive Illumination

Infrared spectroscopy is a non-destructive technique due to the properties of infrared light. The dosage levels of infrared radiation involved in collecting spectra is insufficient to induce ionization, chemical reaction, significant thermal warming or otherwise cause damage to an exposed sample or analyte (Stuart, 2004).

1.3.2 Applicability to biological samples

FTIR spectrochemical imaging of various types of cells is possible. Some examples from our group include lichen tissue (Liao et al., 2010), fungal hyphae (Szeghalmi et al., 2007), brain tissue from murine models of Alzheimer's Disease (AD) (Gallant et al., 2006), scar tissue (Gough et al., 2003) and diatoms (Pogorzelec et al., 2017). The collected spectral features of common biochemicals are well discussed in the doctoral thesis by Rak (2007). Peak parameters and band assignments utilized in this thesis are based on these citations.

1.3.3 Instrumentation

Early infrared spectroscopists employed dispersive instruments; however, modern Fourier Transform Infrared (FTIR) spectroscopy is accomplished with spectrometers based on interferometry. Components will be briefly described in the following sections.

Thermal Light-Sources

Globars are electrically heated silicon carbide rods found in benchtop IR instruments. The light emitted from a globar source is approximately black-body radiation. The mid-infrared region of the polychromatic light is suitable for infrared absorption spectroscopy. Globars have relatively low brilliance compared to synchrotron light sources (Griffiths and De Haseth, 1986).

The Michelson Interferometer

Wavelengths of infrared light that have passed through a sample imaging subject are directed to a Michealson interferometer. Upon striking a beam-splitter, a single beam of light diverges and heads down two paths. One path brings the light to a fixed mirror, while the other has a moving mirror. Light from both paths is reflected back toward the beam-splitter where they combine. The beams travel different distances depending on the position of the moving mirror. The displacement between the mirrors is termed 'retardation'. The absorbance spectrum, collected as a function of mirror retardation, is translated into the frequency domain upon applying a Fourier transform. The multiplexed measurement of all of the wavelengths of light simultaneously at the interferometer achieves higher signal to noise ratio: the Felgett advantage (Griffiths and De Haseth, 1986). [5]

[5]The Michelson interferometer is shown in Figure 2.1 of the text by Griffiths and De Haseth (1986).

1.3.4 2D FTIR Microspectroscopy

FTIR microspectroscopy is an imaging technique that combines the 2D spatial resolution of microscopy with the molecular-level chemical information of FTIR vibrational spectroscopy. Microscopic quantities of analyte can be captured in a spectrochemical image. The non-destructive nature of FTIR imaging makes further testing or correlated imaging feasible.

Thermal-source microscopes equipped with high magnification optics and high numerical aperture Schwarzschild lenses are capable of higher resolution[6] and produce spectral images composed of micron-sized pixels (Findlay et al., 2015).[7]

Schwarzschild Objective Lenses

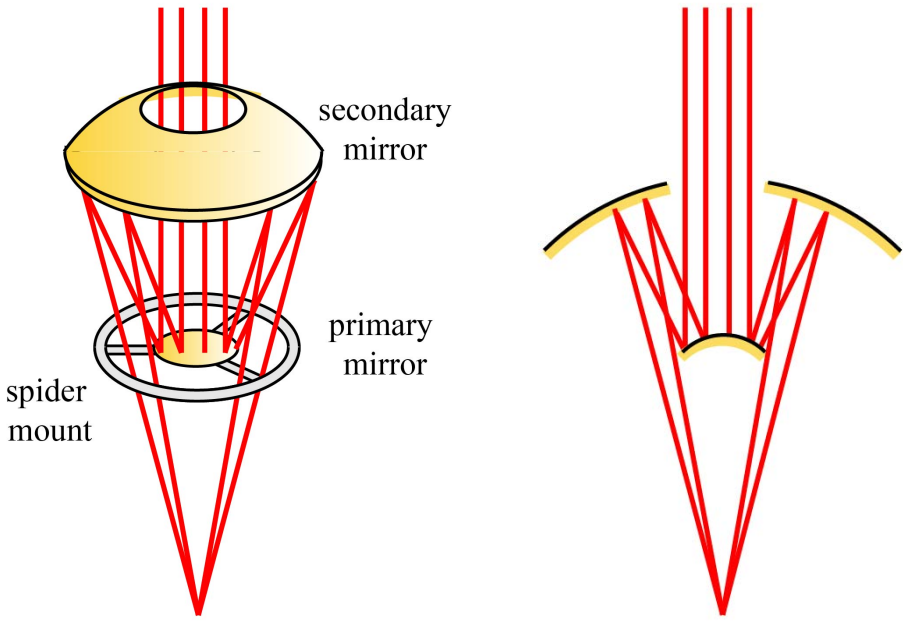

(A) 3D view **(B)** side view

Figure 1.6: Diagrammatic representation of Schwarzschild objective lens components. Artwork by author is based on images in (Atkins and de Paula, 2007) and other common depictions. The primary mirror here is the one struck by light first.

[6] As a rule of thumb, the resolution is approximately double the pixel size

[7] The specific spectrometer employed for 1.1 μm pixel data in this thesis is detailed later in Section 2.1.1.

Silica-based glass lenses for focusing visible light are not appropriate for infrared optics, as they highly absorb infrared light. Rather, Schwarzschild objective lenses are employed for FTIR microspectroscopy (Figure 1.6). Infrared reflective surfaces (e.g. gold- or aluminum-coated mirrors) can effectively focus infrared light. Higher numerical aperture Schwarzschild lenses have a larger acceptance cone and improved ability to gather light.

Schwarzschild objective lenses can be used alone, or be paired with a Schwarzschild condenser lens (Figure 1.7, Figure 2.2). When an FTIR microscope is operated in reflection mode, focused light coming down from the objective reflects back upward off the surface of a sample. In transmission mode, light is transmitted through the sample at the focal point and travels downwards to a Schwarzschild condenser lens. Infrared tomography makes use of the transmission geometry (Martin et al., 2013). The ray diagram in Figure 1.7[8]

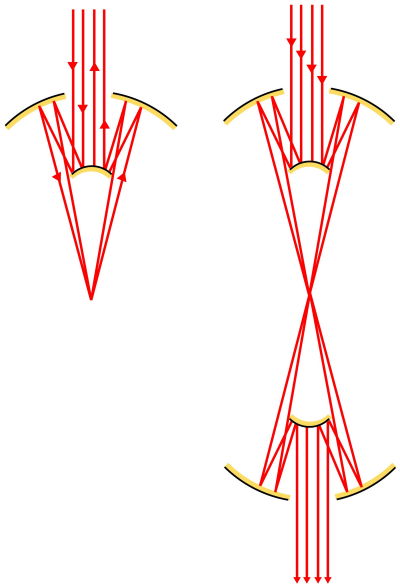

(A) Reflection **(B)** Transmission

Figure 1.7: Schwarzschild lens ray diagrams. Infrared light geometry during the passage through the Schwarzschild objectives of an infrared microscope set to one of two sample measurement modes (A, B).

does not perfectly resemble the parallel or fan beam geometries (illustrated in Figure 3.13)

[8] A ray diagram is a diagram that traces the path that light takes.

traditionally used with tomography.

FTIR spectrochemical imaging in 2D involves the acquisition of spatially resolved FTIR spectra. A FPA detector may be employed without stage movement for single-tile images or combined with raster scanning to generate mosaic images.

High Magnification Optics

Modern commercially-available microspectrometers may include accessory high magnification optics that can be flipped in and out of the beam path. The magnification of the intermediate optics, as well as the objective lens, adds to the total system magnification.

Beam Expander

Magnifying FTIR images can be accomplished with beam expander optics that increase the diameter of a beam. (Figure 1.8) [9] The outside edges of the expanded beam do not fall on the area of the detector, as they would without the beam expander, due to the increased diameter of the beam. Only the central region forms a focused image with enhanced magnification. This is perhaps a side benefit, as the central region of the beam creates the highest quality images (Bhargava and Levin, 2008).

Globar light sources employed in bench-top systems have relatively low brilliance. The use of an additional beam expander optic and the sacrifice of light at the edges of the infrared beam is made feasible by high numerical aperture Schwarzchild lenses which help compensate for this loss in bench-top systems by efficiently collecting the remaining light.

Microscope Stage Considerations

FTIR microscope stages are designed for precision motion, and have stepper motors and fine gears. Commercially available FTIR microscope systems feature software-controlled, automated stage stitching (mosaicing) of multiple FPA tiles.

[9] An expansion ratio of 2 is shown in for illustrative purposes. An expansion ratio of 5 (i.e. 5$\times$ magnification) could be expected for the system employed in Section 3.2 and Chapter II.

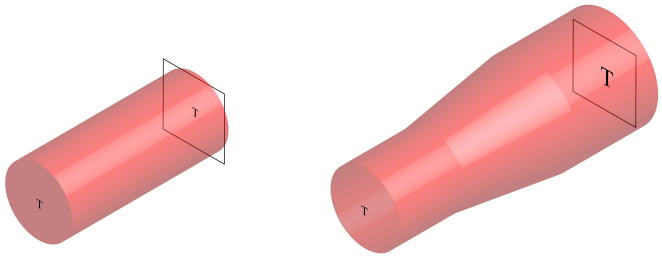

(A) No Expansion **(B)** Expansion

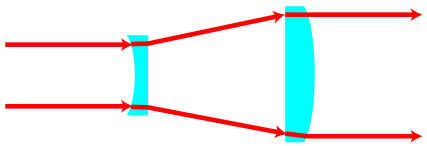

(C) Expansion Ray Diagram

Figure 1.8: Effect of beam expander. A beam of infrared light **(red)** carrying information about a sample (letter 'T'), traveling through **(A)** no beam expander or **(B)** a beam expander with an expansion ratio of 2. The light forms an image upon striking a detector area (black box). (C) Ray diagram of light passing through infrared transparent CaF_2 or BaF_2 lenses **(blue)** within the beam expander optic.

Mechanical parts naturally experience wear with normal motion resulting in loss of precision and image mosaic artifacts. Many stages are not designed for easy or frequent removal from the microscope. Such stages have a maximum recommended load[10]. Excessive mass loaded onto the stage can result in permanent damage.

Typical Processing of 2D FTIR Images

The raw data generated by the instrument is in the form of a hyperspectral cube (Figure 1.9), with each spectrum (Figure 1.11) associated with spatial coordinates. For every spectrum, the absorbance values for a band may be integrated to calculate a peak area (Figure 1.10). The value for the peak area is the input for a colour mapping function and a colour is assigned to a pixel in a 2D FTIR false-colour image (Figure 1.13) This is done for each pixel in a 2D image. On top of univariate methods, there are multivariate methods that can

[10]'Load' here refers to mass placed onto the microscope stage.

be applied, in order to quantify chosen features in a pixel spectrum, and then display the result for the area imaged.

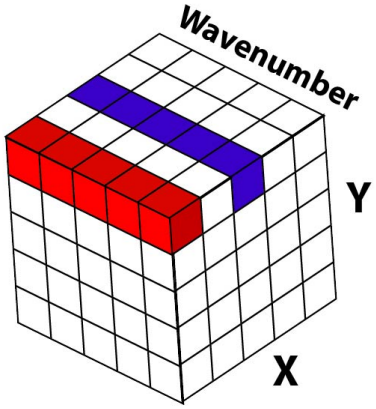

Figure 1.9: Simplified FTIR hyperspectral data cube structure. Only 5 by 5 pixels and 5 discrete wavenumber data points are illustrated herein for clarity. FTIR spectral data that is resolved to two spatial dimensions is structured as a three dimensional (X, Y, $\bar{\nu}$) table of absorbances. The positions of absorbances corresponding to two pixel spectra are highlighted.

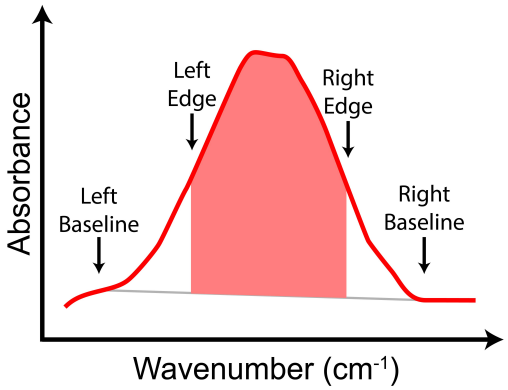

Figure 1.10: Spectral peak (**red** solid line) with peak parameters defining baseline corrected integration. Left Baseline (LB), Left Edge (LE), Right Edge (RE) and Right Baseline (RB) are indicated with arrows. The resulting peak area is shaded.

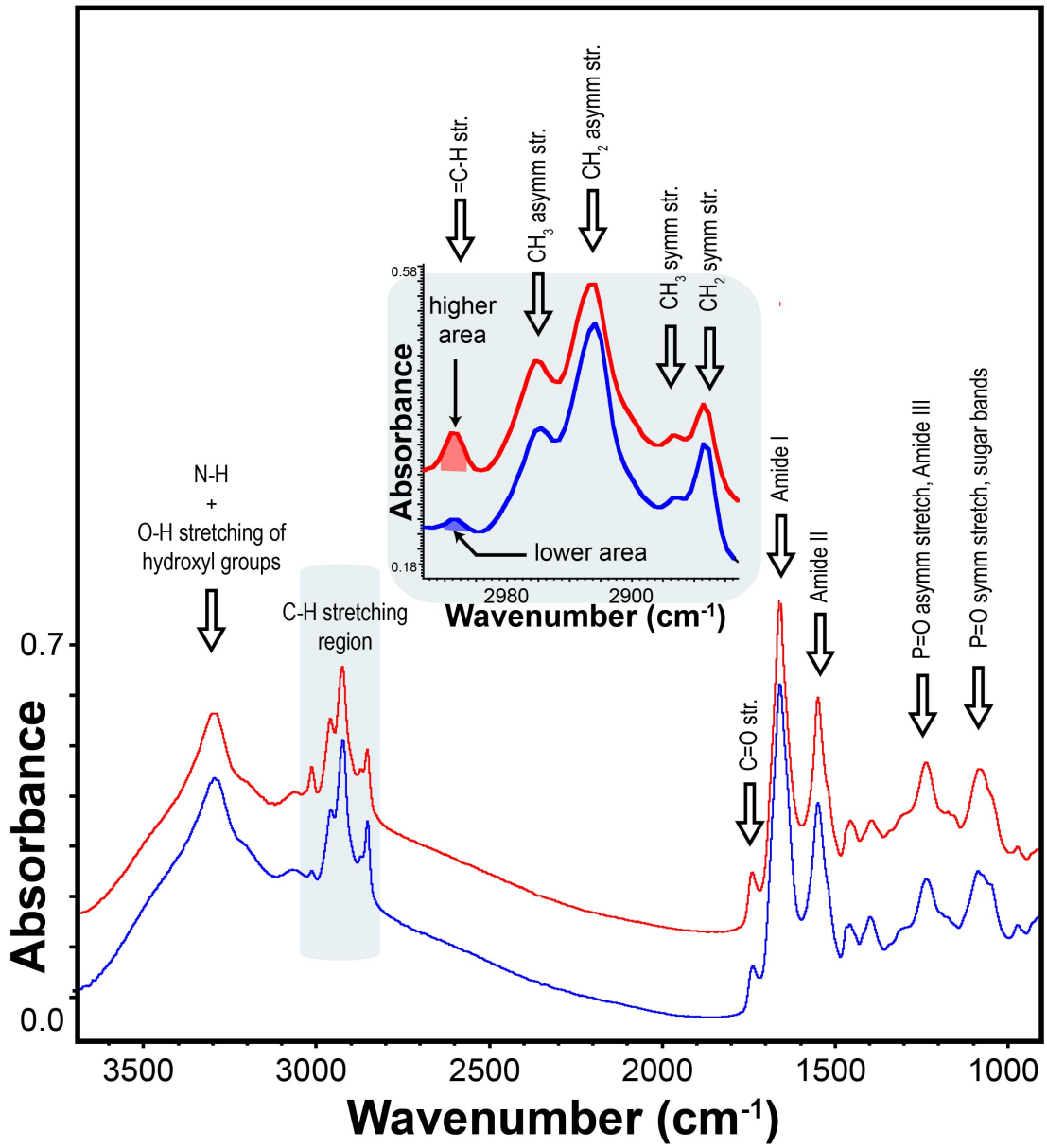

Figure 1.11: FTIR pixel spectra with 1024 discrete wavenumber data points per spectrum. Spectral region of interest is highlighted and expanded to illustrate spectra with (**red**) high and (**blue**) low values for baseline-corrected peak integration. Spectra are on common scale, offset for clarity. Parameters used for integration correspond to shaded areas under the curves. Though many other vibrational modes absorb, only the positions of a selected number directly relevant to this thesis are marked for clarity. Pixel spectra shown for introductory purposes are of the rod outer segment of murine retinal tissue cryosections adapted from Stitt et al. (2012).

Figure 1.12: A scale bar showing the colour mapping that was applied to processed images unless otherwise specified.

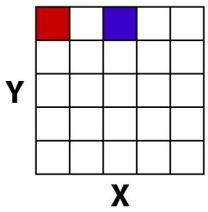

Figure 1.13: Simplified depiction of a false-colour two dimensional (2D) FTIR image (5 by 5 pixels) processed for an integrated absorbance band in the pixel spectra. High and low values are mapped to **red** and **blue**, respectively.

1.3.5 Image Artifacts

Anomalies during visual representation can degrade fidelity and produce imaging artifacts. In general, images with high quality preferably have a reduced number image artifacts. There are a variety of imaging artifacts associated with FTIR imaging.

Vignetting Artifacts

Vignetting is a type of pixel-to-pixel systematic non-uniformity in optical systems. Vignetting artifacts occur at the periphery of images as a decrease in brightness. There are multiple causes of vignetting, e.g. the falloff of light intensity at the outer edges of a single beam of light. Image calibration problems can stem from IR beam vignetting (Hanssen and Zhu, 2002).

Mosaic Seams

If mosaic creation software is miscalibrated or the stage has a large inaccuracy in positioning the sample between tile acquisitions, image artifacts appear as seams between the tiles (Figure 1.14). For example, backlash (AKA 'gear slop') during stage movement could cause a slightly different area to be in the field of view during acquisition, one that would not correctly be used to fill in the quadrant of a 2 by 2 mosaic. The resulting image distortion can affect the quantitative measurement of area, for example, in Figure 1.14, the brown sunflower center area is artificially reduced due to a seam artifact. [11]

[11] The compatibility of the tomography accessory with mosaicing is described in §2.1.2.

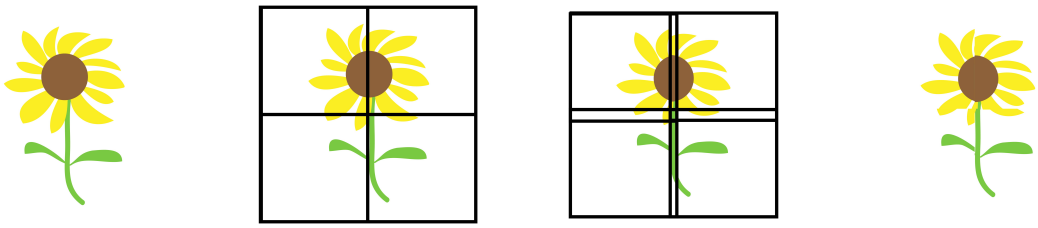

(A) Original Object **(B) Correct seams** **(C) Incorrect seams** **(D) Incorrect image**

Figure 1.14: Illustration representing a seam artifact in a composited, multi-tile FTIR image (mosaic, 2 by 2 tiles). **(A)** An imaging subject (sunflower) that is larger than a single FPA tile. **(B)** A complete and correct image captured as a mosaic. Tiles are outlined in black. Incorrect seaming giving rise to **(C)** incorrect tile position and **(D)** an image with seam artifacts.

Chromatic Aberration

Chromatic aberration is a dispersive artifact that can occur in images, including FTIR images. For transmission mode FTIR-SMI, certain frequencies of light will be unfocused when others are focused because of dispersion and refraction through infrared windows, a typical substrate for tissues sections and other imaging subjects. There can be different focal lengths for different frequencies of infrared light, due to the refraction occurring at the air-IR window interface. (Chan and Kazarian, 2012). [12]

Scattering Artifacts

The Lorenz-Mie-Debye solution to Maxwell's equations describe the scattering of electromagnetic radiation by spherical objects, non-molecular particles such as aerosols. The scattering of light by particles with sizes that are comparable to its wavelength is known as resonant Mie scattering (RMieS). The amount of light scattered is not equal for all wavelengths. Consequently, there are broad baseline effects apparent in spectra.

The resulting broad spectral baseline effects (Griffiths and De Haseth, 1986) can hamper the relation of spectra to concentration and quantitative analysis via Beer's Law.

[12] Infrared microtomography does not require an infrared window, thus the technique is free of the chromatic aberration associated with such windows.

Locke expounded upon the scattering of cylindrical objects (Lock, 1997). The Locke solution to Maxwell's equations may be more applicable to fibers, which are also cylindrical. Scattering negatively impacts the quantitative analysis and the resolution of 2D images. Scattering causes changes in the direction of light that blur an image. The misdirected light can also result from an absorption process, which gives the scattered light a particular spectrum. IR light wavelength is on the same order of magnitude of size as micro-samples that are desirable as image subjects. Scattering from distinct particles with diameters ranging between 2-20 micrometers is documented. Scatter is immediately apparent as a broad baseline when the entire mid-infrared region is shown. When only the fingerprint region of the IR spectrum is displayed, scattering appears more subtly in dispersive line-shapes and altered spectral peak maxima.

Attempts to apply the Mie solution corrections to scattering in spectra have been made (Bassan et al., 2009). In practice, cells do not have geometrically perfect shapes, and, due to this and other concerns, such corrections have limited utility.

1.4 Tomography

The word 'tomography' stems in part from the ancient greek root $\tau\acute{o}\mu o\varsigma$ ('tomos'), meaning 'slice' or 'section'. Modern tomography involves visualization of cross-sections via a penetrating wave. Measurements of light or particle transmission permits reconstruction of internal structures. Various forms of tomography employ different sources of penetrating wave: beams of electrons, gamma rays, x-rays, ultrasound, sonar, etc.

One form of tomography commonly used in hospitals is human Computer Aided Tomography (CAT scans), in which the detector and x-ray light source are rotated while the imaging subject, a patient, remains more or less stationary. In contrast, in electron tomography, an extension of traditional transmission electron microscopy (TEM), the sample is rotated, and the electron source and detectors are fixed in place. In both cases, there is some

form of rotation about an axis, whereby an object is illuminated from different directions to form projections. Through tomography, it is possible to recover the axial cross-sections from such projections (Kak and Slaney, 1988).

Transmission electron microscopy (TEM) has superior resolution, due to the wavelengths employed. Faster, shorter wavelength electron beams generate images with finer detail; however, this technique is monochromatic, i.e. does not capture spectral information. In contrast, other techniques, such as X-ray microtomography, can create hyperspectral images. X-ray microtomography systems have been built with sufficient spectral resolution to distinguish individual elemental absorption edges (Egan et al., 2015). FTIR microtomography systems have been built with sufficient spectral resolution to distinguish absorption of infrared-active vibrating molecules (Martin et al., 2013; Quaroni et al., 2015). Like the spectroscopy techniques from which they stem, these different forms of microtomographic imaging have different niche utilities. X-ray microtomography is well suited for elemental analysis, while FTIR microtomography can be used to analyze chemical functional group distributions. Multiple techniques are complementary and useful for correlated microscopy.

1.4.1 Modeling of Objects

The basis for tomography is the interaction between light and matter. It is stated in Beer's law that the concentration of a chemical is directly proportional to light absorbance. Specifically, incident light of intensity I_0 is transmitted through an attenuating object and strikes a detector with a final intensity I. Objects can be modeled as distributions of attenuation coefficients, μ, defined in Equation 1.5.

A Single Voxel

Consider the case of light with intensity I_0 entering a small square homogenous object with thickness ℓ (Figure 1.15). The beam is attenuated by Beer's law as per Equation 1.12. The

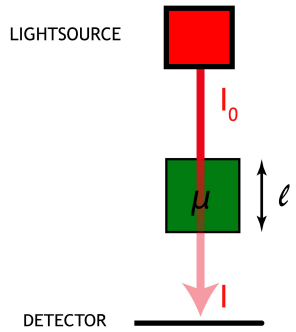

Figure 1.15: One ray of light passing through one voxel. Adapted from Seeram (2015).

values for ℓ, I , I_0 and e are known, thus unknown object μ can be calculated (Seeram, 2015) with Equation 1.7.

Multiple Voxels

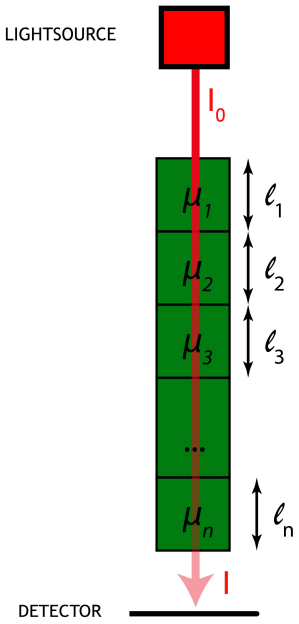

Figure 1.16: One ray of light passing through multiple adjacent volumes, i.e voxels. Adapted from Seeram (2015)

In a case where the light is passing through a series of voxels that comprise a larger

object (Figure 1.16), μ can be expressed as follows (Seeram, 2015):

$$\mu_1 + \mu_2 + \mu_3 ... + \mu_n = \mu_{\text{total}} \tag{1.15}$$

The thickness of each voxel is of equal length, therefore:

$$\ell_1 = \ell_2 = \ell_3 ... = \ell_n \tag{1.16}$$

The situation is such that, by Beer's law:

$$log\left(\frac{I_0}{I}\right) = \ell_1\mu_1 + \ell_2\mu_2 + \ell_3\mu_3 + ... + \ell_n\mu_n \tag{1.17}$$

$$\frac{1}{\ell_{\text{total}}} log\left(\frac{I_0}{I}\right) = \mu_1 + \mu_2 + \mu_3 + ... + \mu_n \tag{1.18}$$

Alternatively this can be expressed in terms of absorbance, A:

$$\frac{1}{\ell_{\text{total}}} A = \mu_1 + \mu_2 + \mu_3 + ... + \mu_n \tag{1.19}$$

Parallel Rays Passing Through a Continuous Object

Consider an imaging system as remaining motionless in world-centric 3D space, defined by three Cartesian coordinates, X,Y and Z (Figure 1.17). Tomography can take place by rotating an object, the imaging subject, in the Z axis, relative to this fixed frame.

An object can be modeled as a 3D spatial distribution of attenuation constants, μ, on a second Cartesian coordinate system centered upon the object, defined by x, y, z. The value of the attenuation constant varies between points on the object and is given by μ(x, y, z) (Seeram, 2015).

Suppose that the object and the object-centric Cartesian axes x and y, are tilted at θ degrees from X and Y. A ray of light with initial intensity I_0 travelling parallel to the Y axis

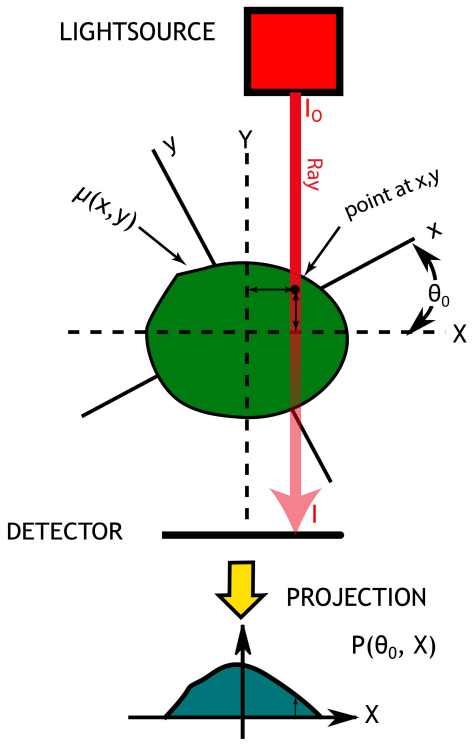

Figure 1.17: Multiple rays passing through an object (green, irregular shape) with absorbance coefficients defined by a continuous function. Dashed lines indicate Cartesian axes fixed in space: X, Y (shown as horizontal, vertical) and Z (pointing toward the reader, not shown). The object rotates around the Z axis. Adapted from Seeram (2015).

can pass though the attenuating object, such that the transmitted beam strikes the detector with intensity I (Seeram, 2015). The distance between the source and detector is constant at unity. In this case, I is given by:

$$I = I_0\ 10^{\left[-\sum_{source}^{Detector}\mu(x,y)\right]} \tag{1.20}$$

The logarithm of the ratio of intensities will have a linear relationship to the sum of attenuation constants:

$$log(\frac{I}{I_0}) = -\sum_{source}^{Detector}\mu(x,y) \tag{1.21}$$

When $\mu(x,y)$ is a continuous function, the relationship is more appropriately expressed as the logarithm of I/I_0 being linearly related to a corresponding line integral. Here, the line integral of $\mu(x,y)$ represents the total attenuation suffered by a beam of light as it travels

through the object (Seeram, 2015), i.e. absorbance. The line integral $P_\theta(X)$ is defined as:

$$P_\theta(X) = \int_{(\theta,X)line} \mu(x,y)Y \tag{1.22}$$

The equation of the line corresponding to a ray of light that travels parallel to Y is:

$$x\ cos(\theta) + y\ sin(\theta) = X \tag{1.23}$$

so equation 1.22 can be rewritten as:

$$P_\theta(X) = \int_{-\infty}^{\infty}\int_{-\infty}^{\infty} \mu(x,y)\delta(x\ cos\theta + y\ sin\theta - X)dx\ dy \tag{1.24}$$

the function $P_\theta(X)$ is known as the Radon transform.

Note that there is an assumption that light propagates through the sample in straight lines and that no scattering occurs. (Seeram, 2015)

Clearly, this assumption does not hold true for infrared light, which is diffractive. However, interventions to reduce scattering (Section 3.2, Chapter 4) make the Radon transform a relatively more applicable model. As well, validation methods such as phantom imaging can allow us to understand the extent of the effects caused by using the inverse Radon transform with infrared data.

1.4.2 Back-Projection

Filtered Back-Projection (FBP) is a method to calculate the inverse Radon transform. This reconstruction method can be formulated as an algorithm combining back-projection and a filter. A filter such as the ramp or Ramachandran-Lakshminarayan (Ram-Lak) filter is employed. The Ram-Lak filter in the frequency domain simply sets the absolute value of frequency equal to the weight function Zeng (2015).[13]

[13]Low frequencies have low weight. High frequencies have high weight.

Back-Projection of a 2 by 2 Matrix.

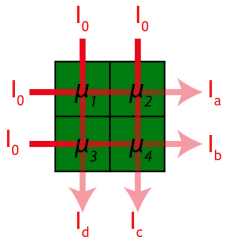

Figure 1.18: Back-projection of a square object with different μ in each quadrant in a 2 by 2 matrix. Light of initial intensity I_0 enters the object, passes through two quadrants and is attenuated. The attenuated light I (a, b, c, d) is detected. Adapted from Seeram (2015).

Intensities ($I_{a,b,c,d}$) that are detected when light is transmitted through a two-by-two matrix of μ (Figure 1.18) are given by the following equations (Seeram, 2015)[14]:

$$I_a = I_0 * 10^{-(\mu_1 + \mu_2)\ell} \tag{1.25}$$

$$I_b = I_0 * 10^{-(\mu_3 + \mu_4)\ell} \tag{1.26}$$

$$I_c = I_0 * 10^{-(\mu_1 + \mu_3)\ell} \tag{1.27}$$

$$I_d = I_0 * 10^{-(\mu_2 + \mu_4)\ell} \tag{1.28}$$

where I, I_0 and ℓ are known quantities. Sub-equations can be formed:

$$S_a = \mu_1 + \mu_2 \tag{1.29}$$

$$S_b = \mu_3 + \mu_4 \tag{1.30}$$

$$S_c = \mu_1 + \mu_3 \tag{1.31}$$

$$S_d = \mu_2 + \mu_4 \tag{1.32}$$

and the 4 unknown values of an 2×2 image matrix can be solved by solving a system

[14]Here, l is the total length through the object

of linear equations.

Artifacts

The overlapping of images with low spatial frequency (i.e. coarse rather than fine details) creates a blur-like effect. A ramp (Ram-Lak) filter is applied to eliminate some of these low frequencies. FBP can induce greater noise because the filter is prone to amplify high-frequency content (Seeram, 2015). An example of this effect is seen later in Figure 6.9.

1.4.3 Resolution

The 3D spatial resolution of tomographic reconstructions is described in terms of axial and trans-axial components. Resolution in the axial direction[15] is limited by slice thickness, i.e the intrinsic spatial sampling of pixels in a single Cartesian dimension due to the physical spacing of the detector electronics. Trans-axial resolution varies depending on proximity to the axis of rotation in tomographic images. Specifically, with simple back-projection, the tomographic resolution deteriorates as distance from the axis of rotation increases. Ramp-filters are often applied only in the trans-axial plane (yz) because it is the only plane that experiences blurring associated with simple back-projection (Barrett and Swindell, 1996).

1.4.4 Angular Sampling

One can take advantage of symmetry to reduce the number of viewing angles sampled for a tomographic data set. Projection data at viewing angle $\theta = \alpha$ is redundant to its counterpart at an angle of $\theta = \alpha + 180^\circ$. Thus, the projections from angles $0^\circ \leq \theta < 180^\circ$ are sufficient to reconstruct a volume. The use of additional redundant viewing angles contributes to an increase in sensitivity and improves the S/N of reconstructed data. (Bailey et al., 2005).

The total number of real, independent, non-aliased pieces of information (POI) that can

[15]The axial direction is along Cartesian coordinate X in the thesis images.

be extracted from a tomographic data set was shown to be approximately:

$$N_{POI} = \frac{2}{\pi} M^2 \tag{1.33}$$

where M is the number of equally spaced projections from 0 to π (Rattey and Lindgren, 1981). This finding has implications for the maximum useful number of FTIR images required for a tomographic data set, explored later.

1.5 Infrared Microtomography

FTIR microtomography was first demonstrated by Martin et al. (2013) as a novel approach to a nondestructive, spatially three-dimensional (3D) imaging of microscopic distributions of chemical composition throughout an intact biological or materials sample. Their custom tomography apparatus combined with the InfraRed ENvironmental Imaging beamline (IRENI) (Nasse et al., 2012, 2011a) at the former Synchrotron Radiation Center (SRC), Univ. of Wisconsin-Madison in 2013, generated the very first published FTIR spectral images resolved spatially to 3D. A variety of samples were imaged: a *Zinnia elegans* tracheary element on a polyimide microloop, a *Populus* wood fiber, a strand of human hair[16], and murine embryoid body colony of stem cells. The integration of absorption intensities in specified spectral regions was performed with and without baseline subtractions. The spectrum associated with one reconstructed voxel [17] extracted from tomographic reconstructions of the polyimide microloop was published (Martin et al., 2013).

The FTIR microtomographic method, after separate modification for use with thermal-source FTIR microscopes, generated images of a cell within onion tissue by Quaroni et al. (2015) and Arctic sea ice diatoms by Findlay et al. (2017). Some method developments employed by Findlay et al. (2017) are described in Part I.

[16] A fresh sample was obtained from one researcher's head.

[17] This is referred to as a 'voxel spectrum' in this thesis, as a 3D counterpart to the term 'pixel spectrum' which can be found in 2D spatially resolved FTIR imaging literature.

1.6 Statement of Purpose

The handful of publications described in the previous section constitute the state-of-the-art in FTIR microtomography. It is clear that the technique was in early stages of development when used in combination with the synchrotron light source. As such, there exists great potential for improvement.

The following sections describe development of a laboratory-based hyperspectral FTIR microtomography method which allows the internal biochemical distributions of microscopic samples to be reconstructed and visualized in three dimensions. The method was adapted towards the dual purposes of demonstrating the capabilities of 3D FTIR imaging and extending existing FTIR microtomography methods to specific problems encountered with biological samples. The advantages and drawbacks of FTIR microtomography can be demonstrated, in order to establish the niche of applications best conquered with 3D FTIR imaging.

Part I

PROCESS OPTIMIZATION

In general, process optimization activities, such as method development and validation, are intended to enhance the utility of FTIR microtomography to the purposes of a wider scientific community. An affordable new design for a tomography accessory for infrared microscopes can be assembled from consumer-available parts. The detailed description of open-source software and inexpensive hardware needed to build an accessory are provided in the next section in order to encourage wide-spread adoption of basic tomographic imaging functionality.

Chapter 2. Method Development

2.1 Apparatus

2.1.1 Main Apparatus

Spectrometer

An Agilent Cary 670 spectrometer (Figure 2.1) was used in combination with an FTIR microscope to acquire the spectra and spectral images shown in this thesis.

Spectral Data Sampling Spectra were typically acquired over the range of 4001.60 to 898.67 cm^{-1} (approximately 4000 to 900 cm^{-1}) with 3.86 cm^{-1} spectral resolution. The data point spacing of 1.93 cm^{-1} meant that a total of 1610 discrete data points were recorded per spectrum. These precise values are specific to the Agilent microspectrometer employed.

FTIR microscope

A Cary 620 FTIR Microscope from Agilent Technologies was used to generate all the spectral images in this thesis. This thermal source instrument is equipped with a 64 $\times$ 64 Focal Plane Array (FPA) ($5.5\,\mu m$ pixel edge, MCT detectors) and was coupled to the spectrometer (Figure 2.1) described above in Section 2.1.1. A high magnification upgrade to the microscope was used for all the transmission mode thermal source imaging at the University of Manitoba (UofM).

High Magnification A 15$\times$ objective (NA 0.62, 21 mm working distance) combined with additional high magnification optics (5$\times$ increase, proprietary to Agilent Technologies) was installed on the FTIR microscope to yield images with a geometric pixel size of $1.1 \times 1.1\ \mu m^2$ (Findlay et al., 2015).

2.1.2 Tomography Accessory Apparatus

The tomography accessory for microscopes[1] (US Patent, Findlay and Gough (2016)) is a removable module, whereby a target can be held and moved in the IR microscope field-of-view. Inexpensive prototypes[2] of the tomography accessory exemplify alternative architectures with compatible and portable features that fit the requirements for tomographically imaging larger globular samples (single diatom or human buccal cells, Chapters 5 and 6, respectively) and elongated samples (diatom colonies, and artificial spider silk, Chapters 5 and 4, respectively).

The tomography accessory is comprised of hardware forming three subsystems that: 1) hold the sample under the microscope objective lens, 2) physically align a micro-sample for rotation, and 3) rotate the sample. Current prototype rotation systems have been automated and have software involved in their function. Prototype alignment systems involved strictly manual adjustments, and did not involve software.

Hardware

The tomography accessory hardware assemblies were designed for use with the commercially available FTIR microscope described in Section 2.1.1. The primary functional systems and subsystems of the accessory were arranged to fit the microscope dimensions and rotate with clearance while riding on the microscope stage. Additionally, size was limited by the maximum height above the stage that the Schwarzchild lenses could focus on, i.e. the ceiling of the system. Towards this end, miniature and lightweight components were selected. In the next section, specific parts and their assembly and function are described.

[1]The accessory could conceivably be useful to other forms of microtomography, so general language (‘microscope’) rather than the specific ‘infrared microscope’ was employed during the patent process.

[2]A note regarding a question of language: It is true that there has been no development of my device into advanced or final products. Still, the devices are ”prototypes” in the sense that I hope that in the future they may be fully robotized and automated with software to form part of a finished tomography accessory product.

Prototype Mark I In the first prototype of the tomography accessory the sample holding hardware subsystem was composed of a collet on an outstretching shaft. The sample holder was fixed to an aluminum mounting hub (Pololu Robotics and Electronics, USA) that connects to a physical alignment subsystem.

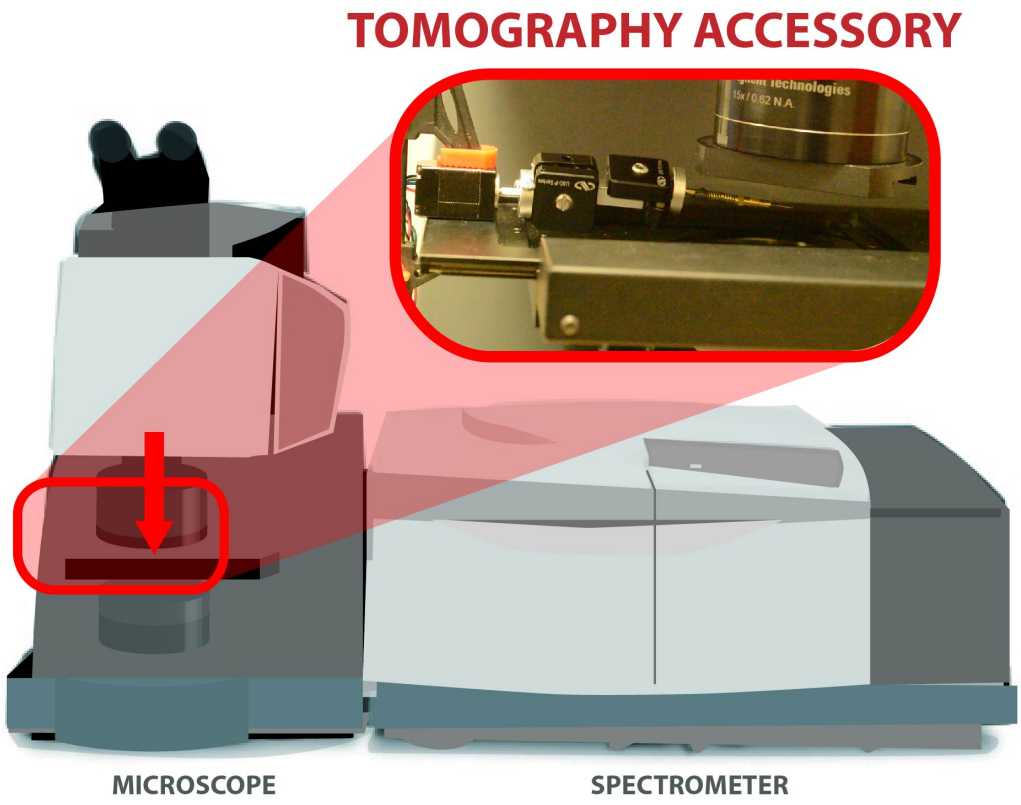

Figure 2.1: Tomography accessory installed on an FTIR microspectrometer.

In the first prototype, two identical platform optical mounts (Newport Corporation, USA, 1.0 $\times$ 1.0 in., 80 turn per inch (TPI) Allen-Keys) were oriented at 90° from each other and fastened together. This assembly was in turn fixed to a second circular aluminum mounting hub (Pololu), which attached to a stepper motor output shaft.

Stepper motors, like the one in Figure 2.3, provide rotation that is especially precise when operated at low velocity with light loads, as is the case in FTIR microtomography. Permanent magnets within the motor can detent[3] the shaft at precise angular intervals with-

[3]The word 'detent' can be used as a verb to describe the action of creating a mechanism to lock or unlock

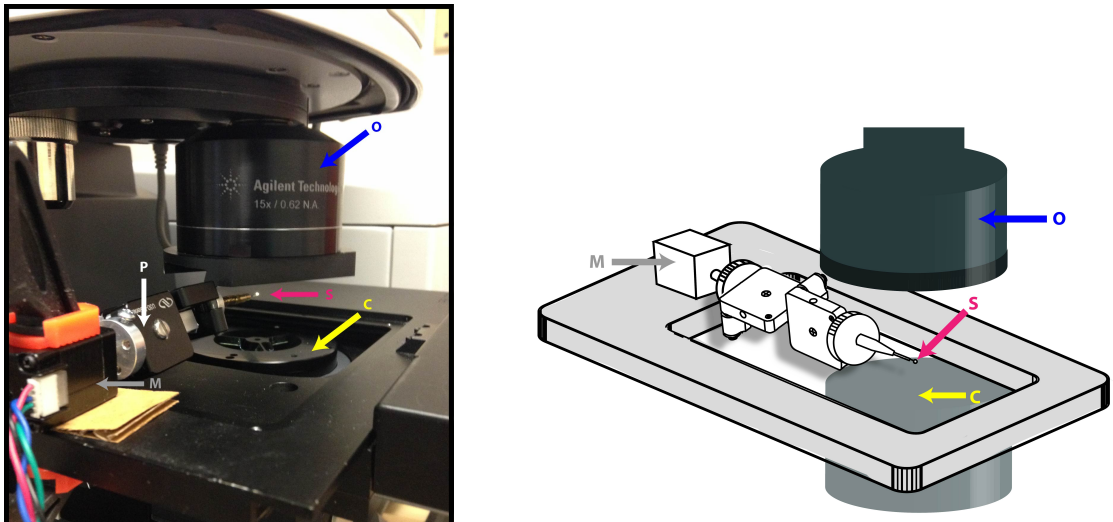

(A) Visible **(B)** Schematic

Figure 2.2: Infrared Microscope with tomography accessory prototype Mark I (P, white arrow). Microscope parts highlighted include the microscope stage (square ring), and (**C**, yellow arrow) the condenser and (**O**, blue arrow) the objective Schwarzchild lenses. Accessory parts highlighted include (**M**, gray arrow) the stepper motor. (**S**, pink arrow) The sample imaging subject is illuminated in (A) the visible light image, but not in (B) the schematic depiction.

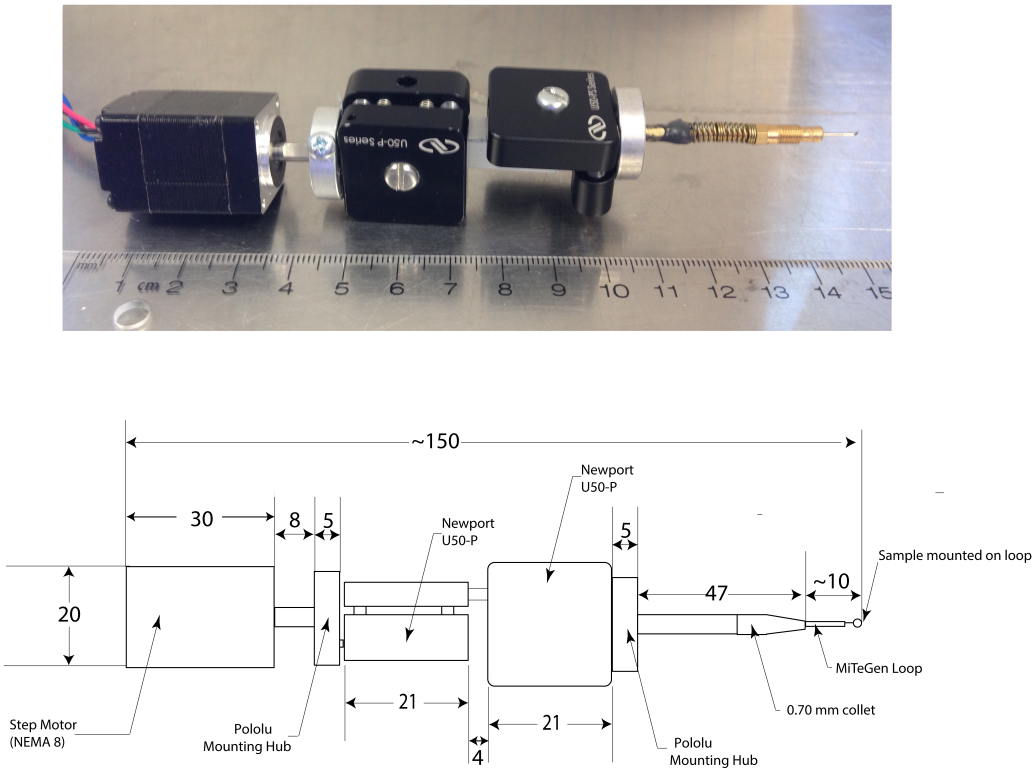

Figure 2.3: Prototype (Mark I) of the tomography accessory for infrared microscopes. **(TOP)** Visible light image and **(BOTTOM)** schematic representation of the prototype. Loop is optional. Schematic dimensions are in millimeter units.

out any additional power or control systems.[4] Energization of the motor applies torque to the stepper motor output shaft for two purposes: 1) increasing the force of detention or, 2) initiating rotation. The stepper motor in the tomography accessory provides non-cumulative angular error, unlike other types of electric motor. The infrared microtomography setup reported by Martin et al. (2013) had closed-loop control over a rotation system to ensure precision of rotation. In our tomography accessory system ('tomography accessory') the low and non-cumulative angular error makes an inexpensive open-loop control system a viable option. Simulations of the impact of the angular error suggest that the use of stepper motors should not cause reconstruction problems in pixelated FTIR tomographic reconstructions (Section 3.1.5).

An off-the-shelf microcontroller (Arduino Uno™) was wired to the stepper motor. The microcontoller was chosen based on its ease of use, ubiquitous availability and popularity in do-it-yourself (DIY) hobby electronics.

Prototype Mark II The second prototype of the tomography accessory for infrared tomography (Mark II) had several functional differences. The Mark II motor has a planetary gearbox to permit rotation of imaging subjects to additional viewing angles; it is compatible with a plurality of multi-tile sampling schemes. The Mark I prototype requires the fine adjustment of three different precision machined screws (high TPI) to achieve sample translation, while the Mark II only requires one such screw to be adjusted manually. The Mark II prototype was not used extensively, as it eventually developed some problems with position stability, possibly due to loosening of connections between parts, or mechanical wear.

movement.

[4]During the design phase, crude proof-of-concept data sets were obtained with manual rotation of a de-energized stepper motor, prior to the development of the tomography accessory.

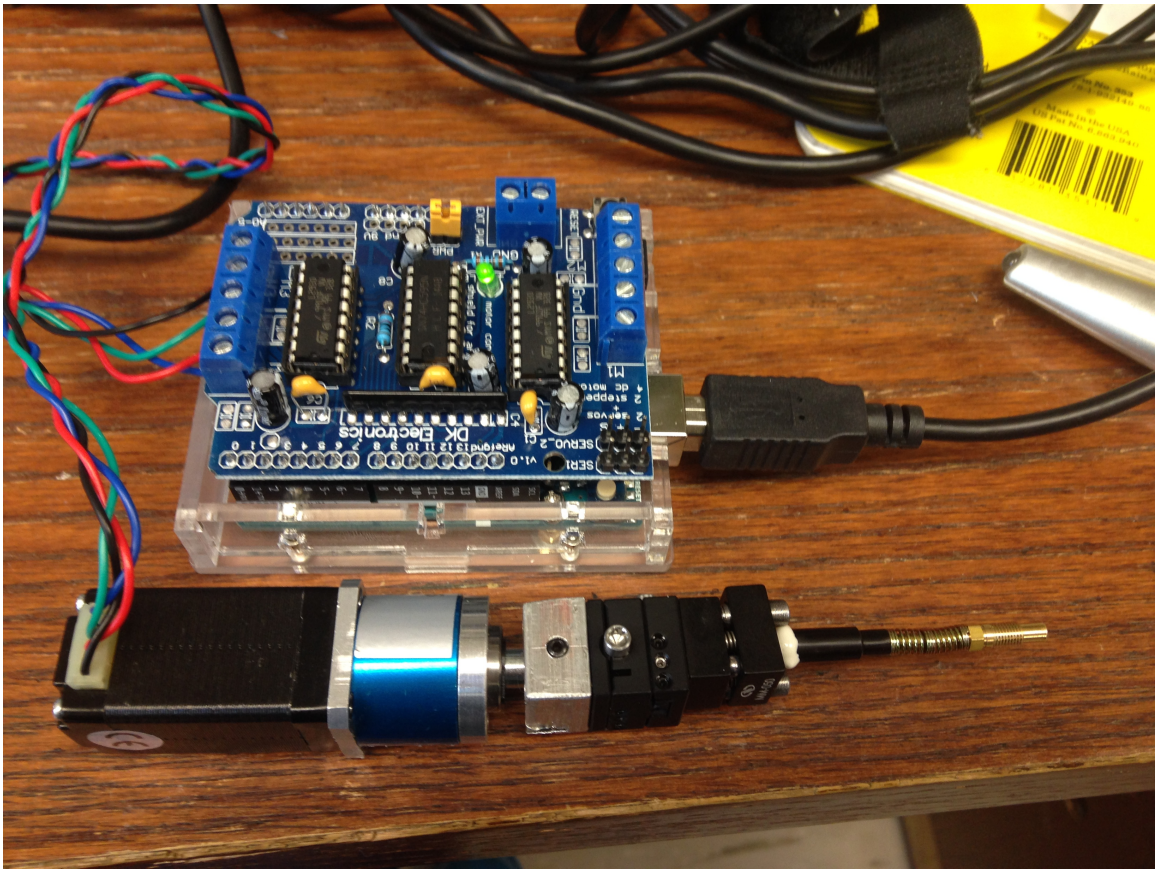

Figure 2.4: Visible light image of the Mark II prototype tomography accessory for infrared microscopes. No sample loaded.

Features and Considerations

Armature Length Increasing the diameter of the objective lens of a microscope increases numerical aperture. The tomography accessory sample holding arm has to be sufficiently long to extend under the relatively large diameter (∼10 cm) of the exterior housing of the Agilent microscope Schwarzchild objective lens.

With increasing armature length comes a trade-off for physical positioning stability of the held sample. It is possible for adjacent equipment to cause physical vibration that will be magnified by a long sample-holding armature. This consideration is particularly important for synchrotrons with beamline congestion and many sources of vibration. Vibration causes the imaging target to shake while held in the microscope field of view. Such extraneous movement of the imaging target is not accounted for in simple models of tomographic reconstruction.

Consistent Turn Directions The tomography accessory system employed forward[5], positive[6], counter clockwise (CCW)[7] angular rotation relative to starting position of the motor shaft and loaded sample. Consistency in the registration of turn directions prevented the reconstruction errors observed in simulations.

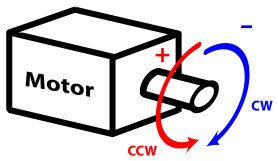

Figure 2.5: Motor directions. (**red**) Positive CCW and (**blue**) negative CCW rotation of the motor output shaft are marked with arrows.

[5] 'Forward' and 'backward' terminology is used in the adafruit motor control library and the tomography accessory Arduino sketch (§9.3).

[6] The CCW step counts in Matlab and Arduino were positively numbered.

[7] The turn direction is CCW as viewed from the motor output shaft side of the tomography accessory.

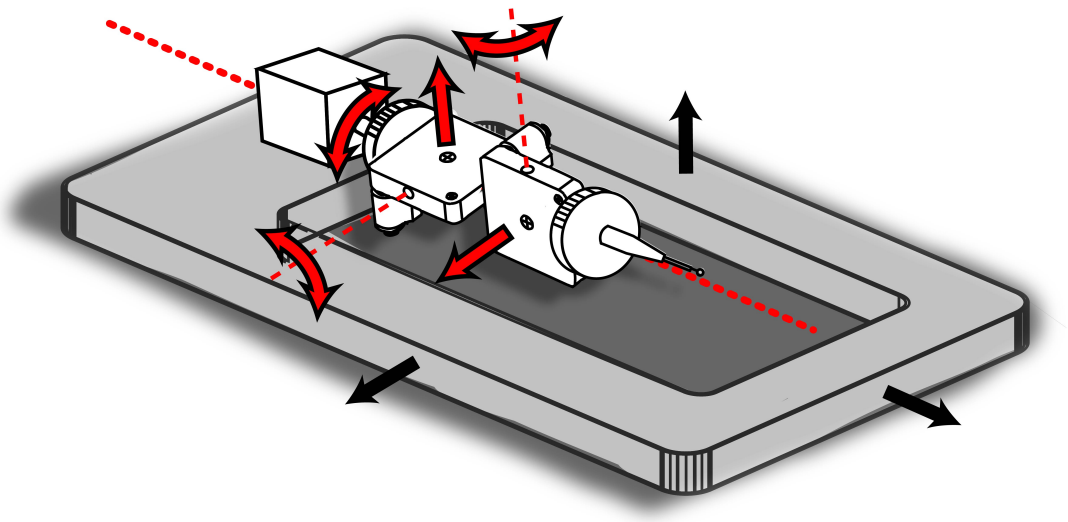

Figure 2.6: Degrees of Freedom for the tomography accessory Mark I prototype. The black arrows indicate the translations of the microscope stage along the three Cartesian coordinates defining the fixed frame of the microscope (X, Y, Z). **Red** arrows indicate the degrees of freedom provided by the tomography accessory, relative to the output shaft of its motor.

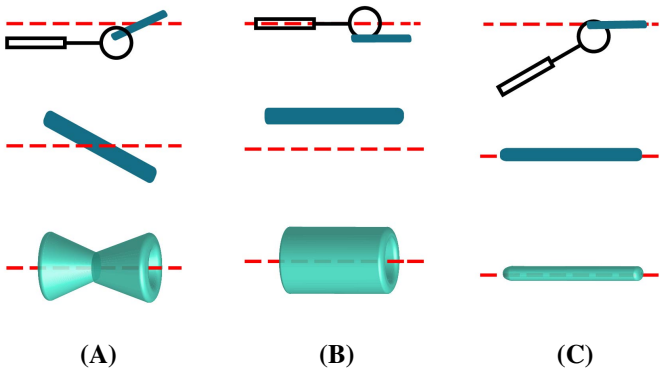

Figure 2.7: Tomography accessory sample holder loaded with a polyimide microloop-mounted cylindrical sample. **(TOP)** Position and orientation of cylindrical imaging target (**dark blue**) relative to axis of rotation (red dashes) leads to **(MIDDLE)** the imaging target **(BOTTOM)** tracing of different paths (**light blue**) during rotation: **(A)** tilted; conical or hourglass **(B)** linear but offset; cylindrical, and **(C)** linear and aligned; minimal profile.

Degrees of Freedom for alignment The degrees of freedom for the tomography accessory are shown in Figure 2.6. In both prototypes there is an adjustable assembly for supporting the sample holder on the output shaft of the electric motor such that: i) the sample holder is translatable relative to the output shaft along at least one translation axis perpendicular to the output axis, and ii) the sample holder can pivot relative to the output shaft about two pivot axes which are transverse to one another and which are perpendicular to the output axis. Rotation around three orthogonal axes (R_x, R_y, R_z) is also possible.

Simply put, the tomography accessory is more flexible and capable of additional adjustments to sample pitch, yaw and roll, versus other previously published designs. It can centre the rotating sample to the motor via translational movement (T_x, T_y, T_z). The centered rotation of the sample can be further centered to the middle of the microscope field-of-view (T_X, T_Y), and focused (T_Z) with the translation of the stage.

These degrees of freedom permit both tilted (Figure 2.7A), and straight (Figure 2.7B) samples to be aligned for tomographic imaging (Figure 2.7C) and were particularly useful for aligning diatoms (Figure 5.4).

Imaging of objects larger than one tile The tomography accessory was designed to be compatible with the previously described features of the microscope stage. It mounts directly onto the FTIR microscope stage (Figure 2.2), thus larger measurement areas and volumes can be obtained by mosaicing. The tomography accessory is practical for a laboratory work-flow environment. The 2D imaging capabilities of the FTIR microscope are not compromised by rapid switching to and from 3D mode. Unlike the design reported by Martin et al. (2013), removal of the microscope stage is not necessary. This is particularly important because the stage performance for other tasks, especially mosaic collection, is severely degraded when the stage is uninstalled and reinstalled often.

Software

Rotation System Software Given the numerous images that needed to be acquired, manual rotation systems were not feasible. Automated rotation and control software was scripted for the collection of FTIR data from the multiple views composing a FTIR tomographic data set. An Arduino sketch script (Listing 9.3) was uploaded to the Arduino Uno microcontroller of the tomography accessory. The imaging subject was rotated on an axis parallel to the X-axis and perpendicular to the incoming light at software-triggered time intervals.

Alignment System Software There was no alignment system software. The current hardware based, manual alignment system was workable without software, as alignment only needed to be performed once per sample, prior to tomographic data set acquisition.

2.2 Choice of Angular Sampling Scheme

It is impossible and unnecessary to collect FTIR image data at an infinite number of viewing angles. Reconstructing limited data requires only a finite number of viewing angles. The 2D spatially resolved FTIR images are pixelated, i.e. limited and composed of discrete data points, not continuous functions. The spatial frequency of the view data is bounded (bandlimited) and it is possible to reconstruct with negligible additional aliasing error if enough projection angles are sampled. Angle spacing must be small enough to prevent information loss, but only needs to be large enough to enable reconstruction of the bandlimited input 2D images.

For example, at least 4096 real, independent, non-aliased pieces of information (N_{POI}) need to be reconstructed for there to be one for each voxel in a reconstructed 64×64 voxel axial slice.

Rearranging equation 1.33:

$$M = \sqrt{\frac{\pi}{2} N_{\text{POI}}} \tag{2.1}$$

and inserting an N_{POI} of 4096 into the equation gives the following:

$$M = \sqrt{\frac{\pi}{2} 4096} = 80.21 \tag{2.2}$$

After rounding up, one can see that collection of M = 81 projections at viewing angles equally spaced between 0 to π provides the appropriate angular sampling.

That being said, an object smaller in diameter than the full width of a single tile will have unoccupied voxels at the outer edges of the image that are inconsequential. It is possible to acquire projections sampled at a smaller number of views adequate for the reconstruction of occupied pixels, i.e. fewer than 81 projections for a tomographic data set consisting of single tiles. In general, sampling schemes may vary with imaging subject size. Specific sampling schemes were tested in simulations for verification purposes in Section 3.1.3.

2.3 Acquisition Procedures

The full procedure for tomography data set acquisition is described in detail in Appendix Section 9.1. Essentially, the tomography accessory is clipped onto the FTIR microscope and a micro-sample is loaded onto it. An AutoHotKey macro script (Listing 9.4) is activated in order to send keystrokes and to switch between two program windows: 1) Agilent Resolutions Pro™ (Res Pro) software to start and complete the image collection (single tile or mosaic) and 2) Arduino Integrated Development Environment (IDE) serial communication interface (Version 1.6.5) software to rotate the sample. The data files are exported to ENVI file format in Res. Pro.

2.4 Data Processing

Our approach has been to avoid processing that employs down-sampling, which outright degrades the quality of data, but speeds up processing. A standard 64-bit, Intel Core i7 laptop had computational capacity sufficient for a sequence of processing steps to be applied to FTIR spectral data within the MATLAB^{TM} (version R2014a) environment. The processing time for a single tile tomographic data set was typically less than 10 minutes.

2.4.1 Pre-Processing

The ENVI formatted FTIR images were loaded using either the built-in Matlab^{TM} 'Multi-BandRead()' function or an ENVI file reader/writer mini-toolbox (Totir, 2010). Each image was integrated, displayed, visually screened for obvious scattering artifacts and resaved in Matlab^{TM} MAT-file format for partial loading of variables. The images were rotated 90° for compatibility with the reconstruction function, which assumed rotation about a vertical axis. If the axis of rotation was not perfectly centered, (e.g. not positioned at the 32^{nd} pixel in a 64 pixel single FTIR tile) the images were adjusted with zero-padding, i.e. adding pixels with a value of zero to the edge of the image. Centering problems occurred rarely, and the amount of zero-padding required was calculated using the imageJ tomoJ software package. Other data, such as wavenumber axes information, was retrieved as a list of wavenumbers from ENVI header files ('*.hdr') generated by Res. Pro. (Appendix Listing 9.1).

2.4.2 Reconstruction

Spectral data processing and tomographic reconstruction algorithms specific to full-colour FTIR hyperspectral images were adapted from an existing monochromatic back-projection algorithm: the Matlab^{TM} implementation of the inverse Radon transform, 'iRadon()'[8].

[8]Empty brackets imply that this is a programming function.

Listing 2.1: Matlab Code Snippet – Reconstruction

```
%(unfiltered) back-projection
BackProjArray = iradon(input_images, theta, 'linear','none', 1, x);

%filtered back-projection
BackProjArray  = iradon(input_images, theta, 'linear','ram-lak', 1, x);
```

Run times were minimized by partially loading and reconstructing selected spectral ranges ('windowing'), rather than loading the entire spectrum in a single round.

2.4.3 Post-Reconstruction Processing

The reconstructed hyperspectral images outputted from the iRadon function were rotated -90°, to correct for the pre-processing rotation. If zero-padding was applied as a pre-processing step, the corresponding number of voxels were cropped off. These reconstructed images were stored as a four dimensional (x, y, z, $\bar{\nu}$) Matlab variable ('chromaticBackProjArray'). Empty voxels at the periphery were further cropped off the image for clarity as needed.

Retrieval of Intensity

The intensity of an infrared absorption at a particular wavelength was extracted from reconstructed hyperspectral data. If the coordinates of a desired voxel (x, y, z) were known, the intensity could be retrieved. This was accomplished with the script in Listing 2.2. In Listing 2.2, the variable 'WN' contains the list of wavenumbers that was retrieved before using Appendix Listing 9.1.

The intensity at a single wavelength for the entire reconstructed image could be retrieved as per Listing 2.4.

Listing 2.2: Matlab Code Snippet – Intensity at a wavenumber for one voxel

```
%Retreive the intensity of reconstructed absorbance at 1500 inverse cm
%for the voxel spectrum at coordinates (1,1,1);

%specify coordinates
x = 1;
y = 1;
z = 1;
%Find the index corresponding to the wavenumber 1500 inverse cm
target = 1500;
[closest_WN, WN_array_position] = min(abs(WN - target));
%Retrieve the Intensity from array of Backprojected spectra.
Intensity = chromaticBackProjArray(x, y, z,  WN_array_position);
```

Listing 2.3: Matlab Code Snippet – Intensity at a wavenumber for all voxels in the image

```
%specify the index of the wavenumber disired
WN_array_position = 1000;
%Retrieve intensities
Intensity_Image = chromaticBackProjArray(:, :, :, WN_array_position);
```

Retrieval of Cross-Sectional Slices

Reconstruction of the entire FTIR voxel spectrum was performed for select axial slices, across planes perpendicular to the rotation axis. Cross-sections in each of the three perpendicular planes (xy, xz, yz) could be extracted. Of these, the trans-axial plane (yz) was of primary interest as it could be used to assess the trans-axial resolution of the tomographic image.

Retrieval of One Voxel Spectrum

Individual voxel spectra were collected using the script in Listing 2.4. Select voxel spectra were exported to SPC file format ('*.spc') using the GSTools package (De Gussem, 2009) for compatibility with OMNIC Series Software (Thermo Fisher Scientific, USA).

Listing 2.4: Matlab Code Snippet – Intensity at all wavenumbers for one voxel

```
%Specify coordinates of desired voxel
x = 1;
y = 1;
z = 1;

%Retrieve the voxel spectrum at coordinate (1,1,1)
Voxel_spectrum = chromaticBackProjArray(x, y, z, :);
```

Integration of a spectral band

After reconstruction of spectral windows, integrated peak areas were computed for each voxel spectrum in the four-dimensional (x, y, z, $\bar{\nu}$) matrix of absorbance data.

Given a spectral peak, for example the one illustrated in Figure 2.8, one can perform integration with or without baseline correction.

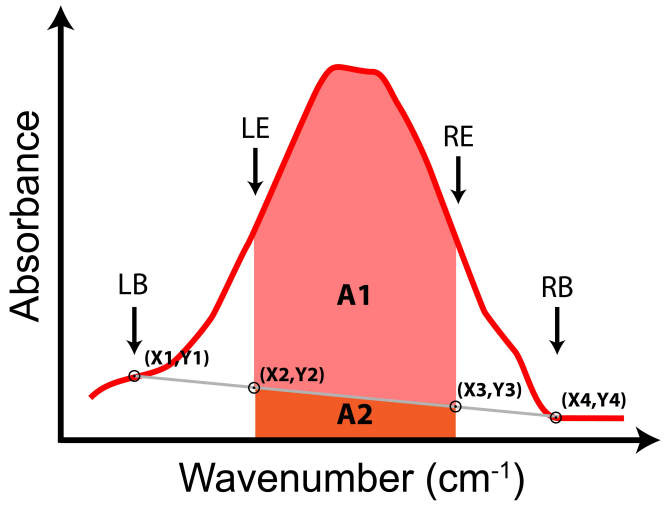

Figure 2.8: Integration of a spectral peak. Peak parameters that define the peak are the left edge (LE), right edge (RE), left baseline (LB) and right baseline (RB). Two areas (A) are shaded.

The left and right edge parameters were determined on the basis of full-width at half-height basis.

Integration Lacking Baseline-Correction Numerical integration was performed using the Matlab^{TM} implementation of Trapezoidal Rule Approximation. The area under a peak (e.g. Figure 2.8, A1 + A2) was calculated with Listing 2.5 and constitutes integration without baseline correction.

Listing 2.5: Matlab Code Snippet – Integration without baseline subtracted

```
% Integrate along wavenumber, the 4th dimension
A1andA2 = trapz(chromaticBackProjArray(:,:,:,RE:LE),4);
```

It is important to note that integration without baseline correction can emphasize edge scattering artifacts. This is not only true for conventional FTIR microspectroscopy resolved to two spatial dimensions, but FTIR micro-tomographic data as well. An example of this is shown later through the application of infrared tomography to the imaging of a buccal cell on a polyimide holder (Section 6, Figure 6.6).

Baseline-Corrected Integration A corrected area (Figure 2.8, A1 only) was calculated after subtraction of a baseline area as per Listing 2.6. As shown later in Section 6.3.1, baseline-corrected integration can reduce the appearance of edge scatter artifacts. In the case of 3D FTIR images, it eliminates a hollow appearance that plagued prior FTIR tomographic reconstructions (Martin et al., 2013; Quaroni et al., 2015). Hollow reconstructions are not congruent with the solid imaging subjects. One would not expect absorbances to be isolated to such a gossamer thin outer shell, unless there was a biological phenomenon to explain such a localization of chemicals.

2.5 Display

Slices of the reconstructed hyperspectral cubes resolved to three spatial dimensions were viewed using a Matlab Exchange package (Eckhard, 2013). Voxelated image data processed for various spectral bands were displayed as voxels in Matlab^{TM} using a 3D vol-

Listing 2.6: Matlab Code Snippet – Integration with baseline subtracted

```
%Calculate area under the baseline
m = (Y4-Y1)/(X4-X1); % calculate slope
b = Y1 - m*X1; % calc x-intercept using equation for a line
Y2 = m*X2 + b;
Y3 = m*X3 + b;
A2 = (Y2 + Y3)/2*(X3 - X2); % area2 = average height multiplied by width

%Subtract Area under the baseline from total integrated area
A1 = (A1andA2-A2);
```

ume rendering package (Woodford, 2011). The image voxels were false-coloured with a modified rainbow colour scale mapping (Figure 1.12) and an alpha transparency scale (0, transparent; translucent; 1, opaque).

Videos of voxelated renderings were exported using a Matlab Exchange rotating video recording tool (Jennings, 2013). Videos of isosurface renderings were exported from UCSF Chimera software (Pettersen et al., 2004).

Chapter 3. Validation

System testing, simulations and phantom imaging were performed in order to evaluate the efficacy of the methods. Computer generated and experimental FTIR tomographic data sets of standardized imaging targets were processed as per the Chapter 2 methods.

3.1 Simulation

3.1.1 Digital Modeling of an Absorptive Object

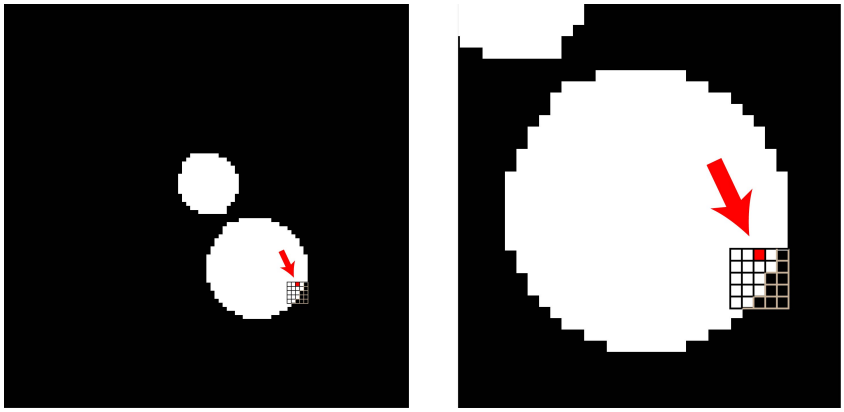

(A) Image **(B)** Zoomed-in region

Figure 3.1: Pixelated black and white image. One pixel is highlighted in red. Adapted from Findlay et al. (2017).

A black and white 2D image was created (Figure 3.1). Copies of this image were stacked to form a 3D object with two irregularly shaped elongated structures obliquely oriented to one another (Figure 3.2). Entirely black images were stacked on either end of the structures. Object voxels were assigned absorption constants (Figure 3.3) for the mid-infrared region resulting in a hyperspectral data structure (Figure 3.4). The absorption constants were simulated using a Gaussian curve with an area equal to unity (Figure 3.5).

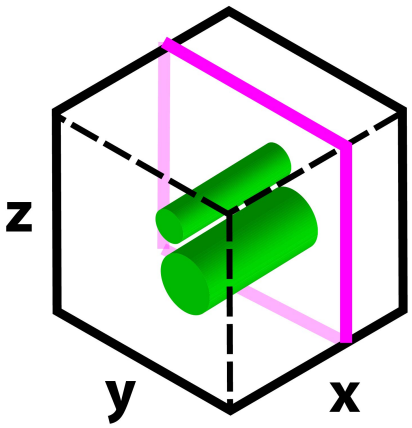

Figure 3.2: Image of a simulated multidimensional (x, y, z, $\bar{\nu}$) object consisting of two absorptive masses (one small, one big, obliquely adjacent) that are each roughly cylindrical. One axial slice through the object is framed in pink. Adapted from Findlay et al. (2017).

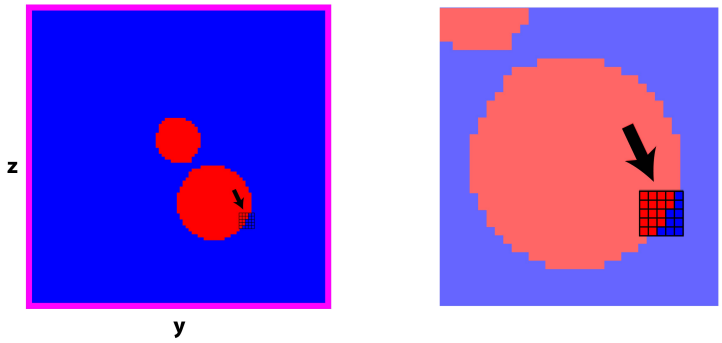

(A) Image **(B)** Zoomed-in region

Figure 3.3: **(A)** Axial slice (y, z, $\bar{\nu}$) of the 3D simulated object from Figure 3.2. Voxels occupied by the object are red and simulated to be infrared absorptive. Unoccupied voxels are blue and simulated to have zero absorbance. **(B)** Grid overlaid on a zoomed-in 5 by 5 voxel region of the slice. The rest of the image is faded for clarity.

Listing 3.1: Matlab Code Snippet – Simulated Voxel Spectrum Peak

```
sigma = 2; %define a parameter for a Guassian curve
WN = 1:0.1:20; %define 20 different values
GAUSS = 1/(sqrt(2*pi)*sigma)*exp(-0.5 *(WN-10).^2/(sigma^2)); % equation
Intensity = GAUSS ./ 10; % normalize
```

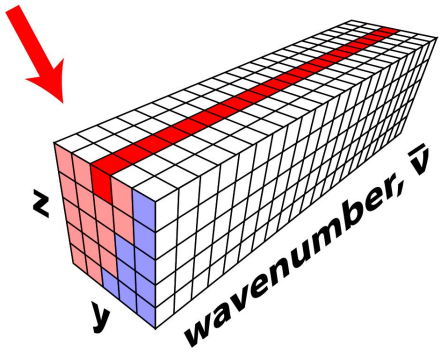

Figure 3.4: Data structure (y, z, $\bar{\nu}$) associated with a 5 by 5 voxel region of an axial slice of the simulated object. One voxel spectrum is highlighted in red.

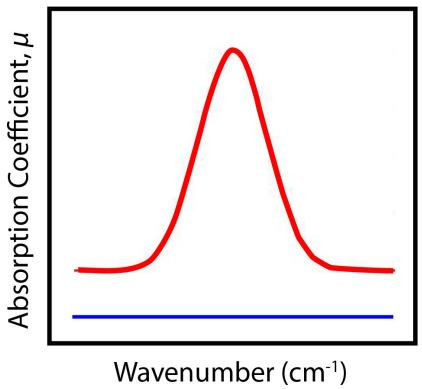

Figure 3.5: Absorption coefficients corresponding to simulated data $\bar{\nu}$ dimension. Red and blue simulated spectra correspond to voxels with and without the simulated absorbing object, respectively. Offset for clarity.

3.1.2 Simulation of Projections

Projections of the simulated object were calculated with the Matlab^{TM} implementation of the Radon transform: 'radon()'. An example of the use of radon() is shown in Figure 3.6. The resulting simulated hyperspectral data cubes (row, column, wavenumber) were resolved to two spatial dimensions. Simulated tomographic data sets (N views at $\Delta\theta$ angle intervals) were generated with one hyperspectral data cube (X, Y, $\bar{\nu}$) simulated for each viewing angle.

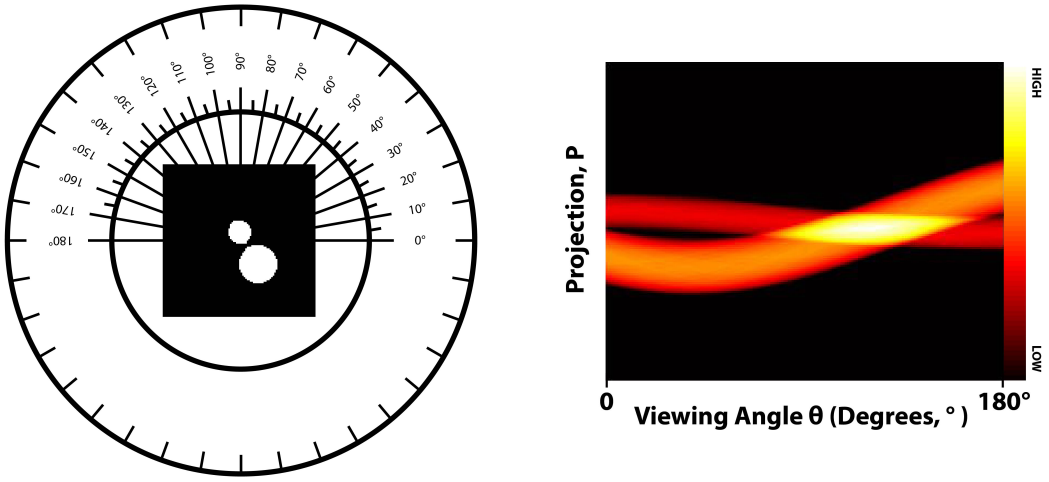

(A) Imaging Subject. **(B)** Sinogram.

Figure 3.6: Projection of **(A)** an axial slice of the simulated imaging subject from Figure 3.2 was input into Matlab^{TM} ('radon()') for the calculation of non-redundant projection at angles from 0 to 180°. The projections are displayed as **(B)** a sinogram. Projection values are mapped to a default Matlab colourscale (high: white; low: black).

3.1.3 Reconstruction from Simulated Projections

The inverse Radon transform (iRadon), with and without filtering, was applied to the simulated projections as per the Section 2.4.2 methods.

Unfiltered Back-projection

Back-projection of the simulated object essentially involves the smearing of projections back toward the source of the projection (Figure 3.7). Back-projections of a monochromatic axial slice of the simulated object were calculated using two simulated tomographic data sets with different angular sampling: one with 4 views and one with 180 views equally spaced between 0 to 180° (Figure 3.8). The back-projections are smeared and linearly super-imposed. Using only 4 views created a crude image that only vaguely resembled the original object. In contrast, the 180-view reconstruction was much improved. A star artifact associated with back-projection is readily apparent in the 4-view reconstruction. The point spread function (PSF) typical of back-projection can be seen in the edges of the 180-view reconstruction, which are blurred.

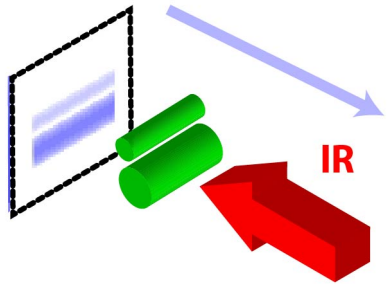

Figure 3.7: Infrared radiation (IR, red arrow) is transmitted through an attenuating object and forms an image on a detector. The blue arrow indicates the direction back toward the lightsource.

Reduction of noise

As described before, linear superposition occurs during back-projection. Other forms of tomography, such as positron emmision tomography (Bailey et al., 2005), employ back-projection to increase sensitivity and signal-to-noise ratio (S/N) .

Randomly generated values were added to projections of the simulated object using a Matlab script (Listing 3.2) in order to simulate spectral data with a low S/N (Figure 3.9). The linear super-position of random spectral noise from the different views cancels, re-

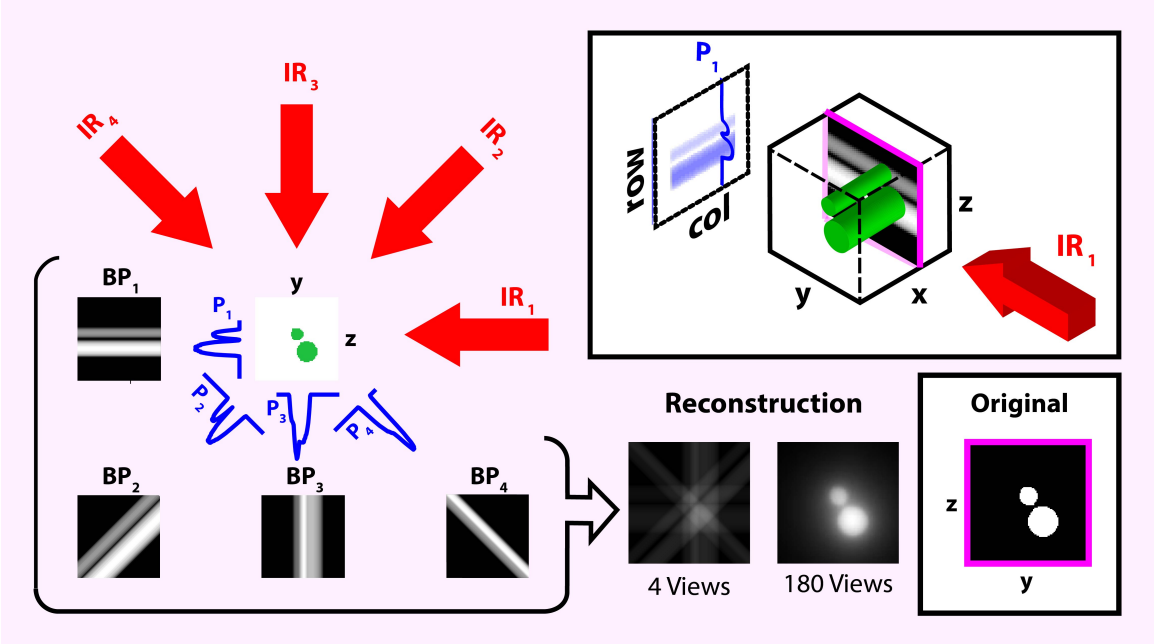

Figure 3.8: Backprojection of images. Simulation of infrared radiation **(IR, red)** transmitted through attenuating matter **(object, green)** at a particular angle (no. 1, 2, 3 or 4). A projected image **(P, blue)** formed on a detector and is linearly smeared to form backprojections **(BP, gray-scale)**. The BP shown here are used to reconstruct a crude image (BP 1–4: 4 views, 45° intervals). Additional BPs (180 views, 1.5° intervals) can be reconstructed into an image that better resembles the original object. Only projections of a single exemplar axial slice (pink) are shown for clarity. Though spectral images are used for FTIR microtomography, monochromatic projections are shown here for ease of explanation. Adapted from Findlay et al. (2017).

sulting in an improvement to the S/N. This noise reduction effect was later applied in the imaging of diatoms (Figure 5.7).

Listing 3.2: Matlab Code Snippet – Simulating Voxel Spectrum Peak

```
for wavenumber = 1:201
    % Project the simulated object using the Radon transform
    P = radon(chromaticBackProjArray(x, :, :, wavenumber), 0:1.5:180);
    % create random noise such that S/N = 1
    randnoise = rand(145,121) .*0.3 -0.15;
    %add noise to the projections.
    P = P + randnoise;
    %reconstruct with unfiltered back-projection
    Reconstructed_Img = iradon(P,0:1.5:180,'linear','none');
    %collect the resulting reconstructions for all wavenumbers
    chromatic_Reconstructed_Img(:,:,wavenumber) = Reconstructed_Img;
end
```

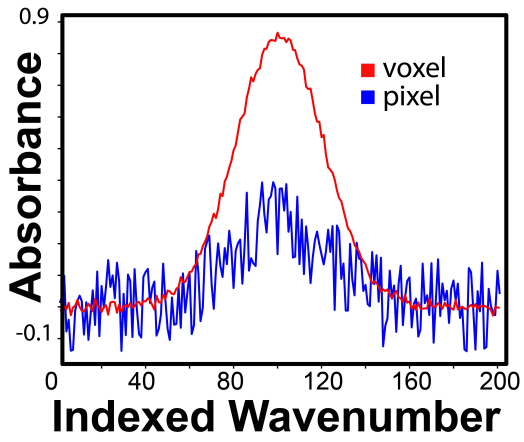

Figure 3.9: Spectra resulting from the reconstruction of noisy simulated spectra with unfiltered back-projection. (Blue) Typical pixel spectrum input into 'iradon()' (Matlab™, inverse Radon transform function). (Red) A reconstructed output voxel spectrum. Adapted from Findlay et al. (2017).

Filtered Back-Projection

A filter, such as the Ram-Lak filter, can be applied to back-projected images in order to reduce the blur associated with the back-projection PSF. The filtered and unfiltered reconstruction methods (Section 2.4.2) were applied to simulated projections. The unfiltered

reconstruction (Figure 3.10A) is brighter and has more blur than the filtered reconstruction (Figure 3.10B). The filter has removed some of the low spatial frequency signal associated with the blurring artifact, at the cost of image brightness. The remaining high-frequency details (Figure 3.10B, two gray shapes) have lower contrast to the image background (black). The high spatial frequency noise (Figure 3.10C, different shades of gray) has been amplified, i.e. made more prominent with respect to the background. An example of this noise amplifying effect can be seen with buccal cell tomographic images in Figure 6.9.

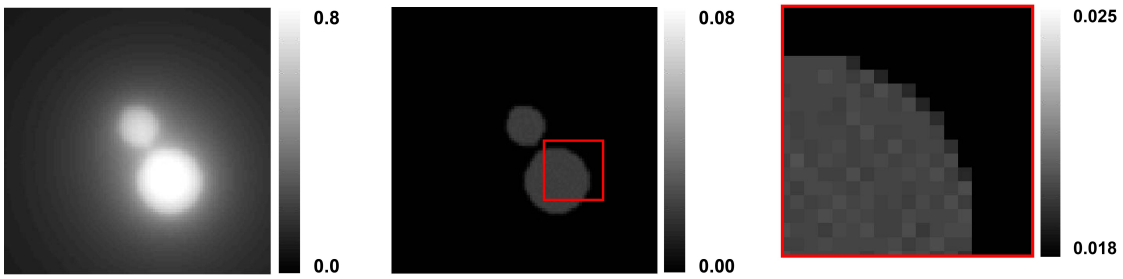

(A) Unfiltered. **(B)** Filtered. **(C)** Filtered, Zoomed-In.

Figure 3.10: Images generated from **(A)** back-projection and **(B)** filtered back-projection of a simulated tomographic data set (100 views, $\Delta\theta = 1.8°$) composed of Radon projections of an axial cross-section of the simulated object. The red box on B indicates the area that was zoomed-in on to create C. (C) A close-up view of pixel-to-pixel noise.

3.1.4 Rotation Direction

Inconsistent registration of turn directions between hardware and software was simulated. The Matlab^{TM} default Shepp-Logan phantom (Figure 3.11A) served as a digital proxy to an imaging subject where absorbance varies with position inside the object. Projections were calculated from the phantom to mimic those obtained when an imaging subject is rotated CW or CCW. The CW and CCW data were each registered to positive viewing angles and reconstructed in order to explore the effects on a tomographic image. The CCW reconstruction (Figure 3.11B) recapitulated the original image, but the CW reconstruction (Figure 3.11C) was mirrored. Reversal errors are common to other forms of computed

tomography, including medical scans where they can lead to wrong-sided surgery and malpractice suits (Schmidt and Odland, 2004).

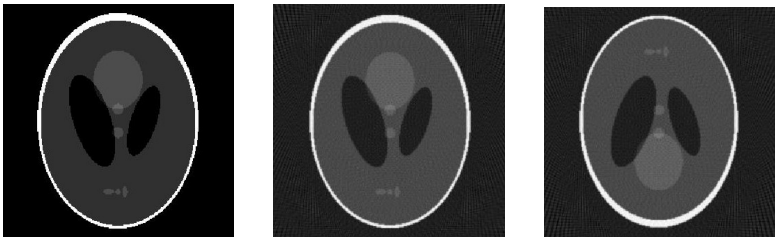

(A) Digital Phantom. **(B) CCW**. **(C) CW.**.

Figure 3.11: Image error stemming from inconsistent registration of turn directions. **(A)** The default Matlab phantom reconstructed with **(B)** positive CCW or **C)** positive CW angles.

3.1.5 Simulation of Angular Error Associated with Stepper Motors

The output shaft of the NEMA 8 stepper motor of the tomography accessory prototype Mark I turned 1.8° with each step. As specified by the manufacturer, the angular error associated with this stepper motor is at most ±5% of a step. A simulation was built to model this error (Listing 3.3).

Reconstructions of data with (Figure 3.12) and without (Figure 3.10) angle error were compared and found to be nearly identical. Small differences between the reconstructions were not readily noticeable due to the small and non-cumulative nature of the angle error and the level of pixelation in the input images. In short, the results of the simulation suggest that stepper motor error should not produce noticeable imaging artifacts.

Listing 3.3: Matlab Code Snippet – Simulation of Error

```
theta = 1.8:1.8:180; % define the viewing angles
error_in_step = (rand(1,100) * 2 - 1) *0.05* 1.8; % generate 5% error
theta_with_error = theta + error_in_step; % add error to viewing angles
[R,xp] = radon(I,theta_with_error); % calculate the projections
```

For contrast, a simulation of extreme angular error with noticeable effects on on the resulting reconstructed image is shown in supplemental Figure 9.3.

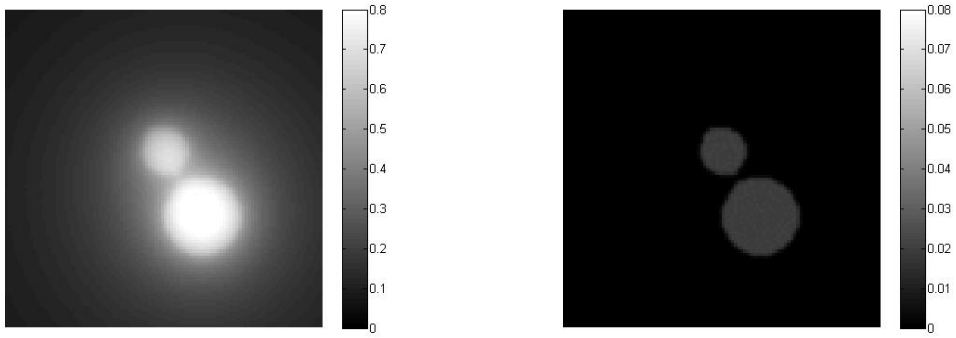

(A) Unfiltered. **(B)** Filtered.

Figure 3.12: Reconstruction of simulated projections (100 views, $\Delta\theta = 1.8°$) with $\pm 5\%$ of a step angular error by a) back-projection and b) filtered back-projection .

3.1.6 Angular Sampling

The stepper motor angle interval for tomography accessory prototype Mark I was fixed at an angle of 1.8°, or multiples thereof, which created incompatibility with the minimum angular sampling scheme calculated in Section 2.2. The calculated scheme warranted 81 projections between 0 and 180°. The various prototype Mark I compatible angular sampling schemes used in Section 3.2 and Part II were simulated and closely resembled the results in Figure 3.12. This suggests that these angular sampling schemes are sufficient for the applications presented later.

3.1.7 Parallel Versus Fan-Beam Projection

The magnitude of fan-beam distortion depends on the object distance from the light-source (Cole et al., 2009). In practice, an FTIR microscopy light-source, sample and detector would not be positioned adjacent to one another. For illustrative purposes, extreme fanning was simulated.

Beams of collimated light in the parallel configuration (Figure 3.13A) were simulated with the Radon transform. Radiating beams of light in the fan-Beam configuration (Figure 3.13B) were simulated with the Matlab^{TM} implementation of the fan-beam transform ('fanbeam()').

The 2D spatially resolved images resulting from the focused IR light being brought to the FTIR microscope focal plane array (FPA) detector was approximated as a parallel projection for the purposes of this thesis.

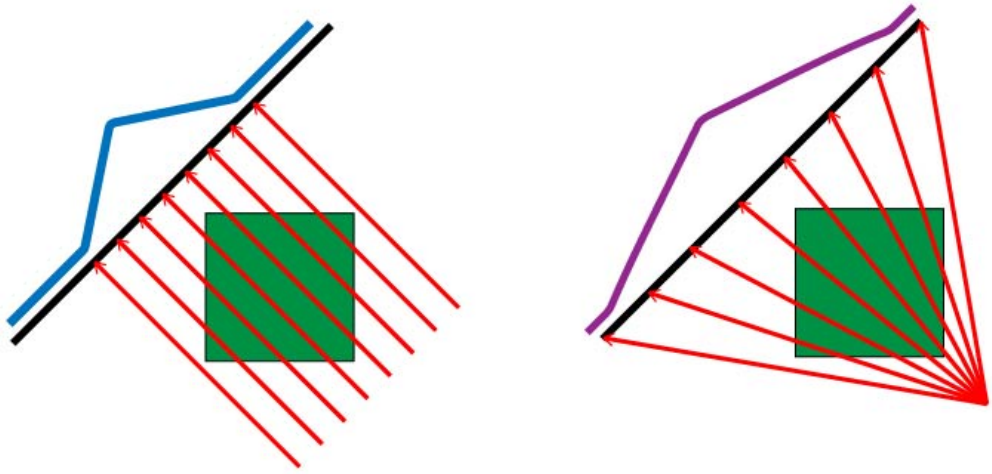

(A) Parallel beam projection.

(B) Fan beam projection.

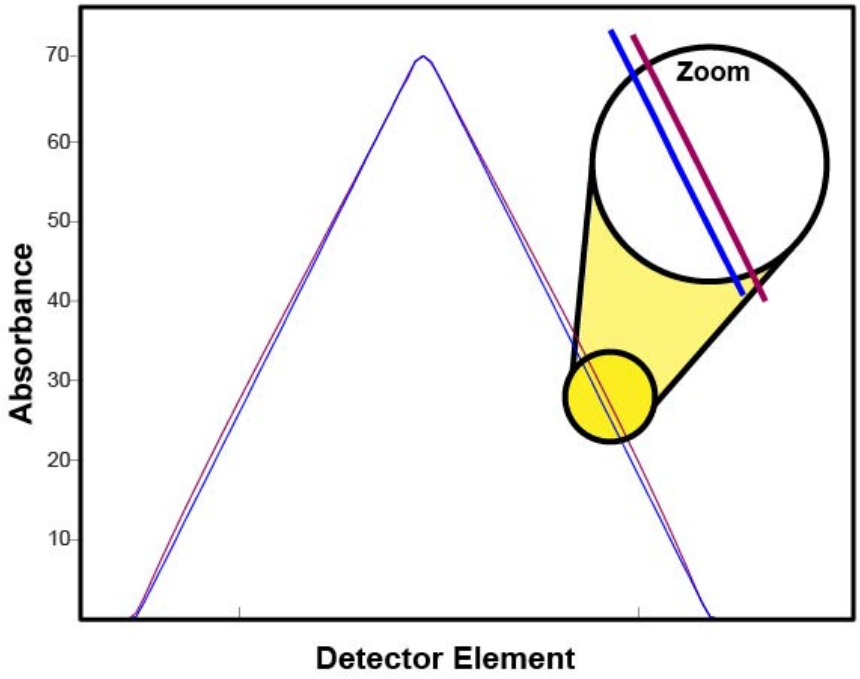

(C) Comparison of projections.

Figure 3.13: Simulated fan-beam projection. Infrared light (red) passes through a simulated square absorptive object (50 x 50 pixels) with each pixel assigned a μ of 1. The path of light through the object follows either a A) parallel beam or B) fan-beam geometry. The light is attenuated and strikes the detector (black line), forming projections (P). C) Projections from (**blue**) parallel beam and (**purple**) fan-beam geometry simulations are scaled horizontally and overlaid for comparison.

3.2 Resolving a Standardized Imaging Target

3.2.1 Introduction

Reference materials, such as those released by the National Institute of Standards and Technology (NIST), are indispensable tools for validation of precise and accurate imaging. Size reference materials serve to calibrate measurements made of commercially available manufactured size standards, such as polystyrene microspheres (PSMs). Results can be related through an unbroken chain of documented calibrations so that measurements are traceable to standards developed and maintained by NIST.

PSMs can be used as standardized imaging targets for FTIR imaging resolved to two spatial dimensions (Nasse et al., 2011b; Holman et al., 2010). For this, among other reasons, a doctoral thesis investigation of the physical performance characteristics of the first ever FTIR microtomography system was performed at IRENI using 200 μm diameter PSM size standard beads (Alavi, 2015). Such imaging serves to evaluate and analyze the performance of novel devices and methods.

The purpose of the imaging in this section was to evaluate the spatial resolution along the z-axis (longitudinal direction). Here a variation on the size standard bead testing is performed, with the creation of a specially designed object: a 'phantom' as it is termed in the realm of medical radiology. The polymer phantom imaged here consisted of a single strand incorporating $6\,\mu$m diameter polystyrene size standardized microspheres and another contrasting agent, polyvinyl alcohol.

3.2.2 Method

Uncoated strand

PSMs (NIST size traceable $6.0 \pm 0.24\ \mu$m diameter) were acquired as an aqueous suspension of 2% solids (Magsphere Inc.). A droplet was applied to a microscope slide for visual

inspection.

A 4% (wt/vol) mixture of powdered polyvinyl alcohol and water was prepared beforehand and left in a 50°C incubator overnight to aid dissolution. Equal volumes of the microsphere suspension and a 4% (wt/vol) solution of polyvinyl alcohol (PVA, 88000–98000 mol. wt, 99+%, Aldrich Chemistry, not spectral grade) were mixed. A droplet of the mixture was again applied to a microscope slide for visual inspection. Strands of PSM-laden PVA were drawn from the solution, captured on a wire and dried overnight.

Coated strand

PSM-laden strands prepared as per the description in the above 'uncoated strand' subsection were dipped in PVA, in order to apply an extra coating of PVA and ensure a full encasement of each PSM within PVA. The strands were again allowed to dry overnight.

Image Acquisition and Processing

The strand-laden wire was mounted into the Mark II prototype tomography accessory for FTIR imaging. Data were acquired and processed as per the Sections 2.1 and 2.4 protocols, respectively. The baseline-corrected peak parameters for integration are shown in Table 3.1.

Table 3.1: Polystyrene and polyvinyl alcohol phantom peak parameters.

Band	**Peak Centre** (cm^{-1})	**Left**		**Right**	
		Baseline, LB (cm^{-1})	**Edge,** LE (cm^{-1})	**Baseline,** RB (cm^{-1})	**Edge,** RE (cm^{-1})
=C–H (PSM)	3021	3038	3038	3010	3010
C–OH (PVA)	1088	991	991	1160	1160

3.2.3 Results

PSM solutions

The deposition of the colloidal PSM suspension mixed with the PVA solution (1:1 v/v) onto a glass microscope slide surface resulted in the spherical particles self-assembling into a hexagonal close-packed arrangement. The uniformity of the spheres was still visible upon inspection as the clumping of the microspheres only occurred on a 2D plane, forming a monolayer. (Figure 3.14). The particles maintained their spherical morphology

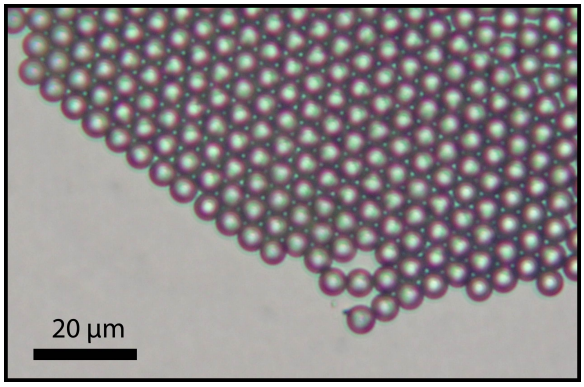

Figure 3.14: Visible light image of a sample of polystyrene microsphere (PSM) solution dried on a microscope slide.

when the PSM solution was mixed with the PVA solution and did not clump together (Figure 3.15). The in-focus microspheres were visually compared to a micrometer to ensure that no swelling occurred.

Uncoated strand

The uncoated strands dried to a final diameter similar to the PSMs. Though the microspheres exhibited low colour contrast under visible light, their positions could be determined from visible light image (Figure 3.16A). Microspheres protruded from the strand at random intervals. Some microspheres were in contact with adjacent microspheres while others were well separated. FTIR imaging resolved to two spatial dimensions revealed the

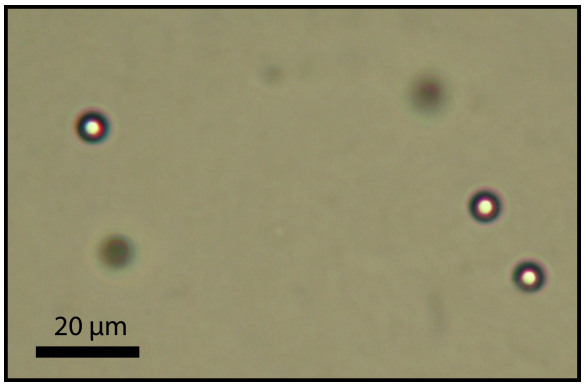

Figure 3.15: Visible light image of the mixture of PSMs and PVA. Microspheres that are in focus and out of focus appear as light and dark circular shapes, respectively.

PVA and polystyrene within the strand had spectral contrast in the mid-infrared region (Figure 3.16BC). Pixel spectra from the body of the strand resembled that of pure PVA (spectra not shown), with a strong absorbance band centred at 1100 cm^{-1}. Pixel spectra from the area with PSM in the strand also resembled PVA, but had an additional weak absorbance at 3020 cm^{-1} (Figure 3.16D). The peak at 3020 cm^{-1} was absent from the spectra from the body of the strand (Figure 3.16E), but matched the 3020 cm^{-1} peak of pure polystyrene (Figure 3.16F). The region in Figure 3.16 underwent further FTIR imaging resolved to two spatial dimensions, as part of the collection of multiple views composing a tomography data set. In some views, such as the one in Figure 3.17B there were scattering artifacts in the data, revealed by our integration parameters. The peak at 3020 cm^{-1} was obscured by a rolling baseline (Figure 3.17C). The sets with inconsistent data were input directly in the image reconstruction process to assess the effects of doing so. (Figure 3.18).

The PVA and polystyrene within the strand (Figure 3.18A) was reconstructed and had spectral contrast in the mid-infrared region that could be resolved to three spatial dimensions (Figure 3.18B). Voxel spectra from the body of the strand resembled that of pure PVA (spectra not shown), with a strong absorbance band centred at 1100 cm^{-1}. Voxel spectra from a region with a PSM resembled PVA; however, a weak absorbance at 3020 cm^{-1} was also present.

The peak centre at 3020 cm^{-1} was neatly positioned between other more intense bands

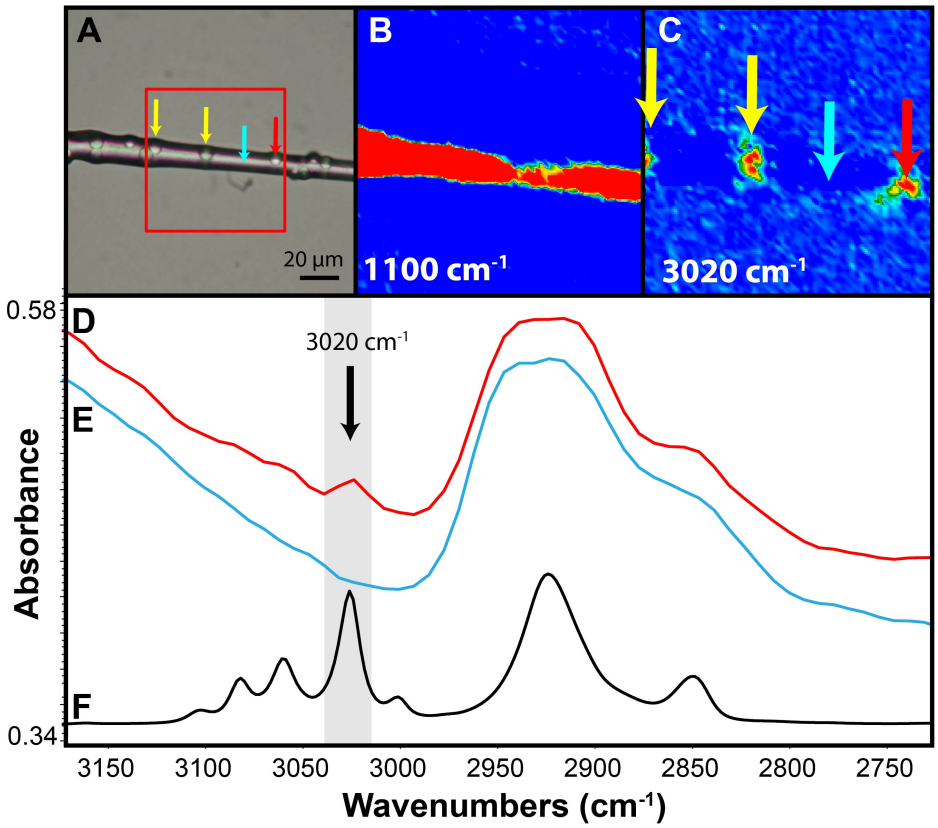

Figure 3.16: 2D FTIR imaging of a phantom consisting of PSMs in a PVA strand. **(A)** Visible light image with red box indicating area further imaged with FTIR. False-colour FTIR images processed for baseline corrected integration of proxy bands for **(B)** PVA (1100 cm^{-1}) and **(C)** polystyrene (3020 cm^{-1}). The **red** and **blue** arrows indicate the position of selected representative voxel spectra from the strand **(D)** with and **(E)** without a PSM present, respectively. **(F)** A reference spectrum of pure polystyrene.

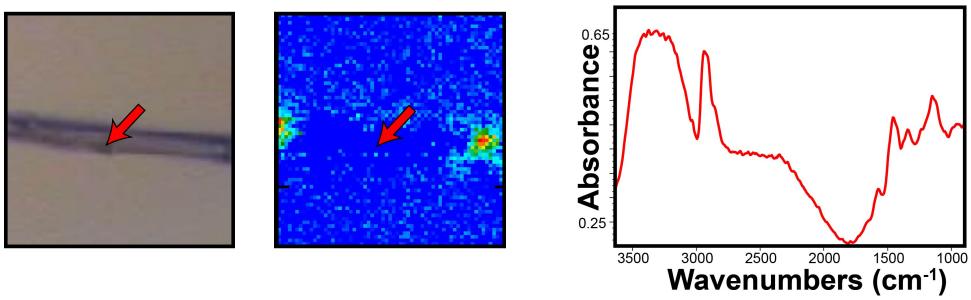

(A) Visible **(B) FTIR** **(C) Spectrum**

Figure 3.17: Large amounts of Mie scattering apparent in a 2D FTIR image of the same uncoated phantom shown in Figure 3.16 after 122.4° rotation to different viewing angle. **(A)** VIsible light image. **(B)** Data was false-colour processed for the peak at 3020 cm^{-1}. The red arrow in **B** indicates the location of **(C)** a pixel spectrum from the part of the image where the centre PSM is expected to be.

and was not obscured in most pixels. (Figure 3.18C). The maximum area of the peak[1] at 3020 cm^{-1} was lower for the central bead than for the other beads, due to changes to its peak maxima by broad sloping baseline features, i.e. Mie scattering artifact (Figure 3.18). The sloping baseline caused the peak centre to deviate from 3020 cm^{-1} , making the integration parameters ill-fitting.

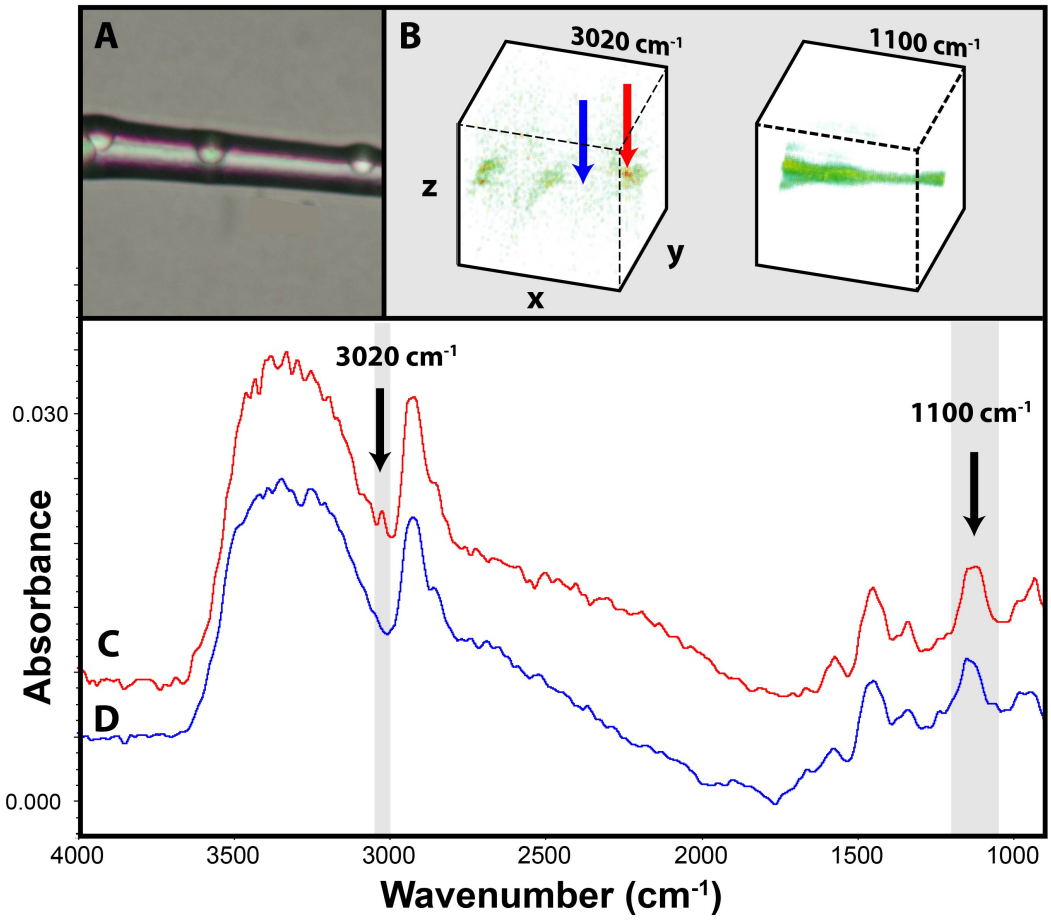

Figure 3.18: FTIR tomographic imaging of uncoated PSM in PVA strand. **(A)** Visible light image of polyvinyl alcohol strand containing PSMs (6 µm diameter) selected for tomographic imaging. A tomographic data set (64 × 64 pixels per tile, one tile per view, 27 views, $\Delta\theta = 7.2°$ view angle interval) was acquired of this region of the sample. **(B)** FTIR images resolved to three spatial dimensions, reconstructed using filtered back-projection method. False-colour images were processed for baseline-corrected integration of bands at 3020 cm^{-1} and 1100 $cm.^{-1}$ Voxels at locations marked with **red** and **blue** arrows were selected to show representative voxel spectra of **(C)** the PSM in PVA and **(D)** the PVA strand without microsphere present, respectively.

[1] calculated with the same integration and baseline correction parameters

Coated Strand

A further coating of PVA to the strands increased the overall diameter to $\sim 15\,\mu\mathrm{m}$ (Figure 3.19A). The microspheres did not protrude from the PVA coating. The 3020 cm^{-1} peak was apparent from all views and no disruptive scattering artifacts were obvious. There were no frames in which the integration parameters were obviously ill-fitting upon inspection. After filtered back-projection was applied and the resulting image was processed (Figure 3.19B), the reconstructed peak area maxima were more consistent across the two microspheres imaged (Figure 3.20).

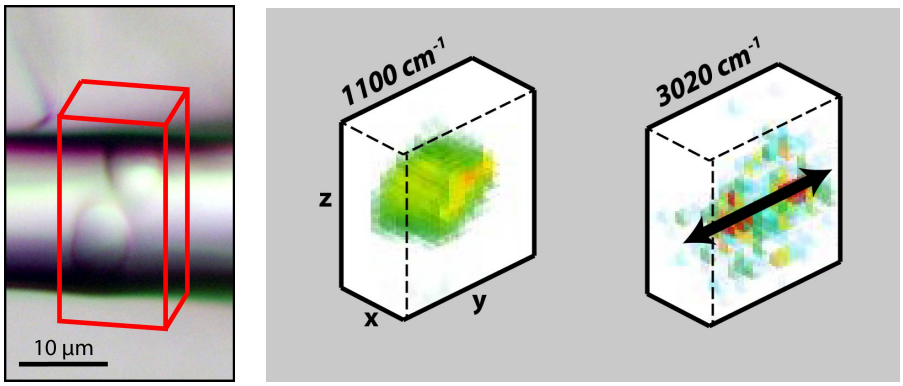

(A) Visible **(B) FTIR**

Figure 3.19: Spatially 2D FTIR image of two PSMs fully embedded in a PVA strand. Image has been cropped to 17 $\times$ 25 $\times$ 25 voxels (1.1 $\times$ 1.1 $\times$ 1.1 μm^3 per voxel) for clarity.

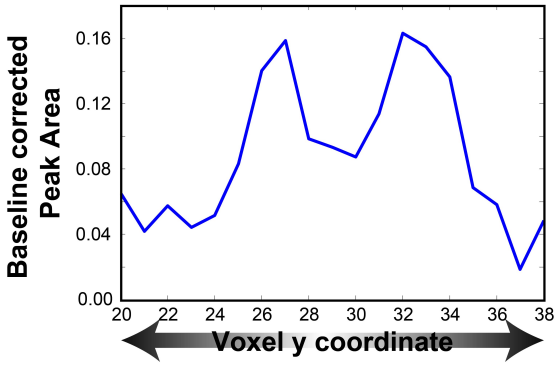

Figure 3.20: Profile of spectra through two PSMs. The baseline-corrected peak area for the 3020 cm^{-1} peak was calculated for each of the voxel spectra along the black double arrow in Figure 3.19B. The two largest local maxima correspond to the centres of two PSMs.

3.2.4 Discussion

The PSMs have a monosize appropriate for their role as imaging standards. The $6\,\mu\mathrm{m}$ diameter employed here are similar in size to subcellular structures (e.g. chloroplasts, nucleus) in cells imaged later in Part II.

It is clear from the FTIR images resolved to two spatial dimensions (Figure 3.16) that there is not much contrast between the polystyrene and the PVA surrounding it. However, the PVA effectively held the microsphere in the field of view for imaging.

The PVA and polystyrene are co-localized in microsphere pixels, but image data resolved to two spatial dimensions (Figure 3.16) does not unambiguously show that the PVA lies within the microspheres. Considered alone, the 2D imaging leaves the possibility that the PVA is above or below the polystyrene.

Polystyrene molecules (Figure 3.21) have many bands, including one absorbance band at 3020 cm^{-1} that corresponds to an unsaturated =C–H stretching vibration.

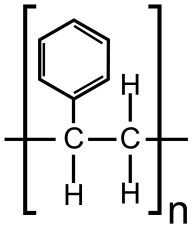

Figure 3.21: Generalized molecular structure of polystyrene.

Polystyrene can be synthesized with low density cross-linked structures via the inclusion of divenylbenzene. Pores large enough to accommodate PVA molecules (Figure 3.22) could allow the PVA to enter the sphere via capillary action, rather than remain excluded. A void area lacking PVA absorbances would be expected if the sphere was impermeable to the coating and if absolutely no bleeding of signal between voxels occurred.[2]

The air surrounding the strand has a lower refractive index ($\sim$1, Mathar (2007)) that is mis-matched to that of polystyrene ($\sim$1.6, Jitian (2011)). If the microsphere protrudes

[2] An example of a truly void area is shown later in Section 4.1, Figure 4.8.

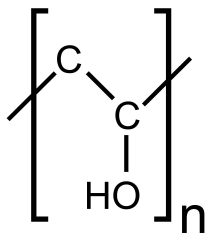

Figure 3.22: Molecular structure of polyvinyl alcohol.

from the strand, as might be the case with the centrally positioned bead in the uncoated strand, the polystyrene is interfaced with the surrounding air. Larger differences between refractive indexes increases scattering effects associated with an interface, especially in images captured at viewing angles obliquely oriented to an object's surface. Scattering, such as that evident in Figure 3.17, is not accounted for and does not fit the reconstruction methods used here.

As noted previously, in some models of tomography there is an assumption that light moves in straight lines through the imaging subject to create an undistorted projection, i.e. is not diffractive. Given the inapplicability of the reconstruction model to the scattering in this tomographic data set, it is not surprising that the central PSM appears artificially faint relative to the right most PSM when the data set is reconstructed (Figure 3.18).

The extra coating of PVA was applied in order to eliminate polystyrene-air interfaces. The coating resulted in less scatter, and a better reconstruction (Figure 3.19) with similar 3020 cm^{-1} intensity maxima for each of the microspheres.[3] Matching the refractive index of the imaging subject to its surrounding medium increased the applicability of non-diffractive models (e.g. Radon projections) to infrared microtomography, as it reduced scattering at the interface of the imaging subject and atmosphere. The capability of FTIR microtomography methods to discern two coated microspheres located on the same trans-axial (yz) plane is evident in Figure 3.20. The two peaks that appear in Figure 3.20 are clearly overlapping and the dip between them is approximately half their height, which would mean that the

[3]The IR scatter reducing effect of coatings is best demonstrated in Chapter 4 with a different sample, PVA-coated spider silk.

Rayleigh criterion has been met; however the noise associated with the data makes such a determination uncertain.

3.2.5 Conclusions

The spectral contrast between polystyrene and PVA permitted the construction of phantoms on which to test FTIR tomographic imaging. The refractive indexes of the media in and around the phantoms caused them to display different degrees of scattering effects. Polystyrene size standard microspheres were not clearly captured by either 2D or 3D spatially resolved FTIR images when scatter occurred. Imaging subjects with diameters small enough to exhibit Mie scatter were particularly challenging, and are intractable without intervention.

It was possible to reduce infrared tomographic imaging artifacts and partially accommodate for irregular sample morphology by minimizing scatter with the application of refractive index matched coatings. Once scattering issues were resolved, improved 3D spatially resolved FTIR images were attainable. The utility of the FTIR microtomography technique for imaging 6 micron diameter polystyrene beads was demonstrated. The contrast and spatial separation of $6\,\mu\mathrm{m}$ microspheres was observable in a voxelated FTIR spectral image.

It is clear that the FTIR microtomography methodology and phantom imaging are by no means optimized at the present time, but advances are important as they serve to increase the legitimacy of FTIR microtomography as an imaging technique.

Part II

APPLICATIONS

Chapter 4. Imaging of Spider Silk Fiber

4.1 Background

4.1.1 Spider Silk

Spider silks are novel imaging subjects for FTIR microtomography. These protein threads are semi-crystalline with highly organized anti-parallel β-sheet nanocrystals embedded in an amorphous matrix. In nature, silk protein (fibroin) is spun into threads by a spider after being secreted from specialized glands. Though these biopolymers can be light-weight gossamer and delicate in appearance, spider silk is, weight for weight, tougher than steel and has other robust mechanical properties such as stickiness, tensile strength and toughness (Gosline et al., 1986).

The banded garden spider, *Argiope trifasciata*, spins different silks for different applications. Of these, its aciform (wrapping) silk, used to immobilize prey, is pound-for-pound the toughest form, with strength that exceeds that of Kevlar^{TM} (Weatherbee-Martin et al., 2016).

Spiders have pairs of movable organs called spinnerets that can telescope and impart a unique mechanical treatment to threads excreted from silk producing glands. One function of the spinneret is to stretch silk, a process which increases silk strength. The increase in strength that occurs after stretching is likely partially due to strain-induced promotion of molecular alignment (Weatherbee-Martin et al., 2016).

Humans have captured live spiders from the wild and hand drawn silk threads from their spinnerets in an inefficient and laborious process referred to as 'silking'. As spiders are not readily domesticated, due to their aggressive territorial behaviors and cannibalistic tendencies, the natural spider silk supply is not a viable source of fiber for practical and widespread usage by humans. (Rech and Arber, 2013; Scheibel, 2004)

Artificial Spider Silk

Artificial manufacture has the potential to be an effective method for mass-producing the principal protein in spider silk fiber: spidroin. Researchers endeavor to spin spidroin into artificial fibers that faithfully recapitulate the desirable properties of natural forms of spider silk. The actions of spinnerets are partially mimicked by incorporating post-spin stretching into manufacturing protocols for artificial spider silk (Weatherbee-Martin et al., 2016).

FTIR Imaging of Spider Silk

The first report of 2D FTIR microspectroscopic imaging to characterize single natural silk fibers employed a synchrotron light source (Ling et al., 2011). The first 3D FTIR microtomographic imaging of spider silk also employed a synchrotron light source and was reported as part of a doctoral thesis by Imtiaz (2015). Scattering artifacts were noted in these reports, and, to the date of this thesis, it does not appear that this problem has been definitively solved. The computer algorithms for scattering correction employed by Imtiaz (2015) are among the best currently available, yet they still incorporate input parameters that are somewhat arbitrarily defined at the user's discretion. Such parameters are adjusted until the results look 'right'. An empirical scatter correction result is desired.[1]

In initial discussions between Dr. Jan Rainey and Dr. Kathleen M. Gough there was hope that FTIR microtomography could identify protein conformational changes due to different protein selections, spinning and post-treatments. It became clear that scattering artifacts obscured the spectra of samples of post-spin stretched silk, and made such determinations impossible, with the FTIR microtomography methods available. The scope of the spider-silk project changed to finding a novel method with which to improve the quality of spider-silk transmission-mode FTIR absorbance spectra.

To this end, the FTIR microtomographic imaging technique was applied as part of an

[1] Scatter-free experimental measurements could help guide optimal correction, where correction is required.

empirical solution to the scattering of infrared light by samples. Biological samples such as spider silk often have refractive indexes that are larger than the air surrounding them. The interface between the air and the oblique surfaces of small or irregularly shaped samples can scatter light. Artifacts of scattering make a sample imaging subject less suitable for transmission mode FTIR imaging. As demonstrated in Part I, Section 3.2, one can effectively eliminate the air-sample interface by coating samples with a material that has a similar refractive index. Using 2D imaging, it would be difficult to separate the FTIR spectra of this coating from that of the sample without sectioning, grinding or otherwise applying physical force. The spectra of both coating and sample would be detected in pixels together. With tomographic FTIR imaging, one can attempt to resolve the FTIR spectra of the coating from that of the sample in 3D, with the separated signatures occurring in different voxels. This is theoretically possible, if the imaging subject that is coated is impermeable to the coating substance. In this chapter, coatings are explored as part of a FTIR microtomography method with which to obtain undistorted transmission spectra from a sample that normally scatters infrared light to a disruptive degree. Furthermore, polarization contrast microtomographic FTIR imaging of coated samples is introduced as a method to verify band assignment of reconstructed absorbance spectra.

4.2 Methods

4.2.1 Fibre Production

Fibre manufacture by Nathan Weatherby-Martin took place in the laboratory of Prof. Jan Rainey (Dalhousie University, Nova Scotia) with methodology modified from Weatherbee-Martin et al. (2016) as summarized in 9.5. was shipped to the UofM for FTIR imaging.

4.2.2 Sample Preparation for FTIR Imaging

Mounting

A length of the artificial spider silk thread was loosely spanned (without tension) over a portion of bent wire and secured using glue at each end. An unused end segment of the wire was bent to run roughly parallel with the artificial spider silk and serve as a shaft to load into the tomography accessory sample holder. The silk fiber was oriented such that its length ran parallel with the axis of rotation of the tomography accessory motor, i.e. horizontally in the field-of-view.

Coating

Quadruple-drawn artificial spider silk fiber was imaged before it was coated with an aqueous 2% w/w polyvinyl alcohol (PVA) solution in order to compare coated and uncoated silk. The PVA coating was partially peeled off of the spider-silk fiber (delaminated) with clean splinter forceps in preparation for further comparative imaging between intact and delaminated regions of the same coated spider silk fiber.

4.2.3 FTIR Imaging

The FTIR microscope described in Section 2.1.1 was employed in the acquisition of the stand-alone 2D spatially resolved FTIR images. The sample underwent tomographic imaging under the FTIR microscope as per the Chapter 2 methods. The tomography accessory prototype Mark I, described in Section 2.1.2, was used to hold, position and rotate the sample for 3D spatially resolved FTIR imaging.

Polarization Contrast Imaging

A removable and rotatable infrared polarizing accessory (wire grid KrS-5, Agilent Technologies) was installed on the FTIR microscope for the acquisition of polarization contrast

images. IR light was polarized 90° to the length of the horizontally running silk fiber while a tomographic data set was acquired.[2] The position, initial viewing angle and alignment of the sample were constant for both the unpolarized and 90° polarized FTIR microtomographic imaging. The polarized imaging was completed within 48 hours of the first unpolarized imaging.

Table 4.1: Quadruple-drawn artificial spider silk peak parameters.

Band	**Peak Centre** (cm^{-1})	**Left**		**Right**	
		Baseline, LB (cm^{-1})	**Edge,** LE (cm^{-1})	**Baseline,** RB (cm^{-1})	**Edge,** RE (cm^{-1})
Amide I	1650	1600	1600	1700	1700
Amide II	1550	1500	1500	1590	1590
C–OH (PVA) †	1088	991	991	1160	1160

† PVA parameters are those used for the phantom in Section 3.2 and are identical to the values listed in Table 3.1.

[2]Polarization filter setting 0° blocks light polarized at 0° (horizontal, parallel to the X-axis) and transmits light polarized to 90° (vertical, parallel to the Y-axis)

4.3 Results

4.3.1 Unpolarized Imaging

When examined under visible light, some samples of artificial spider silk were found to have a central indentation running along the long-axis of the fiber (Figure 4.1A). The central indentation was not well resolved with 2D FTIR microspectroscopic imaging of the samples (Figure 4.1B) though the sample was oriented for optimal contrast (Appendix Section 9.4). The FTIR spectra of the silk had sloping baselines consistent with RMieS (Figure 4.1C).

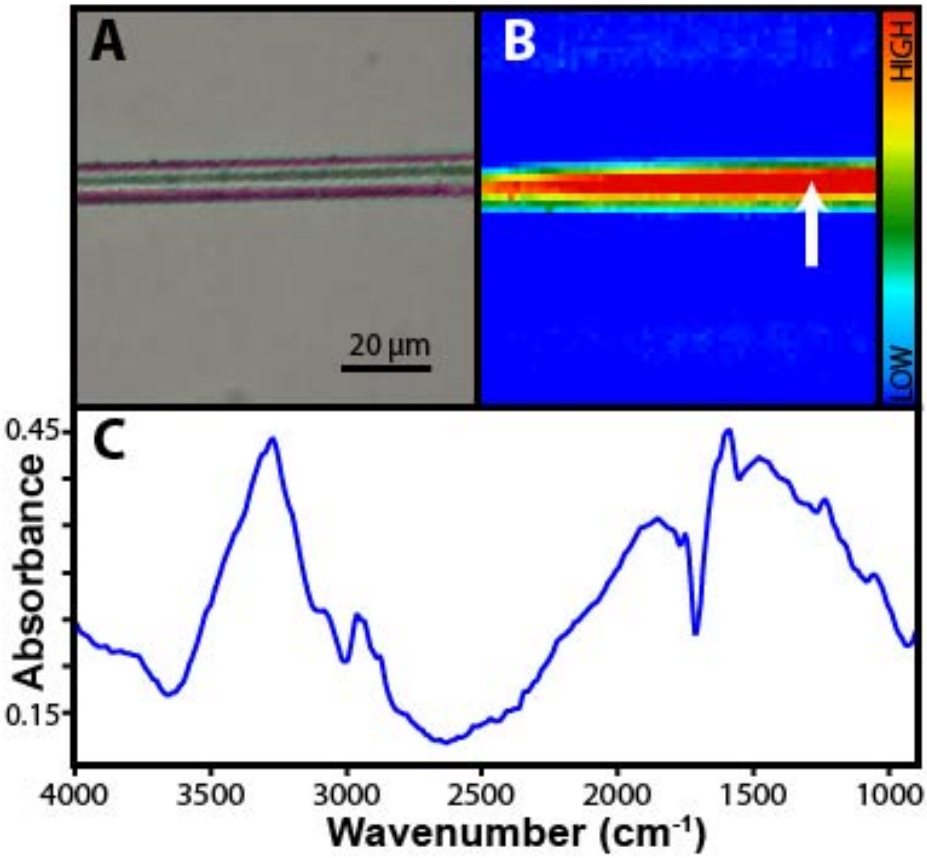

Figure 4.1: Spatially 2D FTIR imaging of quadruple-drawn artificial spider silk fiber. **(A)** Visible image of fiber. **(B)** False-color 2D FTIR image (64 × 64 pixels) processed for Amide I. White arrow indicates the location for **(C)** a typical pixel spectrum from the fiber.

The bandshapes of the absorbance spectrum resembles those of the reflectance spectrum. For example, in the Amide region the spectra appear as a second derivative of the expected absorbances at Amide I and II which classically have maxima at ∼1650 and 1750 cm^{-1} (Figure 4.2).

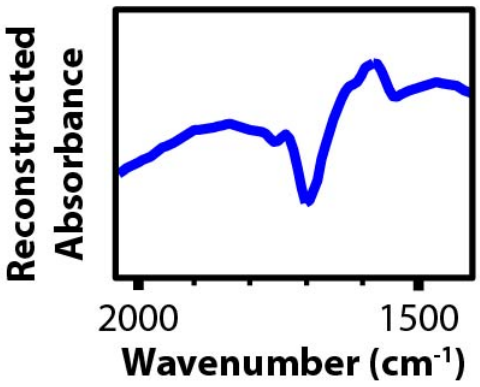

Figure 4.2: Expanded view of the Amide I and II spectral region from Figure 4.1.

PVA applied to micro-samples of the fiber (Figure 4.3A) formed a coating over the strand surface (Figure 4.3B). The coating increased the diameter of the strand by 5–15 μm and obscured the appearance of the central indentation under visible light.

Partial delamination of the PVA coating generated adjacent lengths of silk thread, with and without coating, that could be compared easily (Figure 4.4AB). The spectra of silk that had never before been coated (Figure 4.1C) and delaminated silk (coating removed, Figure 4.4C) both had similar bandshapes and sloping baselines.

The PVA-coated silk (Figure 4.4D) had a markedly improved spectral baseline. Tomographic data from the silk sample shown in Figure 4.4 was acquired. The resulting reconstructed and processed images showed the central indentation to be part of a double stranded sub-structure within the silk fiber; two distinct strands were touching but separated by a small amount of PVA signature (Figure 4.5). The two strands appear in Figure 4.5 as two cylindrical objects that are obliquely adjacent to one another.

Imaging of another sample of the quadruple-drawn artificial spider silk coated with

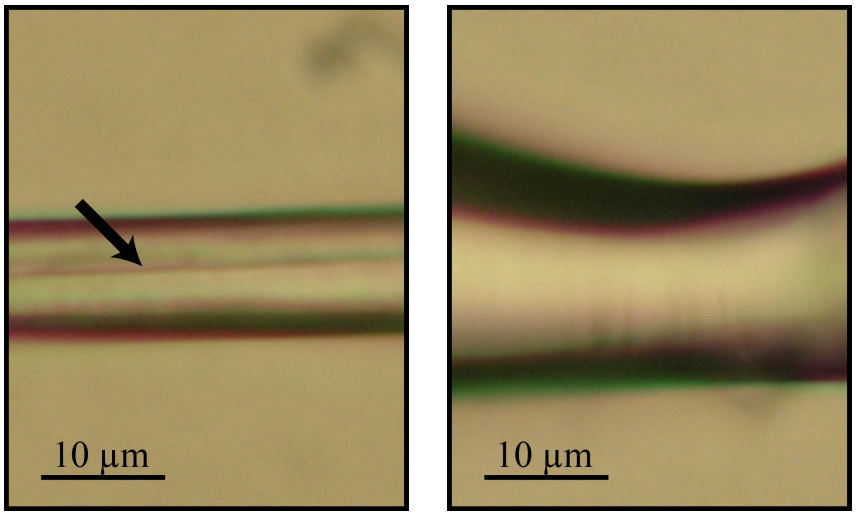

(A) Uncoated. **(B) Coated**

Figure 4.3: Visible light images of artificial spider silk fiber **(A)** before and **(B)** after being coated with polyvinyl alcohol (PVA). The **black** arrow points to the central groove running the length of the fibre.

PVA revealed a grooved structure in 3D spatially resolved FTIR images (Figure 4.6A). Spectral signatures (Figure 4.6B) with the 1651 cm^{-1}, 1527 cm^{-1}, and 1088 cm^{-1} peaks were identifiable in voxels. Specifically, the 1651 cm^{-1} and 1527 cm^{-1} absorbances were found in voxel spectra at the core of the image, co-localized with artificial spider silk as two merging cylindrical substructures, i.e. a grooved strand. Despite the PVA solution surface-tension during coating, no PVA has been drawn into the indentation, and no PVA spectral signature is found between the two cylindrical halves of the fiber structure.

The voxel spectra reconstructed from the silk within the coating had typical absorbance spectrum bandshapes and Amide I and II absorbance maxima with second derivatives compatible with the uncoated silk (Figure 4.7).

The 1088 cm^{-1} peak was co-localized with the coating and was roughly tubular in shape. A central void was viewable after digitally rotating the image (Figure 4.8). The 1088 cm^{-1} void region corresponded to voxels displaying the silk spectroscopic signature, i.e. spectra that include an Amide II absorbance. The $\sim$10 µm diameter of the void is consistent with the diameter of the uncoated silk.

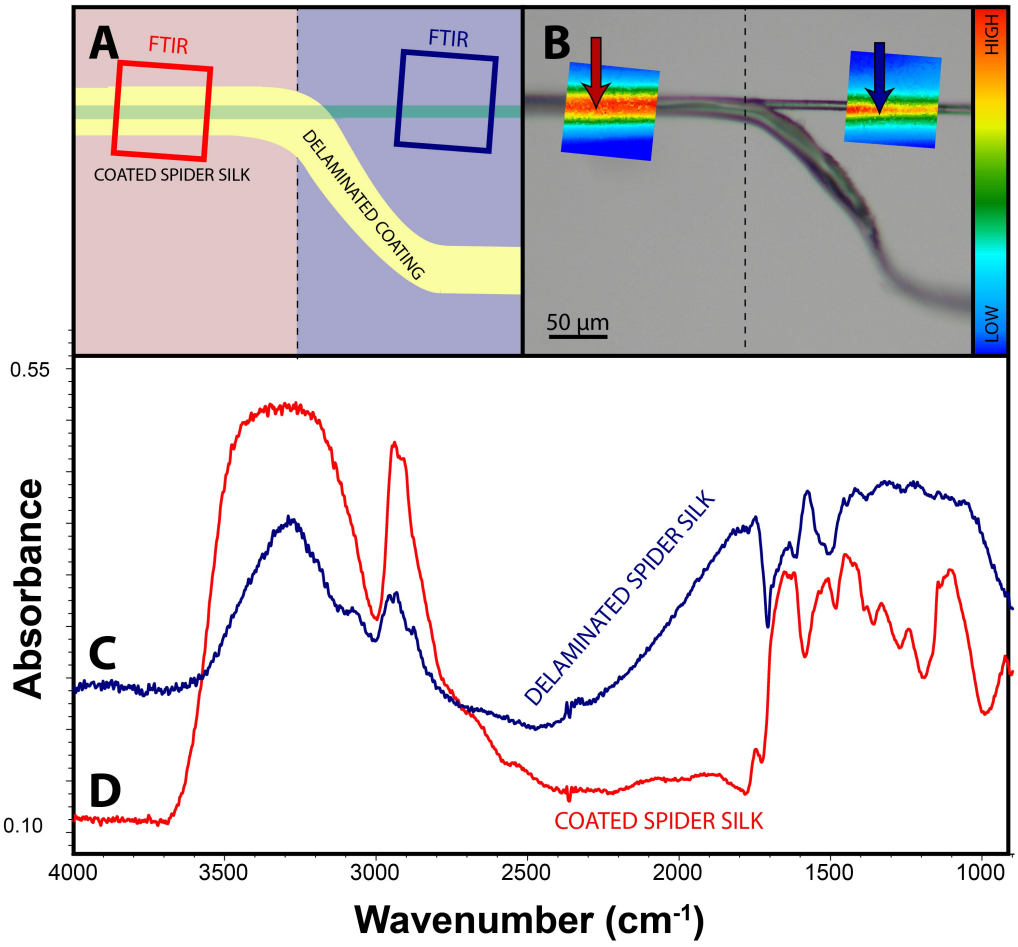

Figure 4.4: Imaging resolved spatially to 2D of quadruple-drawn artificial spider silk from Figure 4.1 coated with PVA and then delaminated on the rightmost part. **(A)** Schematic representation and **(B)** visible light image. Overlaid false-coloured FTIR images processed for intensity at 1650 cm^{-1}. **Red** and **blue** arrows indicate position of pixels used for C and D, respectively. Typical pixel spectra of **(C)** spider silk with PVA-coating intact and **(D)** delaminated spider silk.

4.3.2 Polarized FTIR Microtomography

Polarized FTIR microtomographic imaging of the PVA-coated artificial spider silk showed a co-localization of 1088 cm^{-1} absorbance with the coating and a co-localization of the spider silk with pixels with 1651 cm^{-1} absorbance as before; however, the 1527 cm^{-1} band was reduced in voxels localized to microscopic regions within the silk (Figure 4.9, 4.10).

The spectrum shown in Figure 4.9 is typical of other voxels in the region, and is not an

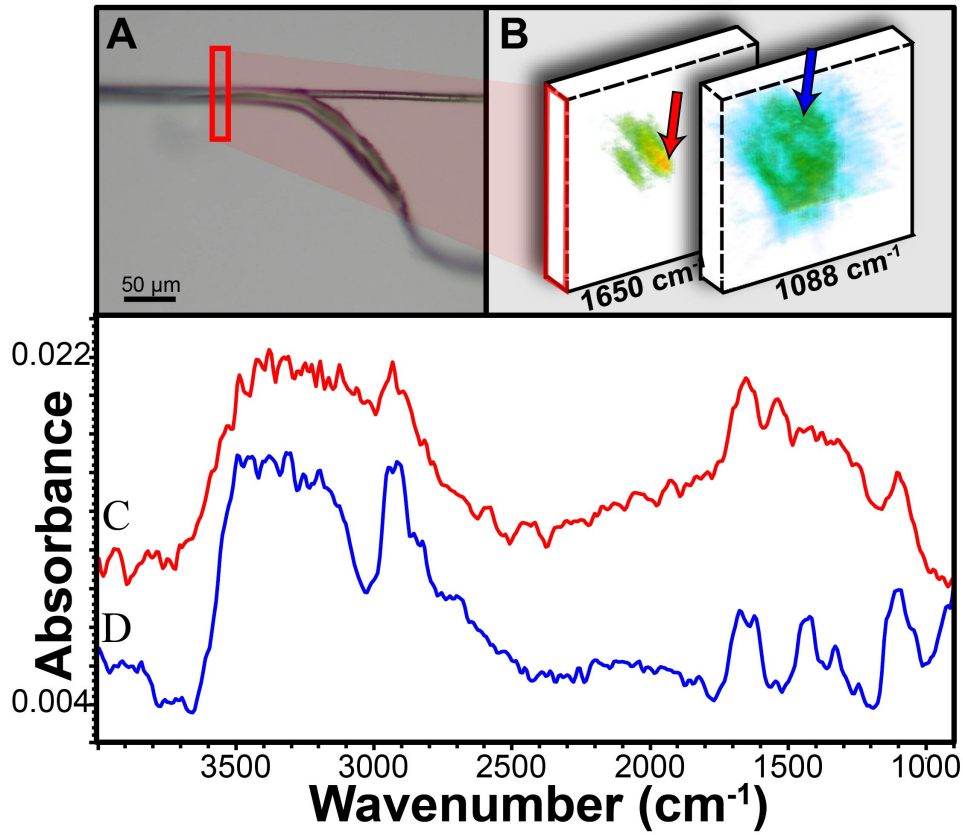

Figure 4.5: 3D imaging of PVA coated spider silk micro-sample from Figure 4.4. **(A)** Visible image with overlaid red box where FTIR tomographic data set (73 views, $\delta\theta = 5.4°$, 64 scans per view, 16 cm^{-1} spectral data spacing) was acquired. **(B)** False-coloured 3D FTIR images reconstructed using filtered back-projection (iRadon, Ram-Lak) and processed for intensity at 1650 cm^{-1} and 1088 $cm.^{-1}$. Image was cropped to 10 $\times$ 50 $\times$ 50 voxels with 1.1 $\times$ 1.1 $\times$ 1.1 μm^3 per voxel. Typical voxel spectra of **(C)** the spider silk within the coating and **(D)** the PVA coating. **Red** and **blue** arrows indicate position of voxels used for C and D, respectively, overlaid on B.

anomaly restricted to a single voxel. One can see from a line of adjacent voxels that the centre-most voxels have similar well-behaved baselines and ratios of Amide I and Amide II (Figure 4.11, blue arrow). Spectra from voxels corresponding to the air-coating interface have elevated and/or rolling baselines, and low contrast between wavenumbers (Figure 4.11, orange arrows).

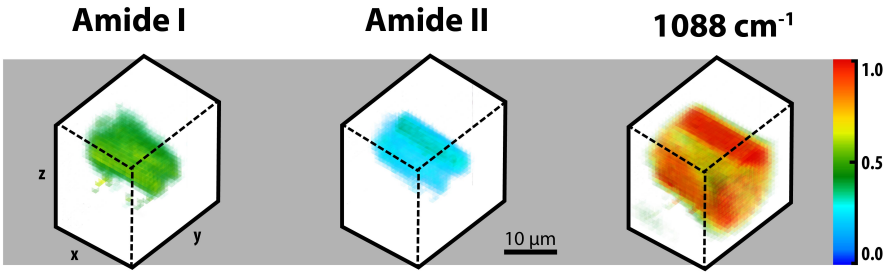

(A) Voxelated Image

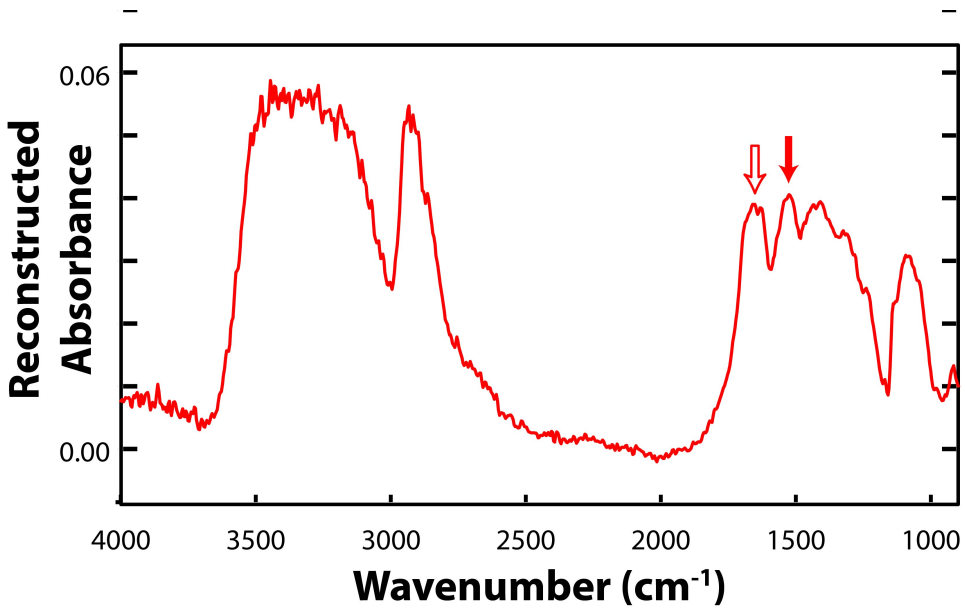

(B) Voxel Spectrum

Figure 4.6: Unpolarized FTIR microtomographic imaging of PVA-coated artificial spider silk. **(A)** FTIR tomographic data set (single tile, 64 $\times$ 64 pixels per view, 35 views, $\Delta\theta = 5.4°$, 1.1 $\times$ 1.1 μm^2 pixels) reconstructed using filtered back-projection. Voxel spectra were false-colour processed for the baseline-corrected area under peaks at 1651 cm^{-1} (Amide I), 1527 cm^{-1} (Amide II), and 1088 cm^{-1} (PVA coating). Image was cropped to 20 x 25 x 25 voxels for clarity. **(B)** A representative voxel spectrum. The hollow and solid **red** arrows indicate Amide I and II, respectively.

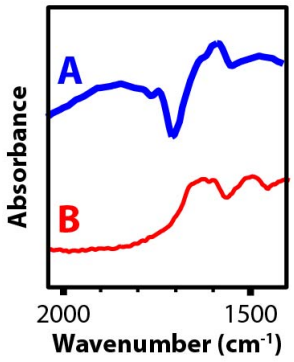

Figure 4.7: Comparison of the expanded view of the Amide I and II spectral region from **(A)** the pixel spectrum from the uncoated silk in Figure 4.1C and **(B)** the reconstructed spectrum associated with a silk-containing voxel from Figure 4.6B.

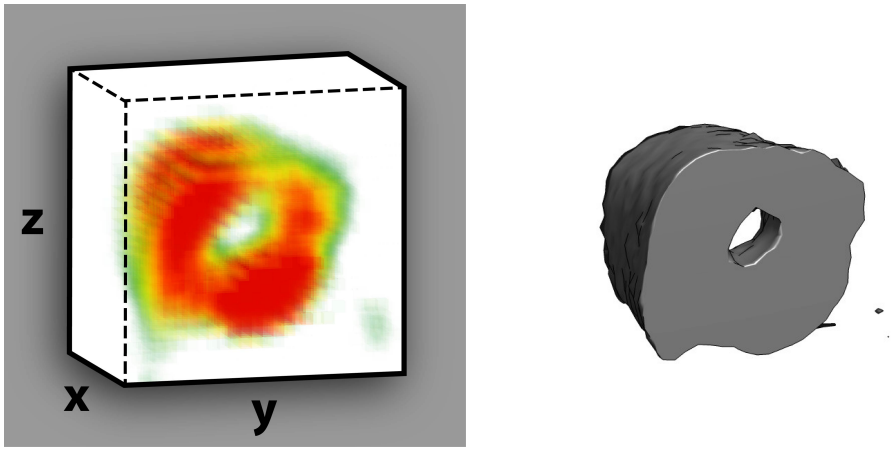

(A) Voxels **(B) Isosurface**

Figure 4.8: **(A)** The voxelated false-colour 1088 cm^{-1} image from Figure 4.6A digitally rotated (azimuth: 165°; elevation: 10°) for better display of a central void area inside of the tubular shape and **(B)** rendered as an isosurface in USCF Chimera software. Image cropped for clarity to 20 x 25 x 25 voxels with 1.1 $\times$ 1.1 $\times$ 1.1 μm^3 per voxel. Scalebar as per Figure 4.6.

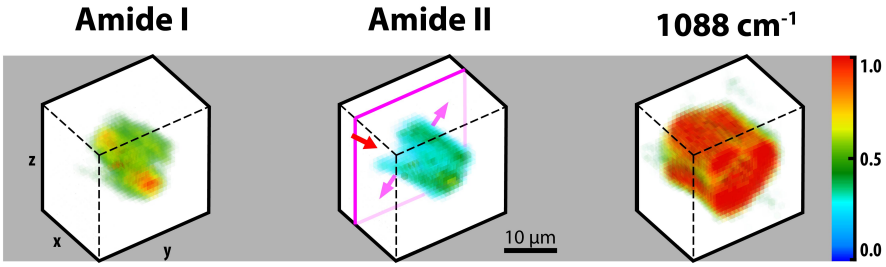

(A) Voxelated Image

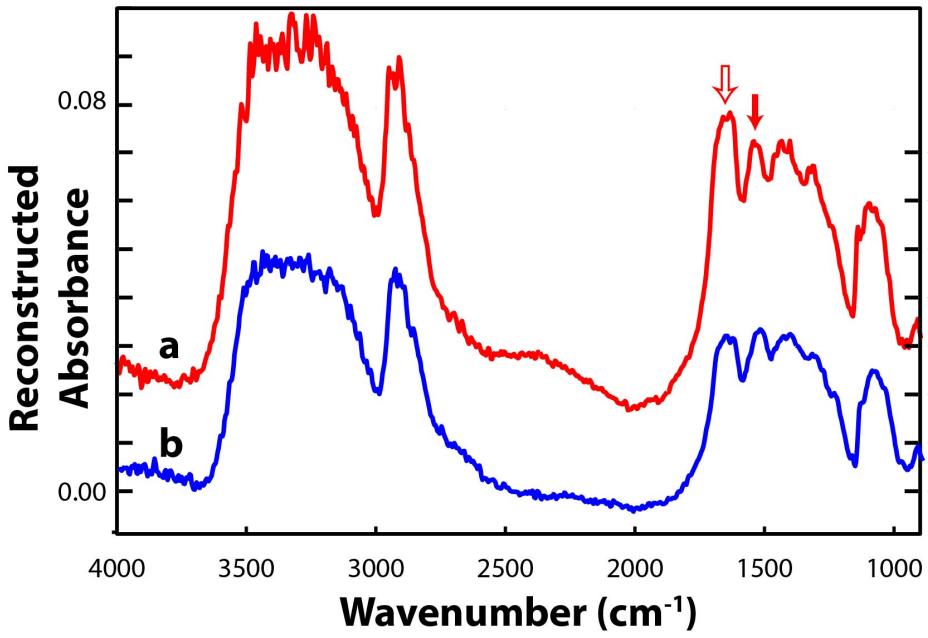

(B) Voxel Spectrum

Figure 4.9: Polarized FTIR microtomographic imaging of PVA coated artificial spider silk. A polarization filter was oriented at 0° so that light polarized to 0° to the X axis was not transmitted. **(A)** FTIR tomographic data set (single tile, 64 × 64 pixels per view, 35 views, $\Delta\theta = 5.4°$, $1.1 \times 1.1\,\mu m^2$ per pixel) was reconstructed using filtered back-projection. The voxel spectra were false-colour processed for baseline-corrected area under the peaks at 1651 cm^{-1} (Amide I, hollow blue arrow), 1527 cm^{-1} (Amide II, solid blue arrow), and 1088 cm^{-1} (PVA coating). Image cropped (20 × 25 × 25 voxels, 1.1 × 1.1 × 1.1 μm^3 per voxel) for clarity. Pink arrows delineate voxels along the diagonal, extracted for stacked display in Figure 4.11. Red arrow on **A** points to location of a representative voxel. **(B)** Spectra from **(a)** the representative voxel on the polarized image with decreased Amide II absorbance and **(b)** the voxel spectrum from the unpolarized image in Figure 4.6, shown for comparison.

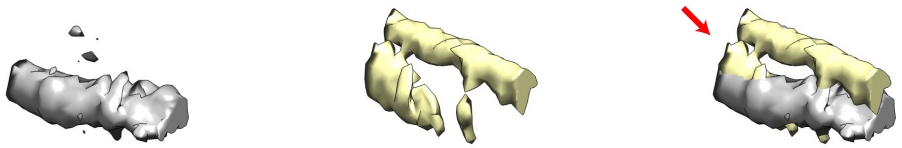

(A) Amide I **(B) Amide II** **(C) Combined**

Figure 4.10: Polarized 3D FTIR images of quadruple-drawn spider silk from Figure 4.9 rotated and rendered as isosurfaces.

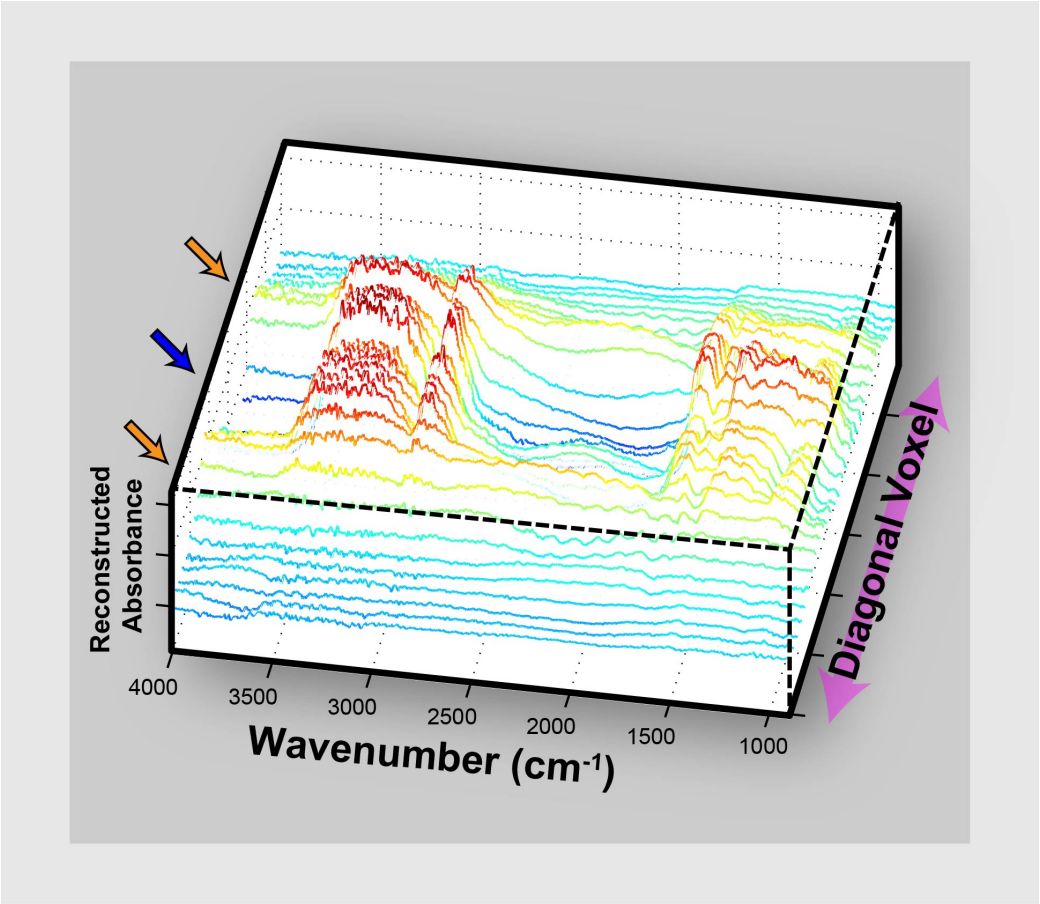

Figure 4.11: Stacked display of spectra extracted from a diagonal line of voxels in Figure Figure 4.9A. **Blue** arrow indicates a voxel spectrum extracted from the centre of the strand. The **orange** arrows indicate voxel spectra spatially located where the edge of the coating on the strand touches the atmosphere (the air-PVA interface).

4.3.3 Inspection of a Physical Cross-Section

Cutting the spider silk with a clean sharp razor blade revealed a single cross-section for inspection under visible light (Figure 4.12).

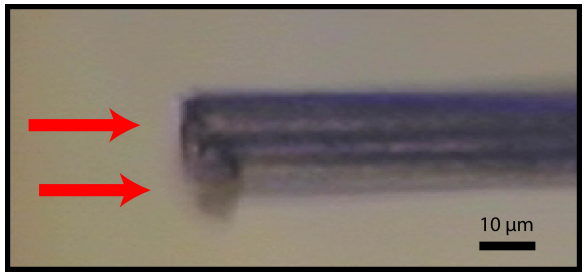

(A) Visible

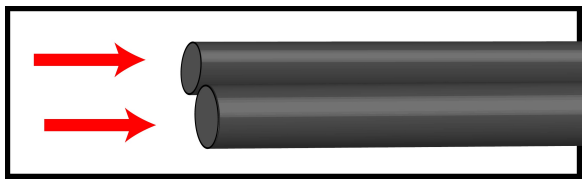

(B) Representation

Figure 4.12: **(A)** Visible light image and **(B)** diagrammatic representation of the cut end of a strand of artificial spider silk. Arrows point to sub-strands within the silk.

4.4 Discussion

4.4.1 Unpolarized Visible and FTIR Imaging

Given that the diameter of the strand of artificial spider silk (diameter 10 µm) is on the same order of magnitude in size as the wavelength of mid-infrared light (1.3 - 3.0 µm), it is unsurprising that scattering is present in FTIR images of the fiber (Figure 4.1). The grooved or double stranded substructure of the silk is not resolved.

A central indentation along the long-axis of the fiber is evident in visible light images of the surface of the artificial spider silk sample imaged here (Figure 4.3), but published SEM images of freeze fractured silk end profile make it clear that both grooved and double strands are possible (Weatherbee-Martin et al., 2016).

A PVA coating reduced silk scattering, as evidenced by a flatter spectral baseline. The absorbance bands of PVA were not separated from those of the silk in 2D (Figure 4.4D). Even when scatter is reduced with a coating, the substructure may not register in 2D images when one sub-strand eclipses the other from view (Suppl. Info. 9.4) as in the case of Figure 4.4. A complete reversal of the coating effect can be seen when the silk is delaminated. The similarity between the spectra of the original silk and the delaminated silk indicates that the PVA coating did not penetrate or chemically alter the silk.

The 3D imaging reveals the artificial spider silk double stranded substructure with the spectra of the silk resolved to a voxel with a scatter-free baseline and separated from the PVA coating signature. (Figure 4.6, suppl. info. 4.5).

In the realm of materials science, it is known that tension relates to longitudinal splitting. Under transverse forces, a drawn tape, i.e. a long and flat material, will undergo fibrillation (Deopura, 1999). The artificial spider silk imaged here experienced four rounds of manual post spin stretching. Even though it is extruded from a single aperture from which one might expect a single fiber, the fiber may undergo forces that encourage it to begin to split (form grooves) and fully split (form double strands).

The 3D imaging technique and coating enabled visualization of the split morphology, when 2D spatially resolved imaging did not. The nondestructive nature of the coating is supported by the spectral peaks and the locations of the voxel spectra containing the coating signatures. The tubular shape formed by displaying the distributions of spectra rich with coating signature (1088 cm^{-1}, Figure 4.8) indicates that coating voxels and silk voxels have mutually exclusive positions in the image, and that the coating did not penetrate the silk.

The tubular shape is hollow, but the walls of the tube had a solid-looking appearance to it. [3] Scattered light off the edges of the imaging subject are not the most predominant feature of the image in Figure 4.8.

[3]This is not found in reconstructions lacking baseline-corrections, which had gossamer (not solid-looking) walls. An example of the gossamer hollow appearance is shown later in Figure 6.6B.

4.4.2 Polarized FTIR Microtomography

The Amide I and II protein absorption bands result from different vibrational modes, each associated with different changes to the molecular dipole. Thus, the Amide I and II bands may or may not have the same relative intensities. (Wiens et al., 2016). The Amide I band stems from molecular vibration involving the carbonyl bonds of amide functional groups. The dipole of the carbonyl is perpendicular to the length of the protein chain and is excited by light polarized at 90° (0° filter setting) to the backbone. The Amide II band stems from backbone modes and is excited by light polarized at 0° (90° filter setting) as represented in Figure 4.13. Additionally, the intensities of the Amide I and II bands change with their orientation relative to the polarization of the incident IR light.

In previous FTIR imaging of collagen by Wiens et al. (2016), tendon was oriented such that fibres were running left to right, horizontally, like the silk here. It was observed that imaging with a polarization filter accessory oriented at 0° (to the horizontal) diminished the Amide II band of absorbance.

During the polarized FTIR tomographic imaging of silk, the polarization filter blocked infrared light polarized to 0° and prevented the vibrational modes of 0° oriented protein backbones from being excited, thus diminishing the Amide II absorbance band. The sub-volumes within the silk fiber that experienced the most reduction in the Amide II band are relatively rich with horizontally-running protein backbone alignment (Figure 4.9).

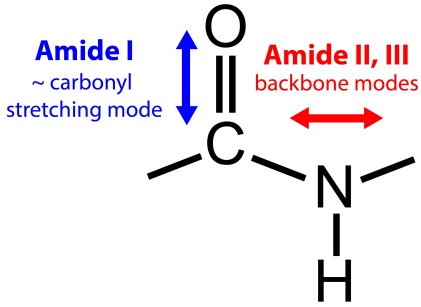

Figure 4.13: Amide functional group.

4.5 Conclusions

Scattering during imaging is a general issue for *all* fibers whose diameters are on the same order of magnitude as the wavelength of infrared light. Light scattered from the surface of a tested micro-fibrous imaging subject, $\sim$10 μm diameter artificial spider silk, obscured details of the silk in 2D FTIR images.

FTIR microtomography played an essential role in an empirical solution to this scattering. The embedding of the silk fiber in a refractive-index matched transparent matrix is viable as a method for reducing scatter and obtaining better quality 3D FTIR images. Additional fine details of these silk specimens, e.g. double-stranded morphological substructure, were captured with FTIR microtomography. The application of a coating was non-destructive and reversible.

The PVA coating did not permeate the silk, but allowed meaningful FTIR polarization contrast images to be acquired from the intact samples. Polarization contrast imaging in 3D shows promise as a method with which to identify highly ordered sub-volumes or fibrillation within the silk. The diminishing intensity of the Amide II band of reconstructed silk spectra in response to 90° polarized IR light indicates the presence of microscopic subvolumes with higher molecular orientation – specifically, alignment parallel to the long axis of the fiber. The identification and quantification of aligned regions is particularly important to stretching applied to silk by manufacturers, who hope to increase such alignment, and as a consequence, silk strength.

Chapter 5. Imaging Arctic Sea Ice Diatoms

5.1 Background

5.1.1 Diatoms

Diatoms are aquatic single-celled microorganisms that can be found in all natural freshwater and marine habitats, including those in the Arctic. Diatom cells can create an intricate biogenic silica encapsulation to protect their organic cell contents from the surrounding environment. These 'frustules' have multiple functions. Nutrients from the surrounding environment can flow through the micro-patterned pores in the frustule into the cell. As well, the optical properties and 3D morphology of the silica frustule can increase the efficiency of light capture for these photosythetic heterotrophs, aiding the fixation of carbon for assimilation into anabolic biochemical pathways. (Round et al., 1990).

Diatoms are the main source of primary production in Arctic sea ice and their consumption by various benthic macrofauna supports the health of fisheries for human consumption. The consumption of diatoms can be traced through the ecosystem and forms the foundation of food webs (Round et al., 1990).

Human consumption of fossil fuels has raised the issue of global climate change. The Arctic environment is particularly sensitive to warming, due to the melt of layers of snow that reflect back incoming sunlight. Diatoms are known to be very responsive to the Arctic climate (Leu et al., 2011). The influence of environmental parameters, such as the depth of snow cover and light limitation, can be observed in the organic content of diatoms (Mock and Gradinger, 2000; Pogorzelec et al., 2017)

Methods exist to analyze the organic content of diatoms in a community of mixed species as bulk samples, such as particulate organic carbon and nitrogen analysis on a CHN elemental analyzer, thin-layer chromatography with flame ionization detection of

lipid classes, etc. (Cota and Smith, 1991). The dietary value of individual species cannot be determined by bulk analysis.

The proliferation of different diatom species and types of organic content are specific to the time of year and body of water. One example of this comes in the form of forensic investigations into drownings in natural bodies of water, which use the presence of diatoms as the gold standard verification test. Only trace amounts of forensic material are available for analysis (Peabody, 1977); however, even microscopic amounts of material can be measured with FTIR microtomography, which is well suited for analysis of one-of-a-kind samples as it is non-destructive in nature (Martin et al., 2013).

FTIR imaging spatially resolved to 2D was used in a study by Pogorzelec et al. (2017) to assess the organic content of diatoms under high and low snow depth, as they adapted to changing light and nutrient conditions of the 2014 Arctic vernal bloom. The samples are specific to the environmental conditions at that time and place, and thus were unique. Published results, for example, those by Pogorzelec et al. (2017), show taxa-specific biomolecular responses of Arctic sea ice diatoms.

FTIR imaging spatially resolved to 3D has been conducted on an algal cell (Martin et al., 2013), but not on a diatom as a whole and not on diatoms from this unique point in time. As such, diatoms present as novel imaging subjects on which to demonstrate the modified methods developed in this thesis.

As summarized by Pogorzelec et al. (2017) and Findlay et al. (2017), there are multiple motivations for the use of FTIR tomographic imaging in the analysis of diatoms. Two that were highlighted by these authors were 1) the unique ability to perform species-specific analysis of mixed-species samples via imaging and 2) simultaneous measurement of concentrations of biocomponents (proteins, lipids, carbohydrates, and silica).

In this thesis, two FTIR microtomography experiments are shown. In the first (Experiment A), individual diatoms from the sample set consisting of a single species, *Nitzchia frigida*, were statistically analyzed to determine the effect of a changing environmental con-

dition: snow depth. In the second (Experiment B), 3D mosaic imaging of a larger species of diatom, *Entomoneis* spp., demonstrated trans-axial resolution of organelles.

5.2 Methods

5.2.1 Field Collection

A series of diatom samples were collected from a landfast ice site in Dease Strait, NU, Canada (69° 1.11'N; 105° 21. 29'W) under the umbrella of the ICE-CAMPS project (Ice Covered Ecosystem-CAMbridge Bay Process Study), March-June 2014. Ice algal samples were harvested from areas with high (17 – 19 cm) and low (3 – 7 cm) snow cover depths in sets of ice cores extracted using a 9 cm diameter Mark II Coring System (Kovacs Enterprises). Ice cores were shielded from direct solar radiation while bottom ice scrapes (0.5 cm) of 2 cores were pooled into opaque, high-density polyethylene bottles containing 500 mL of cooled 0.2 μm filtered seawater (FSW) and melted in the dark.

Aliquots of the gently mixed ice melt were filtered onto polycarbonate filters (Sterlitech Corp. USA, 5 μm pore size, 25 mm diameter). The filters were folded in half such that the diatoms lay on the inner surface of the polycarbonate. The folded filters were wrapped thoroughly in aluminum foil. The wrapped filters were immediately stored in sealed plastic bags in a -80°C portable freezer for transportation. The plastic bags were relocated to -80°C storage freezers (CEOS, UofM) and were thawed prior to sample preparation.

5.2.2 Preparation and Imaging

For each filter, a section was immersed in FSW (filtered from Gulf of Maine seawater, National Center for Marine Algae and Microbiota, USA) to release cells. Droplets of the solution with resuspended diatoms were immediately deposited onto glass microscope slides.

Cells viewed under a dissecting microscope were captured on hand-manipulated polyimide Microloops (MiTeGen™, NY, 35 - 50 μm diameter). The cell-laden microloops were loaded on the tomography accessory and imaged via the FTIR microtomography technique (Chapter 2). No PVA coating was used.

FTIR data sets were acquired with the Mark I prototype tomography accessory (Section 2.1.2) within a few days of sample thawing with the Section 2.1 protocols. Images comprising a tomographic data set were acquired with a co-addition of either 8 scans or 64 scans, and between 64 and 100 non-redundant viewing angles.

Experiment A: Imaging of *Nitzschia frigida* from Low and High Depth Snow Cover

Colonies harvested from two snow cover depth conditions (low and high) on a single tested time point early in the Arctic vernal bloom (19th May, 2014) were examined. A single stand-alone 2D FTIR image of a colony was analyzed first, prior to acquisition of full tomographic data sets. One cell from each of the 6 total *Nitzschia frigida* colonies underwent identical 3D spatially resolved FTIR imaging and analysis.

Experiment B: Mosaic Imaging of *Entomoneis* spp.

A single *Entomoneis* spp. cell harvested on April 29, 2014 from under high depth snow cover was examined. A mosaic image was acquired at each viewing angle to form an *Entomoneis* spp. tomographic data set. A tomographic data set of the *Entomoneis* spp. cell (3×3 tiles per view, 64 views, $\Delta\theta = 5.4^{\circ}$) occupied $\sim$6.50 GB of hard-drive space when exported to ENVI format. The same data was reduced in size to $\sim$2 GB upon resaving in Matlab™ '.mat' format. The spectral windows and axial slices not obscured by the polyimide microloop permitted tomographic reconstruction. [1]

[1] An example of the complete spectral and spatial reconstruction of a cell on a polyimide microloop is shown later in Section 6.3.1.

5.2.3 Data Processing

Baseline-corrected peak areas were calculated as per Section 2.4.3 using the parameters in Table 5.1.

Table 5.1: Diatom peak parameters.

Band	Peak Centre (cm^{-1})	Left		Right	
		Baseline, LB (cm^{-1})	**Edge,** LE (cm^{-1})	**Baseline,** RB (cm^{-1})	**Edge,** RE (cm^{-1})
Si-O	1055	1044	1053	1093	1113
Amide I	1650	1488	1610	1685	1806
C=O	1739	1707	1708	1728	1753
C-H region (CH_2 and CH_3 sym. and asym. str.)	†	2841	2841	2970	2970

† Four peak centres in region, see Figure 1.11 for illustration.

The parameters for the Amide I band overlap with a Si-OH bending mode of hydrated silica. Similarly, the CH stretch region, considered a signature fatty-acid region, includes contributions from other sources such as protein hydrocarbons and not exclusively fatty acids. Still, these parameters are sufficient for imaging considering the comparative weakness of these other contributions (Findlay and Gough, 2016).

A threshold value was applied in order to delineate the cells during analysis. A voxel was deemed to lie within a diatom cell when its corresponding spectrum had a value greater than 0.5 for integrated SiO band area. Isosurfaces of the image data defined by this 0.5 SiO integrated band area were compared with visible light images to confirm that this value did not over- or under-represent the volume of the cell. The sum of all such voxels yielded total cell volume. Lipid and protein proxies were calculated for all voxel spectra within the cell

as the sum of the integrated CH_2 and CH_3 symmetric and asymmetric stretching bands and Amide I band areas, respectively.

Analysis of Significance via Permutation Test

A permutation test described in the text by Berry et al. (2014) was used to determined the exact probability that a sampling had a smaller mean than any other grouping of size n = 3 from the set of all measurements.

5.3 Results

Visible light microscopic images of the re-suspended diatoms showed that cells from multiple species of diatoms were diverse in size, and shape and were overlapping (Figure 5.1). Intact individual cells or colonies could be isolated and captured from tangled clumps using a microloop (Figure 5.2).

5.3.1 Exp. A: *Nitzschia frigida* from Low and High Depth Snow Cover

The *Nitzschia frigida* cells were abundant in the mixtures of resuspended diatoms. Cells in the branched colonies collapsed back on themselves when scooped from the FSW, resulting in appearances typical of the colony in Figure 5.3. The four segments of collapsed cells and one end cell project out into open air from the loop.

Though manual manipulation of the microloops was sufficient to capture individual diatom cells from the mixture of species, there was insufficient control to precisely orient the diatoms on the loops. As a result, diatom colonies protruded from the microloops at random angles (Figure 5.4). Once dry, the diatom cells within a colony remained fixed in place at a particular angle and did not change positions relative to each other when the holder was rotated.

FTIR data resolved spatially to 2D were obtained from a non-overlapping cell within

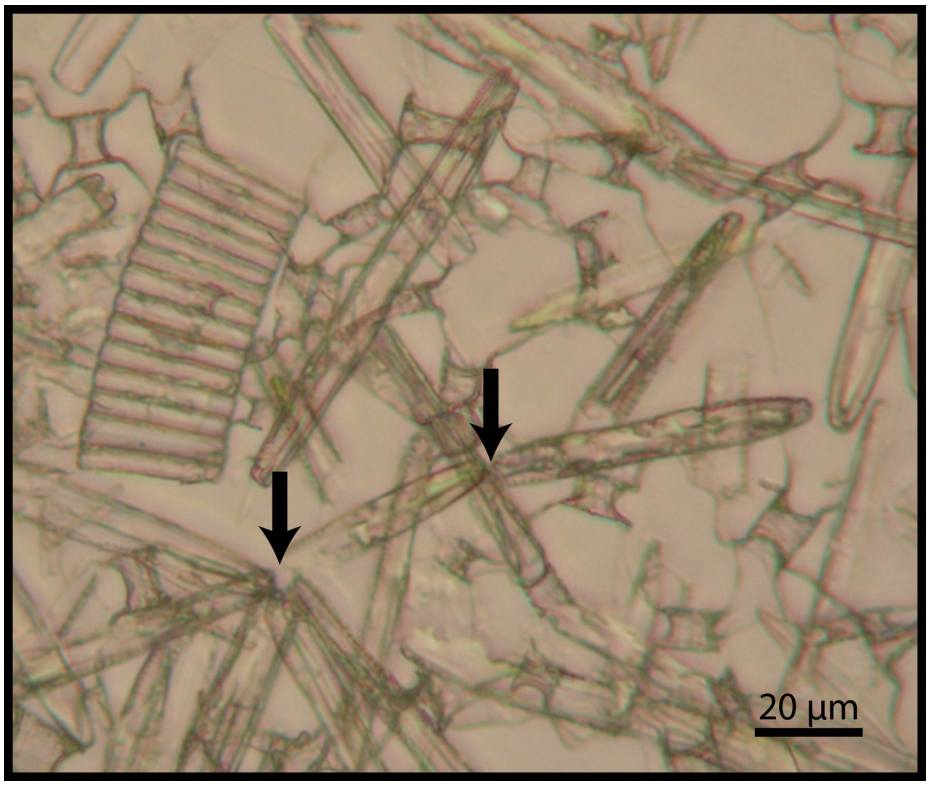

Figure 5.1: Visible light image of re-suspended Arctic sea ice diatoms in FSW. The black arrows point to two branch points of a colony.

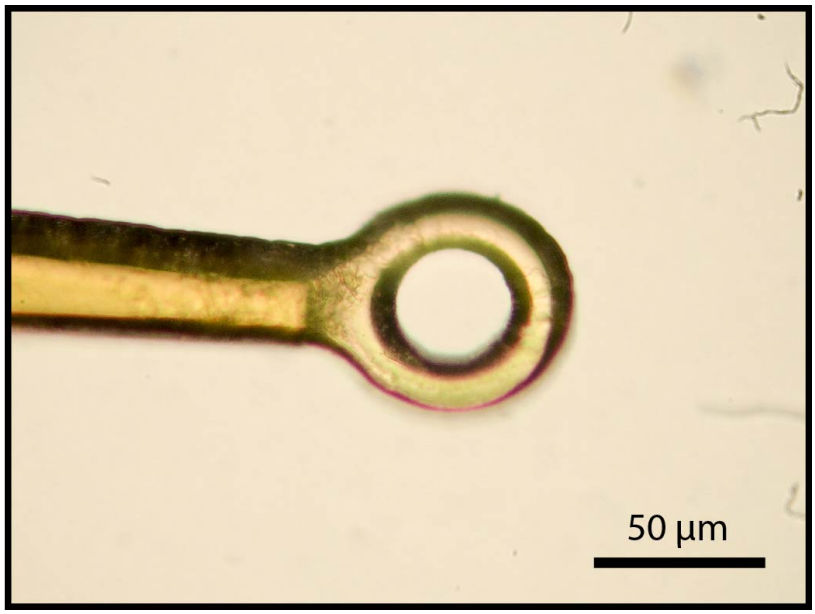

Figure 5.2: Visible light image of a MitiGen™ polyimide microloop. Inner diameter: 35 µm.

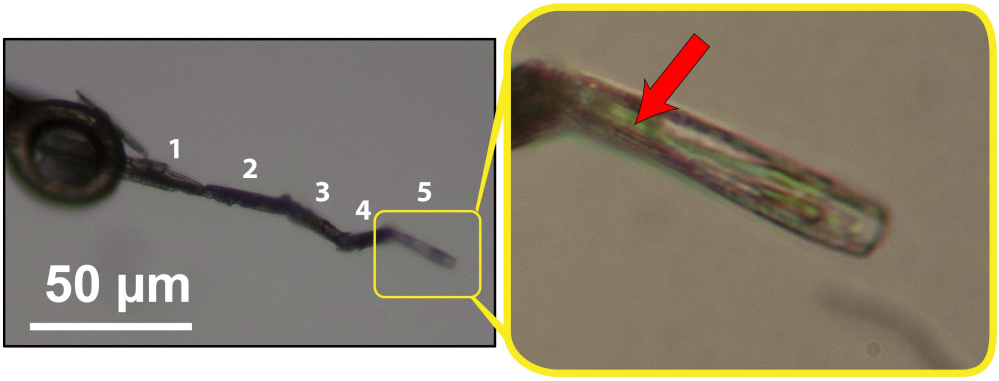

Figure 5.3: Visible light image of a branched *Nitzschia frigida* colony mounted on a polyimide microloop. Cells (overlapping cells, segments 1-4; non-overlapping cell 5) are labeled with white text. Inset (yellow outline) shows close-up view of the endmost cell (No. 5), oriented for FTIR imaging in transmission mode. Red arrow indicates position of the pixel associated with the spectra displayed in Figure 5.5. Adapted from Findlay et al. (2017).

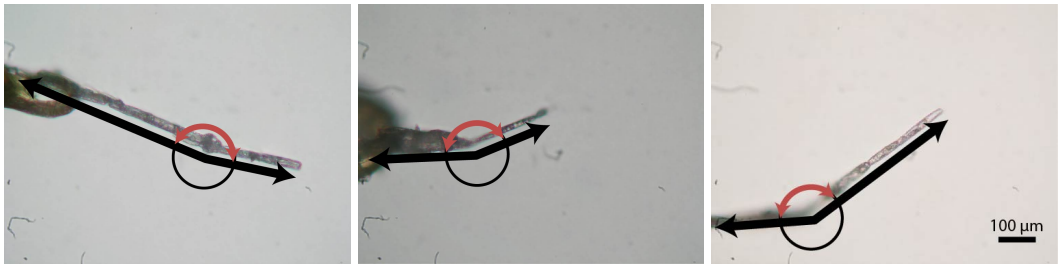

(A) 9° **(B) 21°** **(C) 37°**

Figure 5.4: Visible light images of three diatom colonies (ABC) scooped from solution onto manually manipulated polyimide microloops. The endmost cell(s) (toward the right side of the images) is/are oriented at different angles relative to the next adjacent cell upon drying: **(A)** 9°, **(B)** 21°, and **(C)** 37°.

this colony. The spectra were similar to the spectrum shown in Figure 5.5, with a few variations. False-colour images (Figure 5.6) showed that pixel spectra throughout the cell had elevated SiO absorbance, while pixels from the visibly pigmented regions had the greatest CH and Amide I peak areas.

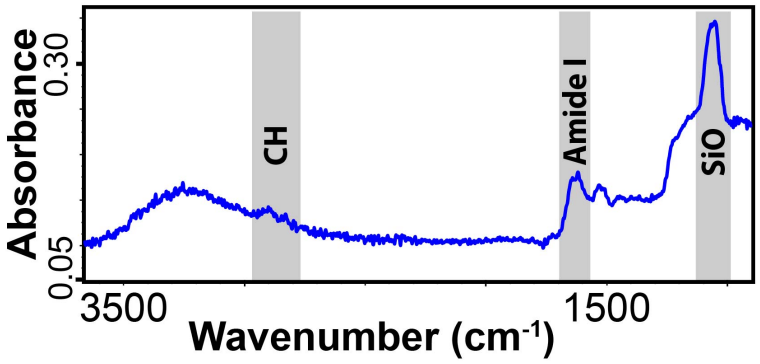

Figure 5.5: FTIR pixel spectrum with typical *Nitzschia frigida* absorbance profile. The location of this pixel spectrum relative to the image from which it was extracted is indicated by the arrow in Figure 5.3. The gray bars highlight bands of interest. Spectra acquired with the co-addition of 16 scans. Adapted from Findlay et al. (2017).

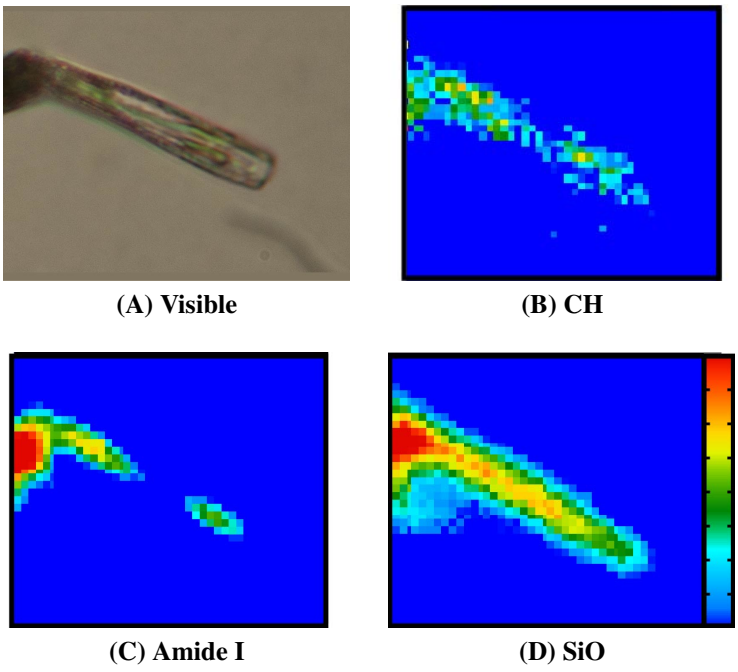

Figure 5.6: False-colour 2D FTIR images of the endmost cell of the *Nitzschia frigida* colony in Figure 5.3 processed for baseline-corrected integrated intensities of CH, Amide I, and SiO bands. Adapted from Findlay et al. (2017). Each pixel is 1.1×1.1 μm^2. Scalebar is as per Figure 5.3.

Each of the 82 single-tile 2D FTIR images comprising a *Nitzschia frigida* cell tomographic data set were acquired with the co-addition of 8 scans. There was a low S/N ratio of $\sim$2 based on the height of the Amide I band and due to the low number of scans (Figure 5.7 pixel spectrum). After the pixel spectra were used as inputs to iradon(), the output voxel spectra had a $\sim$10$\times$ higher S/N ratio (Figure 5.7 voxel spectrum).

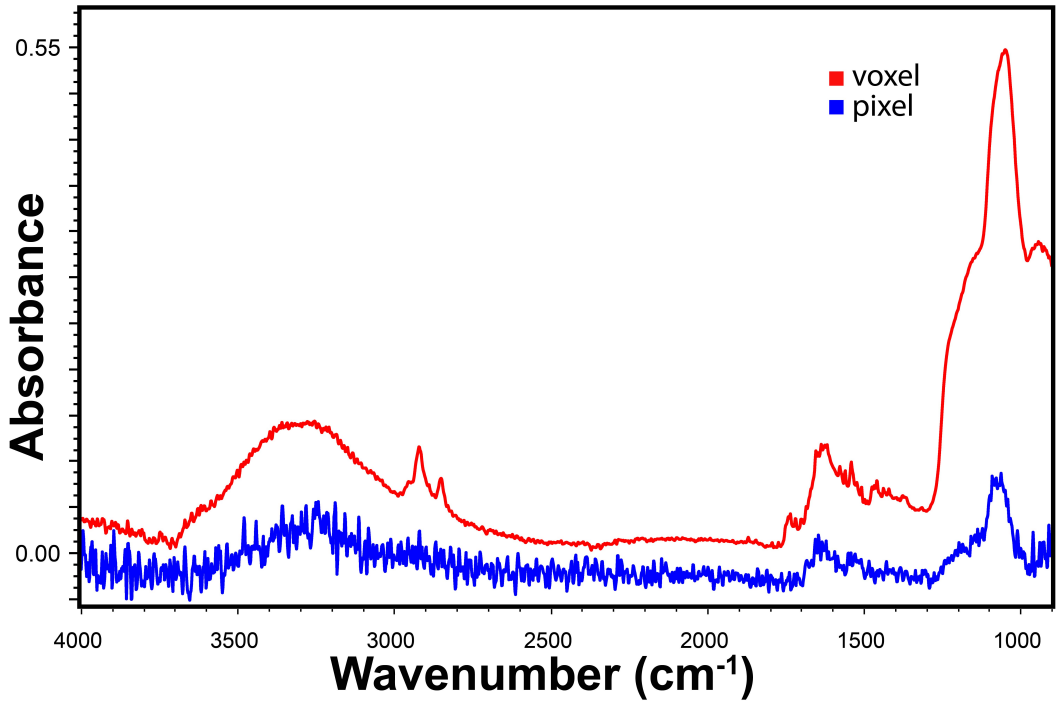

Figure 5.7: Spectral noise reduction in Nitzschia frigida reconstruction. Pixel spectrum (**blue**) from one viewing angle in a tomographic data set (8 scans, 82 views) and the resulting voxel spectrum (**red**) after the data set is input into 'iradon()' (Matlab^{TM}, unfiltered back-projection function). Spectra are on common scale, off-set for clarity.

Exactly as was found from the 2D images, the 3D false-colour images (Figure 5.8) show elevated SiO absorbance throughout the cell, while voxels from the visibly pigmented regions had the greatest CH and Amide I peak areas (Figure 5.8). There were additional cell-to-cell differences in spectra. The infrared voxel spectra at local absorbance intensity maxima of high and low depth cells were not identical in appearance. The levels of CH absorbance were elevated relative to the Amide I band in cells harvested from beneath low snow depth cover (Figure 5.9).

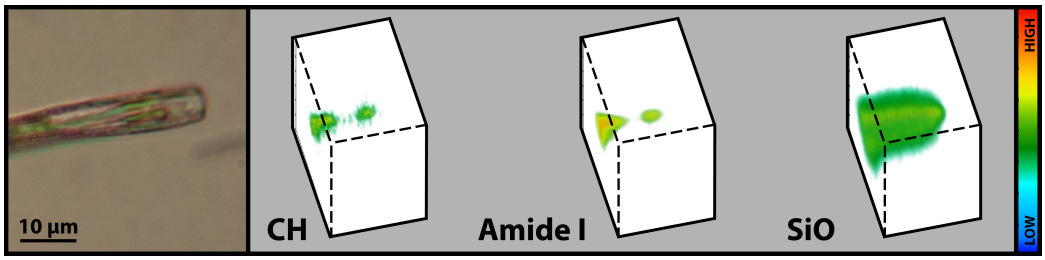

(A) High Snow Depth

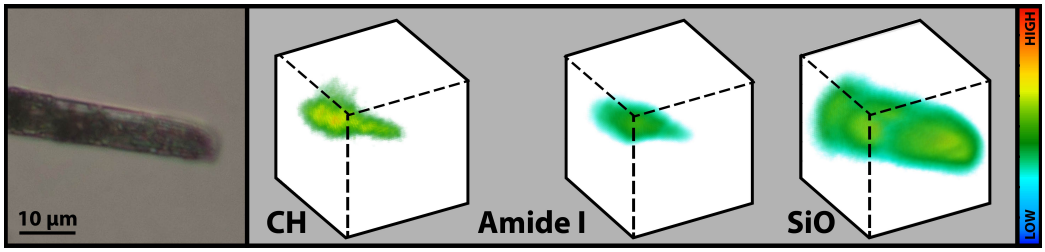

(B) Low Snow Depth

Figure 5.8: Thermal source FTIR tomographic images (each 8 scans per 64 × 64 pixel tile, single tile per view, 82 views, $\Delta\theta = 5.4°$ interval) of cells from *Nitszchia frigida* colonies harvested from Arctic sea ice under **(A)** high or **(B)** low snow cover depths. **(LEFT)** Visible light image and **(RIGHT)** 3D FTIR false-colour images created by integration of CH, Amide I and SiO spectral bands. Adapted from Findlay et al. (2017).

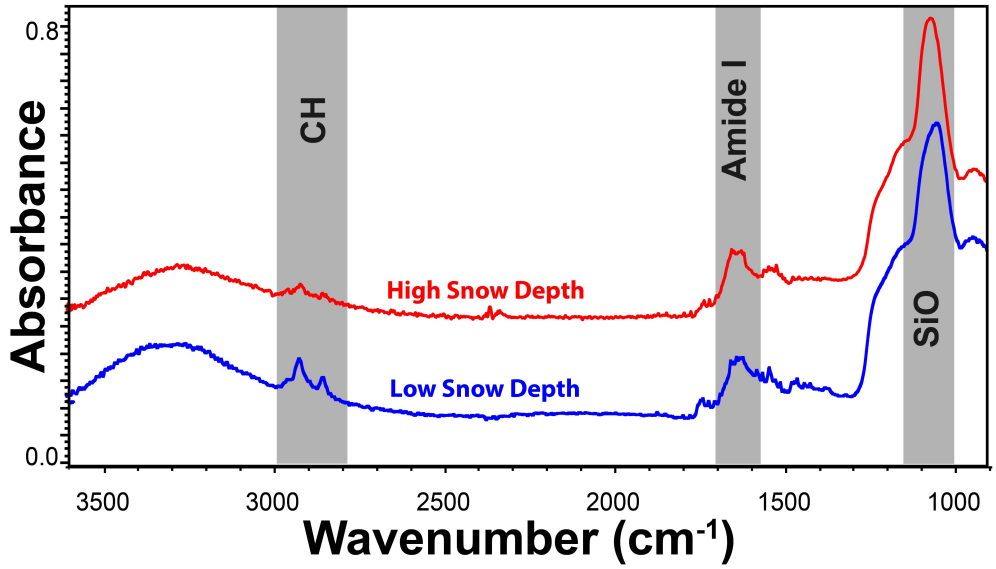

Figure 5.9: Infrared voxel spectrum from location with maximum CH absorbance for each of two *Nitzschia frigida* cells. The **red** and **blue** spectra were acquired from cells harvested in bottom scrapes of Arctic sea ice cores under high or low depths of snow cover, respectively. Common scale, offset for clarity. Adapted from Findlay et al. (2017).

An increase in the ratio of CH to Amide I absorbance was found in a small but statistically significant number of cells (n = 3). Each voxel ($1.1 \times 1.1 \times 1.1$ μm^3) contributed a 0.0013 picolitre volume. The volume of the 3D image deemed to be occupied with diatom was calculated, i.e. the volume of the pixels that exceeded the detection threshold (SiO area > 0.5). Values for the *Nitzschia frigida* cells imaged were tabulated (Table 5.2).

Table 5.2: Diatom values calculated from baseline-corrected integration of 3D thermal source FTIR tomographic images of *Nitzschia frigida* harvested from Arctic sea ice, under low (3–7 cm) and high (17–19 cm) snow cover depths on the 19th May, 2014. Adapted from Findlay et al. (2017).

	Voxels Occupied	Cell Vol. (pL)	Sum of Cell Spectral Peak Areas		Average per Voxel	
			CH	Amide I	CH	Amide I
High Snow Depth						
Cell 1	95175	95	22796	193960	0.24	2.0
Cell 2	172337	172	42767	184730	0.25	1.1
Cell 3	106146	106	42167	187350	0.40	1.8
Mean	124553	125	35910	188680	0.29	1.6
Low Snow Depth						
Cell 4	86283	86	66695	130480	0.77	1.5
Cell 5	102507	103	363440	480790	3.55	4.7
Cell 6	150456	150	208340	406370	1.38	2.7
Mean	113082	113	212825	339213	1.90	2.9

Analysis of Significance via a Permutation Test

Let the alternative hypothesis be that the mean CH per voxel is less for diatoms under high snow depth than for those under low snow depth. The peak area ratio observations for the voxel spectra of the two different snow depths are:

Table 5.3: Ratio of baseline-corrected peak areas (CH ÷ Amide I).

Low Snow Depth	cell 1 (0.12)	cell 2 (0.23)	cell 3 (0.23)
High Snow Depth	cell 4 (0.51)	cell 5 (0.76)	cell 6 (0.51)

The combined samples are 0.12, 0.23, 0.23, 0.51, 0.76 and 0.51.

Table 5.4: Ratio of baseline-corrected peak areas, (CH ÷ Amide I).

High Snow Depth	cell 1 (0.12)	cell 2 (0.23)	cell 3 (0.23)
Low Snow Depth	cell 4 (0.51)	cell 5 (0.76)	cell 6 (0.51)

In Table 5.5, there are 20 (6 choose 3) ways to group the values into two-sample sets. The first data set with asterisk in Table 5.5 is the observed data. The -0.40 difference of means is the lowest possible and therefore the p-value is $1 \div 20 = 0.05$ for this set.

Table 5.5: Permutation distribution for the Ratio Values.

Grouping Number	Grouped Values (cell no.)	Difference Between Means
1*	0.12 , 0.23 , 0.23 (1 2 3)	-0.40
2	0.12 , 0.23 , 0.51 (1 2 4)	-0.21
3	0.12 , 0.23 , 0.76 (1 2 5)	-0.05
4	0.12 , 0.23 , 0.51 (1 2 6)	-0.21
5	0.12 , 0.23 , 0.51 (1 3 4)	-0.22
6	0.12 , 0.23 , 0.76 (1 3 5)	-0.05
7	0.12 , 0.23 , 0.51 (1 3 6)	-0.21
8	0.12 , 0.51 , 0.76 (1 4 5)	0.14
9	0.12 , 0.51 , 0.51 (1 4 6)	-0.02
10	0.12 , 0.76 , 0.51 (1 5 6)	0.14
11	0.23 , 0.23 , 0.51 (2 3 4)	-0.14
12	0.23 , 0.23 , 0.76 (2 3 5)	0.02
13	0.23 , 0.23 , 0.51 (2 3 6)	-0.14
14	0.23 , 0.51 , 0.76 (2 4 5)	0.21
15	0.23 , 0.51 , 0.51 (2 4 6)	0.05
16	0.23 , 0.76 , 0.51 (2 5 6)	0.22
17	0.23 , 0.51 , 0.76 (3 4 5)	0.21
18	0.23 , 0.51 , 0.51 (3 4 6)	0.05
19	0.23 , 0.76 , 0.51 (3 5 6)	0.21
20	0.51 , 0.76 , 0.51 (4 5 6)	0.40

5.3.2 Exp. B: Mosaic FTIR Imaging of *Entomoneis* spp.

The *Entomoneis* cell had an overall globular frustule morphology that narrowed at the waist with double-lobes that twisted relative to one another, typical of the species. The particular cell prepared for imaging was approximately 150 μm long, larger than a single FPA tile. Initially a small piece of debris adhered to the *Entomoneis* spp. cell, but detached upon

mounting (Figure 5.10). In the visible light image shown in Figure 5.10B, half of the cell was partially obscured by the loop, which did not transmit much visible light.

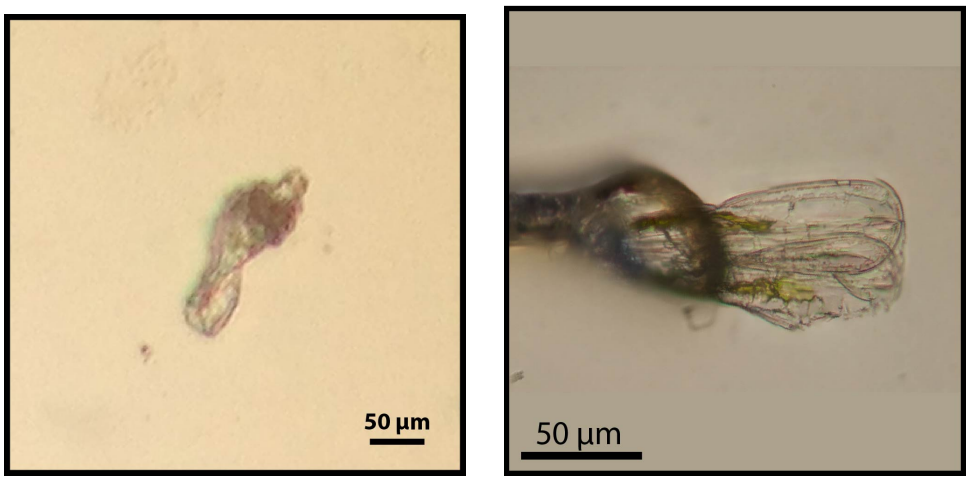

(A) Before **(B)** After

Figure 5.10: Visible light images of an *Entomoneis* spp. cell **(A)** before (when resuspended in FSW) and **(B)** after (when dry, not in solution) being caught on a MiTiGen^{TM} polyimide microloop holder (35 µm inner diameter).

The pixel spectra of the *Entomoneis* spp. cell had contributions from both loop and cell where they overlapped (Figure 5.11A). The part of the cell that was free of the loop had spectra more typical of diatoms (Figure 5.11B). It is clear upon comparison to the spectrum of the polyimide (Figure 5.11C) loop alone that the polyimide signature (including the peak at 1739 cm^{-1}) is overlapping spectral regions where important biological components absorb, e.g CH and Amide II. The Amide I band is relatively free of polyimide absorbance, compared to the Amide II band.

Polyimide has a molecular structure as shown in Figure 5.12 and absorbs strongly in the mid-infrared region.

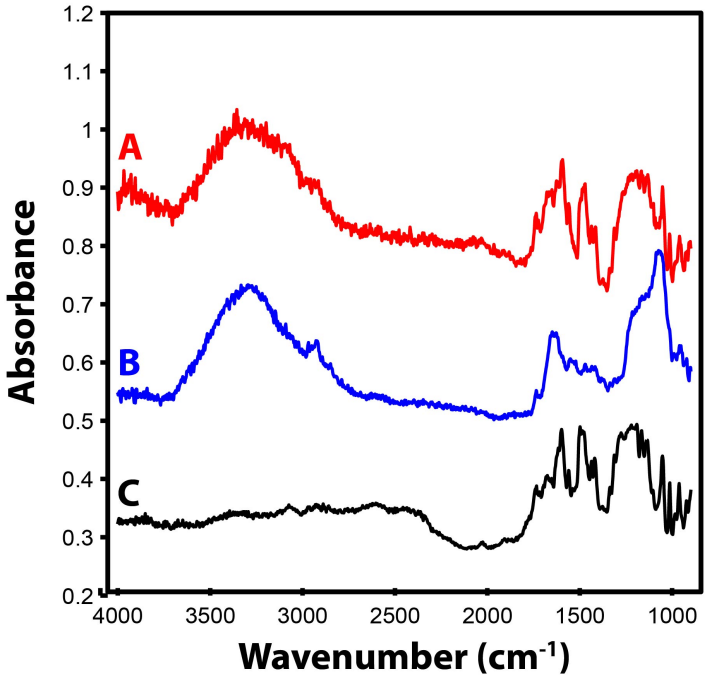

Figure 5.11: FTIR spectra (64 scans co-added) of the *Entomoneis* spp. Pixel spectra were extracted from location with **(A, red)** diatom on loop, **(B, blue)** diatom protruding off the loop and **(C, black)** the polyimide loop alone. Location of the spectra are marked in Figure 5.14 with color corresponding arrows. Image data not shown for spectra of loop alone acquired prior to diatom mounting.

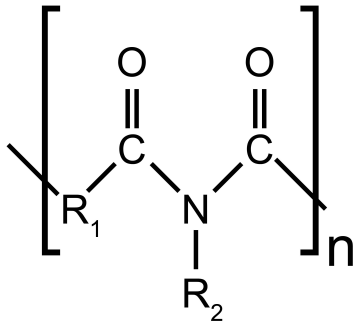

Figure 5.12: General molecular structure of polyimide.

A 3 by 3 tile 2D FTIR mosaic image of the *Entomoneis* spp. cell was dominated by absorption in loop pixels (Figure 5.13). Only the SiO and Amide I absorbances from the diatom frustule had significant spectral contrast from the polyimide loop.

A stacked display of a selection of pixels from along a line going though the image

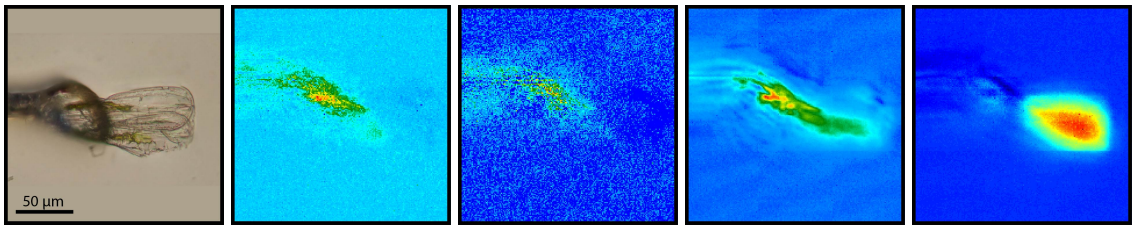

Figure 5.13: Visible and processed 2D FTIR images of the *Entomoneis* spp. cell. **(A)** Visible light image **(B to E)** FTIR image data (3 × 3 tile mosaic, 192 × 192 pixels, 64 scans) false-colour processed for the baseline-corrected area under spectral peaks.

(Figure 5.14A) shows that though some pixels have a nominal appearance (Figure 5.14B) with high spectral constrast (high and low absorbance, colour-scaled red and blue) others have scatter and baseline elevation. This is rendered in Figure 5.14C as reddish-orange vertical swaths of high absorbance with little spectral contrast.

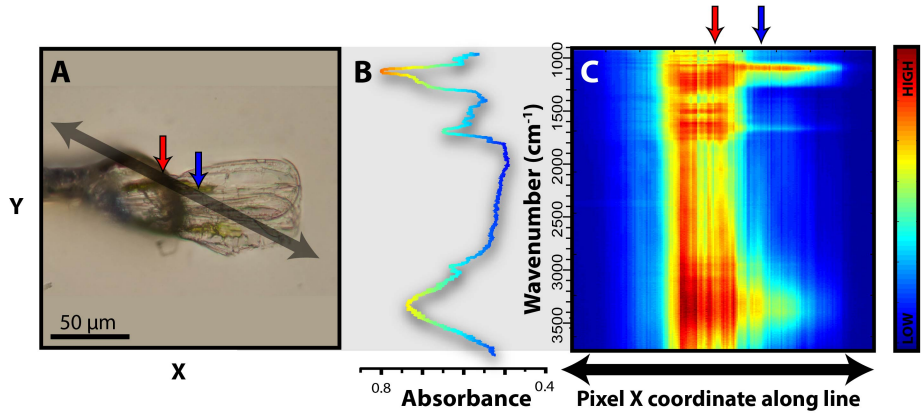

Figure 5.14: Selected pixels along a diagonal line through the image of the *Entomoneis* spp. cell. **(A)** Visible light image of the cell with the location of selected pixels marked by a black double headed arrow. The red and blue arrows point to the location of the spectra in Figure 5.11.The data at the pixel marked by the blue arrow is displayed as **(B)** a single spectrum false-color processed for absorbance (not integrated). The absorbance is also plotted on the horizontal axis. The spectrum is turned 90° for ease of comparison to **(C)** the stacked spectra from all of the selected pixels false-colour processed for absorbance (intensity at a wavenumber, not integrated) with one spectrum per column of colour.

In 3D FTIR images the Amide I band was associated with the cell. The polyimide band at 1740 cm^{-1} was co-localized with the microloop (Figure 5.15). The strong absorbance of the polyimide spectrum of the loop dominated the 3D images.

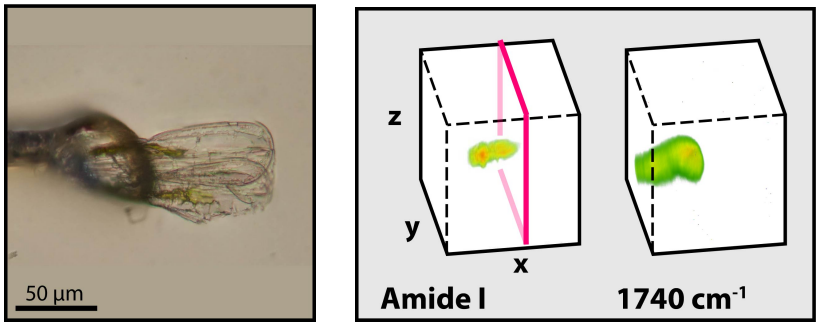

(A) Visible **(B)** FTIR

Figure 5.15: Thermal source FTIR tomographic mosaic imaging of *Entomoneis* spp. A single cell mounted on a polyimide microloop is shown in **(A)** a visible light image of the location where a tomography data set (3 × 3 tiles, 64 views, $\Delta\theta$ = 5.4°, 8 scans per view) was acquired. All parts of the visible light image were captured in the FTIR image. Reconstruction using back-projection (iRadon) generated **(B)** a voxelated FTIR image processed for integrated intensity of Amide I band and a polyimide band at 1740 cm^{-1}. The pink box indicates the position of the axial slice in Figure 5.17. Adapted from Findlay et al. (2017).

As with the other species of diatom examined, the visibly green pigmented area corresponded to locally increased absorbance in the CH stretching region of the FTIR pixel spectra. The voxels with the highest absorbance in the CH stretching region were located within the volume defined by the SiO absorbance (Figure 5.16).

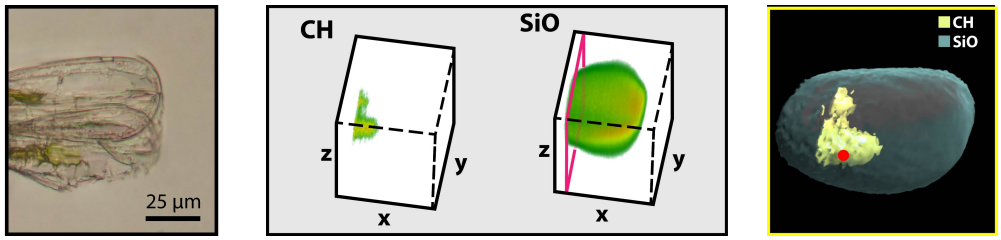

(A) Visible **(B)** Voxelated **(C)** Isosurfaces

Figure 5.16: Tomographic reconstruction of the endmost region of the *Entomoneis* spp. cell. **(A)**. The part of the visible light image of the cell and loop where a FTIR tomographic data set was acquired. The image was processed for the baseline-corrected area under the CH and SiO bands and false-colored for display as **(B)** voxels and **(C)** isosurfaces. Adapted from Findlay et al. (2017).

Closer inspection of voxel spectra from an axial cross-section revealed two volumes with elevated CH stretching absorbance (Figure 5.17A). The two volumes were located within larger volumes with elevated Amide I and SiO bands, as shown in Figure 5.17B and

C, respectively. The Amide I was found in a core region within a larger lobed SiO volume.

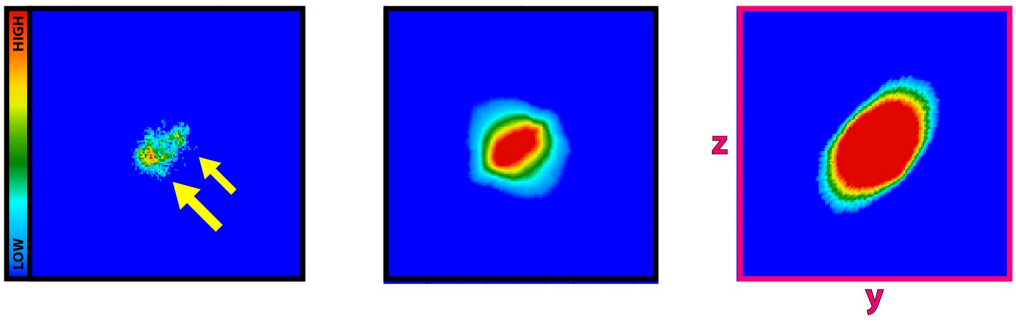

(A) CH **(B)** Amide I **(C)** SiO

Figure 5.17: An axial cross-section (yz) processed for baseline-corrected integrated absorbance of **(A)** the CH stretching region, **(B)** the Amide I band and **(C)** the SiO band. Yellow arrows (CH) show two spatially resolved local maxima. Pink box indicates positioning relative to the location marked in Figure 5.15 (SiO). Adapted from Findlay et al. (2017).

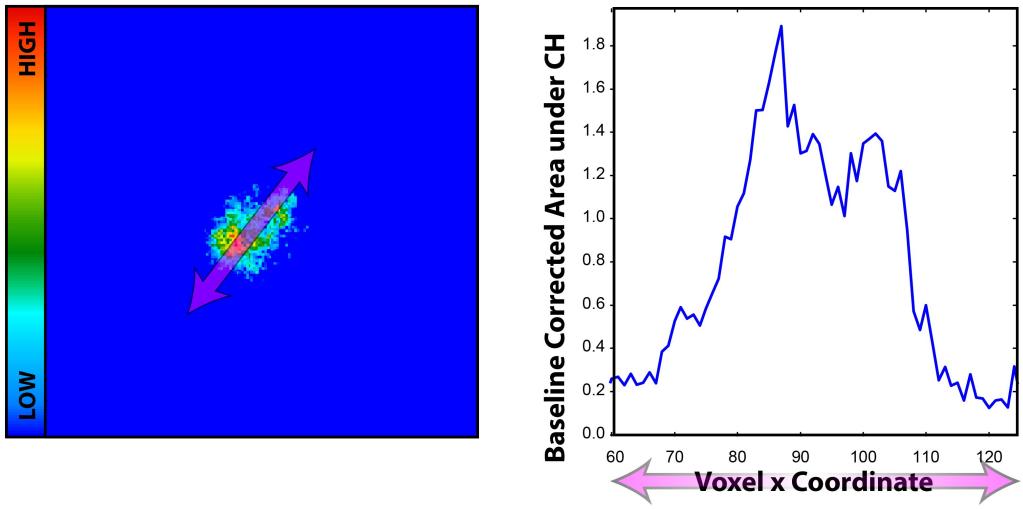

(A) Position **(B)** Profile

Figure 5.18: Selected voxels through a diagonal line through the axial slice. **(A)** The position of the line relative to the axial slice marked with a pink double headed arrow. **(B)** Plot of the integrated and baseline-corrected CH stretching region for the selected voxel spectra along the diagonal line.

The two volumes with increased CH stretching absorbance were obliquely positioned from one another in the image captured. One volume was larger than the other. Voxel

spectra were extracted from the image along a line slanting through the two volumes (Figure 5.18A). The spectral features were typical of diatom spectra viewed before; however, with the *Entomoneis* spp. cell image, the spectra had slight variation in trans-axial planes. The maximum absorbance of the smaller volume was 27% larger than the local minimum absorbance in the C-H stretching region (Figure 5.18B).

5.4 Discussion

The separation of superimposing structures is one reason why tomographic images are chosen over their conventional 2D counterparts. The overlapping positions of the cells in the tangled clump in Figure 5.1 would make them ineligible for analysis via the 2D FTIR imaging technique described by Pogorzelec et al. (2017). The specific targets in that paper were chosen partially because the diatoms were nicely separated from one another facilitating area analysis with FTIR images.

Separation is not simply a matter of dilution. Tangled clumps of cells are typical of diatoms as they secrete sticky extracellular polymeric substances in order to firmly adhere to each other and to the Arctic sea ice, and prevent themselves from being washed away by ocean tides. Other forms of diatoms deliberately aggregate as a means to sink to the seabed (Round et al., 1990).

The polyimide microloops served as a useful tool for untangling the cells gently. The larger *Entomoneis* spp. and the smaller *Nitzschia* spp. cells all fit nicely on the microloops (Figure 5.2).

The random tilt of the oblong cells upon mounting means that they must be moved in order for them to lie parallel to the axis of rotation during the acquisition of a tomographic data set. The prototype tomography accessory fully accommodated the tilt and had sufficient degrees of freedom for alignment (Figure 5.4).

The acquisition of data from cells with a good corresponding visible light image was prioritized. It is theoretically possible to image the overlapping cells that have collapsed back into segments and then separate out the cells in 3D using the tomographic method. It is true that this would depend critically on the resolution of the images. However, the isolated endmost *Nitzschia frigida* cell (Figure 5.3) had an unobstructed appearance under visible light, and clear green regions within the cell. The chloroplasts were identifiable by their green chlorophyll-containing mix of pigment. Such cells provided suitable targets for

the comparison of diatoms from different levels of snow cover.

Absorbance in the Amide I band and CH stretching region is expected in the FTIR spectrum of diatoms, due to the presence of proteins and lipids, respectively (Figure 5.5). It is also unsurprising that the chloroplast pixel spectra have stronger absorbance in the CH stretching region in pixels that correspond to green visible pigment. The chloroplasts are the photosynthetic organelles specialized for the photosynthetic activity of the diatoms. Notably, they contain thylakoids, membrane-bound structures embedded in the chloroplast stroma that stack to form granum. The photosynthetic pigments are embedded directly in the thylakoid membrane of the chloroplast, thus the green pigment and high CH signature should be co-located. Thylakoid membranes also contain integral membrane proteins (Kirk, 1994). The absorbance in the Amide I region (Figure 5.6) is consistent with this information.

The main advantage of utilizing the noise-reducing property of back-projection is in the speed of good quality data acquisition. Fewer scans means that less time is spent on data acquisition. The S/N of the spectral data increases with the square root of the number of scans co-added. In effect, the back-projection of the pixel spectra had the effect of co-adding spectral signals from the 82 different angles, resulting in the cancellation of random noise values and increasing the S/N. The results shown here were congruent with noise-canceling reconstructions performed earlier on simulated data in Section 3.1.3. The speed advantage to using a low number of scans is especially important, given the number of images that need to be acquired to form a tomographic data set. Brilliant light from synchrotron-source FTIR microtomography has very good S/N with a low number of scans, and so this noise-reducing effect is perhaps not as critical with that source of IR light.

Once acquired and processed, the 3D reconstructions of 6 *Nitzschia frigida* cells yeilded voxel spectra (Figure 5.9) and 3D FTIR images (Figure 5.8) consistent with their 2D FTIR imaging counterparts. The tomographic high and low snow depth ratios (Table 5.2) are a counterpart to the 2D data that form part of the larger trend of vernal bloom values by

Pogorzelec et al. (2017). The greater snow depth correlated to less light, preventing its transmission through the ice. The reduction of the illumination of the chloroplasts reduced photosynthetic processes, such as lipid synthesis (Pogorzelec et al., 2017).

The *Entomoneis* spp. cell is the largest single cell[2] that has been caught on a loop (Figure 5.10) and imaged with FTIR tomography as of the date of this thesis. The stage mosaicing built into the Agilent system seamlessly stitched together the total of 9 FPA tiles[3] required to cover the area of the cell. The most problematic image artifacts stemmed from the scatter from the polyimide microloop, which was apparent in the 2D FTIR images (Figure 5.13) and pixel spectra (Figure 5.11, Figure 5.14). There are alternative polymers, such as teflon, that have a lower refractive index and could be more compatible with mid-infrared absorption than polyimide. Such a loop was created for the study of buccal cells, in Chapter 6.

The loop is present in tomographic reconstructions (Figure 5.15), but is nicely hidden where the cell hangs off of it (Figure 5.16). Unlike the end cell in the fibrous colony of *Nitzchia fridgida*, the globular morphology of the *Entomoneis* spp. cell meant that only a part of the cell could hang free of the loop.

The trans-axial plane of the 3D image that is free of the polyimide microloop is informative (Figure 5.17). The two groups of pixels with absorbance in the CH stretching region are resolved (Figure 5.18).

5.5 Conclusions

Though no truly new information was gleaned regarding the biology of diatoms, the reproduction of results from 2D imaging lends credence to the FTIR microtomography technique. The imaging of diatoms constitute the most extensive correlated 2D and 3D FTIR imaging performed to this date. The volume of diatom cells, in picolitre units, was uniquely

[2]The cell is not part of a tissue.

[3]The 3D data takes at least 9 times the time to acquire as another 3D counterpart with single tiles sampled at the same angular interval.

measurable in 3D images, and not their 2D counterparts previously published by Pogorzelec et al. (2017).

Otherwise, the chloroplasts are highly co-localized with lipid and protein absorbance in 3D FTIR images. The spectral profiles, features and absorbance ratios of diatom tomographic images are congruent with the results by Pogorzelec et al. (2017). The 3D images have the same spectral profiles, features and absorbance ratios. Both show that at this location and time of harvest in the Arctic, high snow depth influenced the biomass content of *Nitzschia frigida* diatom cells adhering to ice below.

The tomography accessory employs the built-in mosaicing features of a FTIR imaging system and was able to align the elongated diatoms to an axis of rotation, enabling tomography of entire cells. Combining FTIR tomography with mosaicing permitted the imaging of the largest cell to date. In images of a larger diatom, two chloroplasts are distinctly separable using the tomographic technique. These chloroplasts are among the first sub-cellular structures to be resolved in 3D with FTIR tomography.

Chapter 6. Imaging of Human Buccal Cells

6.1 Background

Buccal cells are ubiquitously available to scientists. One needs only to look to their own inner cheek for a sample[1] of these human epithelial cells. These cells are naturally shed from the human oral mucosa into the saliva. Unlike other cell types, these human buccal epithelial cells can be harvested from saliva with minimal effort using procedures that are non-invasive, and self-administered sampling (Lindfors and Lundberg, 2002; Vining et al., 1983).

The buccal cell nucleus is readily viewable upon inspection with a standard visible microscope. This cellular organelle houses the chromosomes, and therefore most of the human genetic information in the form of deoxyribonucleic acid (DNA). The DNA is in complex with a variety of proteins that organize it into a compact chromosomal form. Campbell et al. (2005)

In general, nucleus volume and morphology are important to many fields. For example, in oncology it is well known that cancer cells can have uncontrolled replication of DNA, resulting in nuclei that are larger than they would be in healthy cases. The diagnosis and grading of cancerous tissue is based on nuclear size: observed nuclear area (ONA) and the ratio of nucleus area to cytoplasmic area (N/C). An unusually large nucleus is associated with precancerous dysplasia as well as with malignant cells. Other diseases are marked by micro-nuclei, an additional nucleus that is smaller in volume than normal (Jevtić et al., 2014).

Unstained cells exhibit low visible contrast, with some cellular structures that cannot

[1]The regulation of biosafety protocols for experiments involving microscopy of healthy samples of normal human buccal epithelial cells is not strict. These kinds of experiments are performed in middle schools. The handling of one's own fresh cells is particularly safe and free of risk for inter-person disease transmission.

be easily detected without the use of stains. However, the nucleus of the cell is round and centered in the cell, and its prominent appearance can be detected with visible microscopy (Schrek, 1936). FTIR imaging provides high contrast spectrochemical images using native signals from buccal cells, without the requirement for stains. Buccal cell nuclei can be detected in 2D using absorbances of protein and phospate groups, which are elevated in these organelles (Romeo et al., 2006).

Human buccal epithelial cells and their nuclei have never before been imaged with FTIR tomography and pose a novel imaging target for this emerging technique. As of the date of this thesis, the only other human sample that has been imaged with FTIR tomography is a shaft of hair (Martin et al., 2013), which is acellular. Here, polyimide microloops and a fluorocarbon macroloop developed in-house were used. The application of FTIR tomography toward detecting a cellular nucleus in three spatial dimensions is demonstrated.

6.2 Methods

6.2.1 Sample Preparation and Imaging

A series of 5 rinses (30 seconds each) with consumer-grade, alcohol-containing mouth-wash (Listerine^{TM}) were applied in order to reduced the number of viable mouth bacteria[2]. Droplets of saliva were deposited on glass microscope slides. Cells were collected from the droplets onto loops.

Cells were mounted on polyimide microloops as per Section 5.2.2. Teflon^{TM} fishing line (100% fluorocarbon, 0.3 mm diameter) was drawn over flame to a final diameter of $\sim$50 μm and then twisted into $\sim$3 mm diameter loops. The loops were glued to wire shafts, for ease of manual manipulation and so they would fit in the sample holder of the tomography accessory. Droplets of saliva were captured on the loops and immediately loaded in the tomography accessory. The saliva dried into a film just prior to infrared imaging.

[2]The alcohol in the mouthwash kills some bacteria.

A cell from each of the two holders types was imaged without delay to preserve any polyunsaturated fatty acids (PUFA) that might exist (Stitt et al., 2012). FTIR data sets from the cell on the polyimide microloop and the fluorocarbon macroloop holder were acquired with the Mark I and II prototypes of the tomography accessory, respectively, using the Section 2.1 protocols. The polyimide loop holding one cell was larger than the FPA area and required a mosaic consisting of 3 vertical tiles to be acquired. A 3-tile mosaic was also acquired of another buccal cell on the fluorocarbon macroloop, for comparison.

Table 6.1: Buccal epithelial cell and holder peak parameters.

Band	**Peak Centre** (cm^{-1})	**Left**		**Right**	
		Baseline, LB (cm^{-1})	**Edge,** LE (cm^{-1})	**Baseline,** RB (cm^{-1})	**Edge,** RE (cm^{-1})
Amide I	1652	1682	1682	1618	1618
P=O symm. str.	1050	1100	1100	1000	1000
C=C (Polyimide)	1488	1546	1517	1468	1448

6.3 Results

A fresh unstained sample of human buccal epithelial cells in saliva had no obvious distortion to cell morphology (Figure 6.1). The contrast was low in visible images, but was sufficient for the cell nucleus to be discerned. The nucleus in Figure 6.1 was not perfectly spherical and had an oval shape.

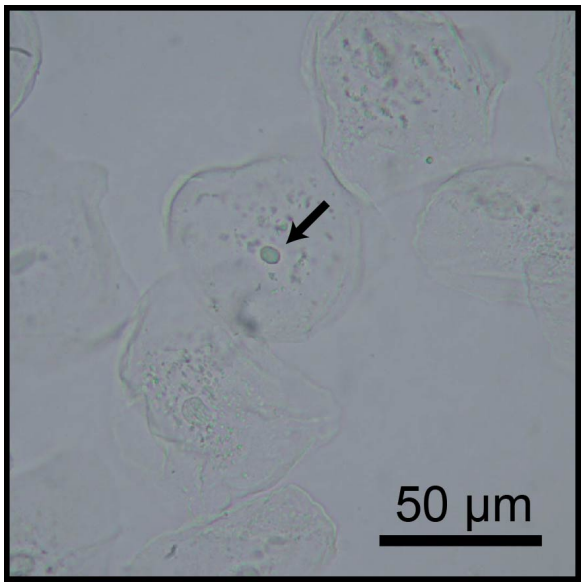

Figure 6.1: Visible image of unstained buccal cells in a droplet of saliva on a glass microscope slide. The black arrow indicates the position of one in-focus nucleus.

6.3.1 Buccal Cell Held by a Polyimide Microloop

2D FTIR Images

A cell was visible as globular low-contrast shape sitting on the orange polyimide microloop. Its nucleus was not readily apparent (Figure 6.2).

An image of this cell was captured in a 3 tile FTIR mosaic. The Amide I peak at 1652 cm^{-1} was co-located with the cell, while the peak at 1488 cm^{-1} was co-located with the polyimide loop.

The peak parameters were non-specific for cell and loop when used without baseline

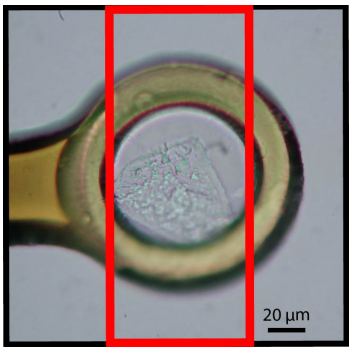

Figure 6.2: Visible image of a human buccal cell mounted on a MiTiGen^{TM} polyimide microloop. The red box indicates the part of the imaging subject captured in 2D and 3D spatially resolved FTIR images.

correction. There was particularly low contrast between the cell and loop (Figure 6.3A) in the processed image produced for the 1652 cm^{-1} peak without baseline correction (Figure 6.3B). In contrast, the baseline corrected integration parameters were specific for cell and loop (Figure 6.3C).

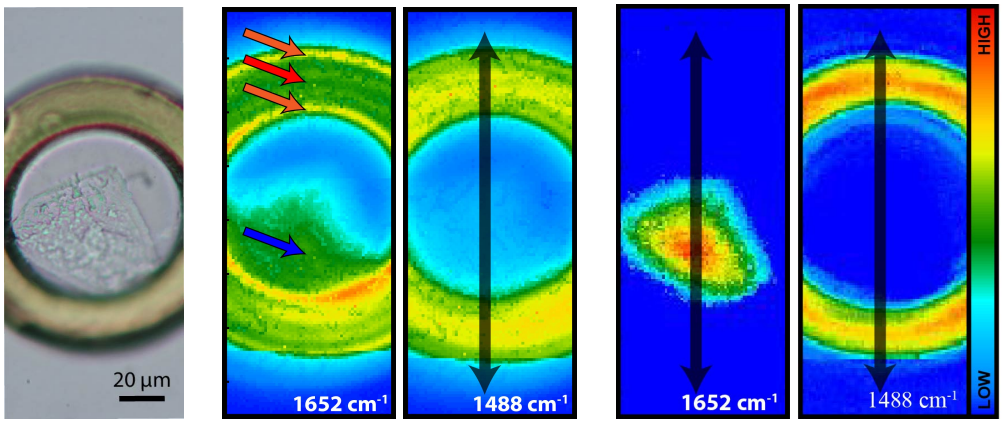

(A) Visible **(B)** Uncorrected **(C)** Baseline corrected

Figure 6.3: Pixelated FTIR image of a single buccal cell on a polyimide microloop resolved to two spatial dimensions and false-colour processed for integration of peaks at Amide I at 1652 cm^{-1} and polyimide at 1488 cm^{-1} **(B)** without baseline correction and **(C)** with baseline correction. The double headed arrow indicates the position of a column of pixel spectra extracted for display in Figure 6.4. The coloured arrows in **B** indicate the locations of four selected pixels along the line.

The spectra shown in Figure 6.4 and 6.5 are typical for the image. The spectra from the edge of the loop had elevated baselines (Figure 6.4 and 6.5, orange arrows). The spectra

from the centre of the polyimide loop and the buccal cell had lower baselines, indicating less scatter. Interestingly, the spectrum of the polyimide loop (6.5A) still had a more obvious slope to its baseline than the spectrum of the buccal cell (6.5A). The increase in baseline value to lower wavenumbers is anomalous behavior, not fully explained by Mie scattering alone.

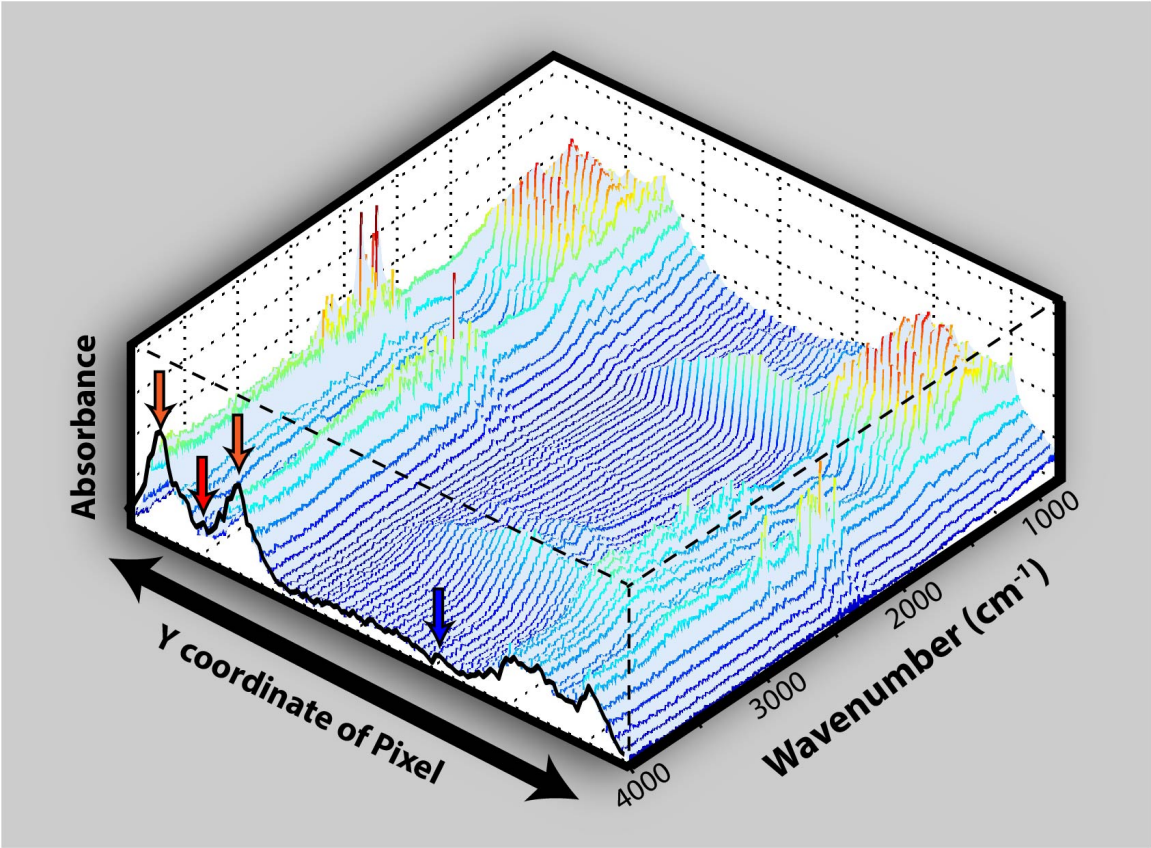

Figure 6.4: Stacked display of pixel spectra of human buccal epithelial cell on a polyimide microloop holder, extracted from a line marked in Figure 6.3. The colored arrows point to the leftmost high energy edge (black outline on left side) of four selected pixel spectra. The **red** and **blue** arrows point to a spectrum from the core of the polyimide loop and the buccal cell, respectively. The **orange** arrows point to spectra from the edges of the polyimide loop. Spectra are false-coloured for intensity of absorbance (not integrated).

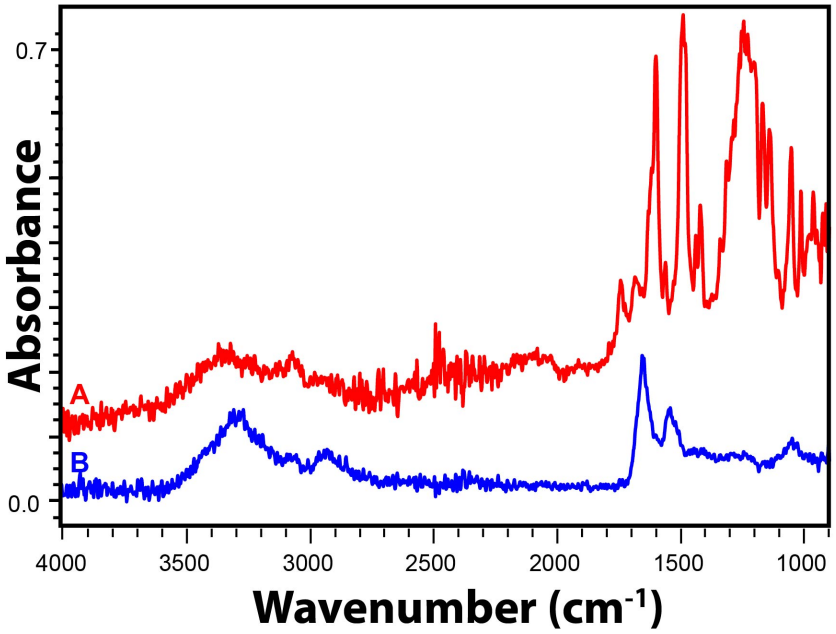

Figure 6.5: FTIR pixel spectra from locations in the FTIR image with (**A, red**) the core of the polyimide loop and (**B, blue**) buccal cell. Color corresponding arrows in Figure 6.4 indicate locations of the pixels.

3D FTIR Images

The 3D FTIR images were solid in appearance when the baseline correction was used during data processing, and had a hollow appearance when the correction was not applied (Figure 6.6). It appears that the buccal cell has curved around the loop.

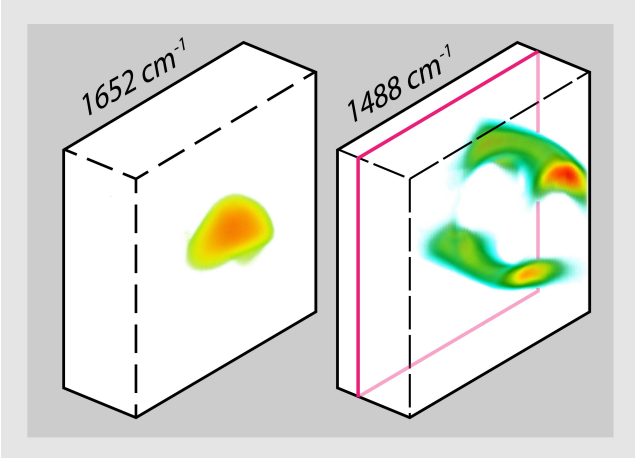

(A) Baseline corrected; solid appearance

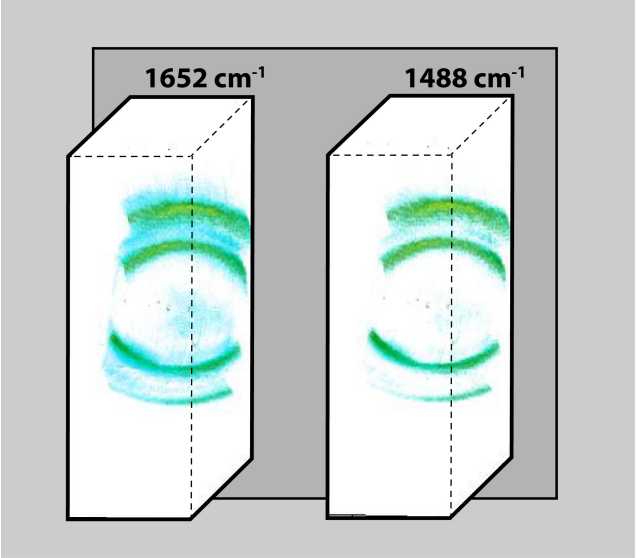

(B) No baseline correction; hollow and gossamer appearance

Figure 6.6: FTIR Tomographic imaging (47 views, $\Delta\theta = 3.6°$, 64 $\times$ 192 pixels per view) of a human buccal cell held on a polyimide microloop. False-colour rendering of filtered back-projected image processed for integration of cell body using the Amide I band at 1652 cm^{-1} and the polyimide microloop using the band at 1488 cm^{-1} **(A)** with and **(B)** without baseline correction. Image cropped to 64 $\times$ 134 $\times$ 134 voxels, 1.1 $\times$ 1.1 $\times$ 1.1 μm^3 per voxel. The pink box in **A** indicates the axial slice extracted for display in Figure 6.7.

Selected voxel spectra from an axial cross-section show that spectral baseline elevation occurred at the edges of the polyimide microloop (Figure 6.7, 6.8, orange arrows).

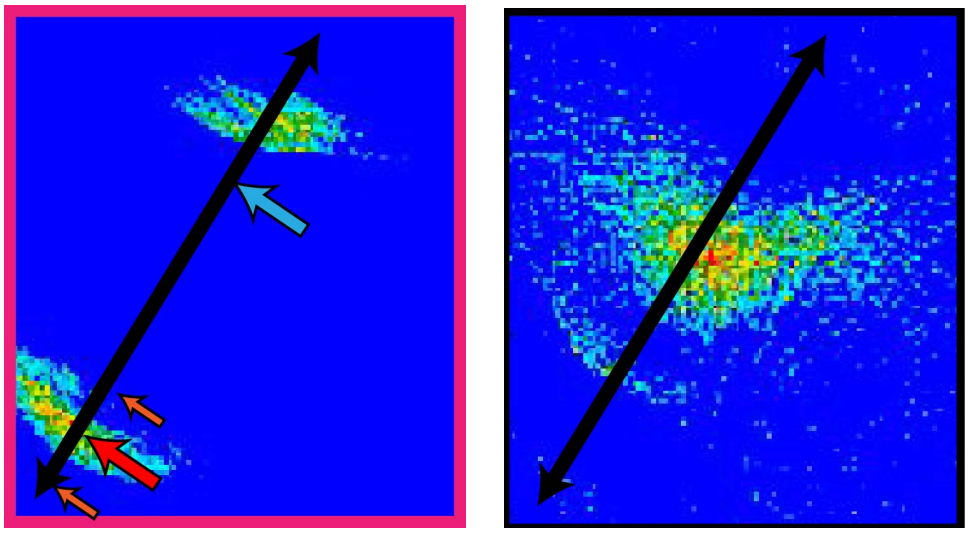

(A) 1652 cm^{-1} **(B)** 1488 cm^{-1}

Figure 6.7: Axial cross-section of 3D FTIR image of buccal cell on loop. The slice is rotated 180 ° for compatibility with Figure 6.8. Image further cropped.

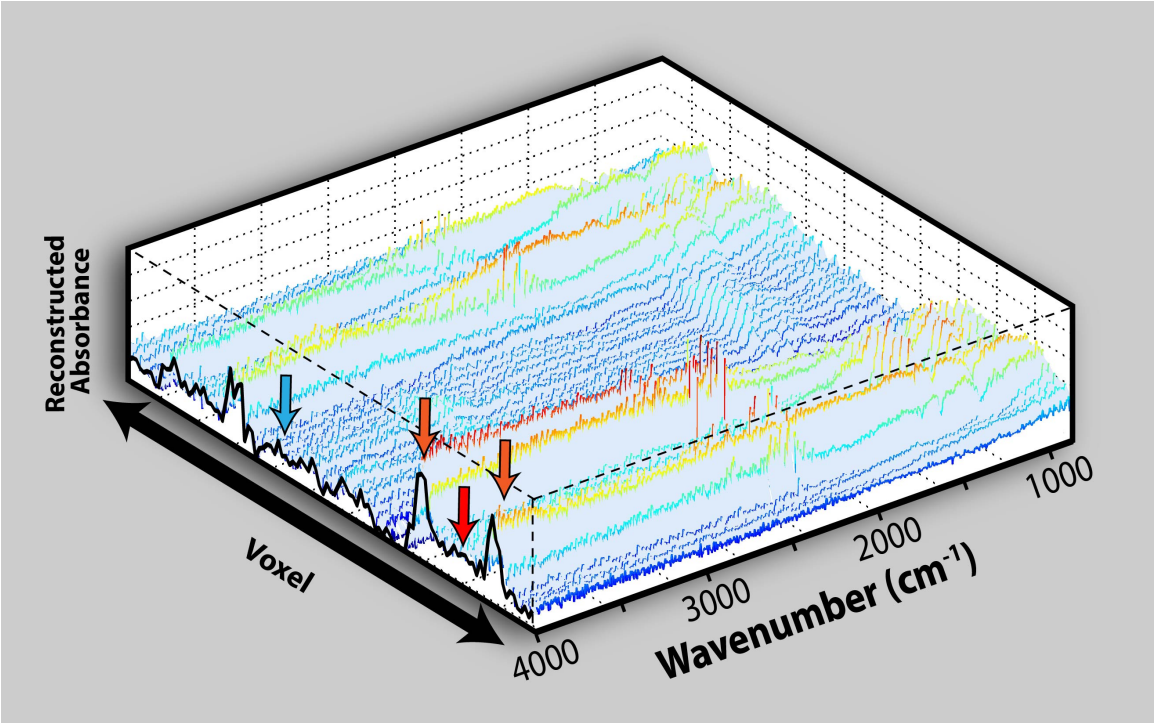

Figure 6.8: Selected voxel spectra through an axial slice of the 3D spatially resolved FTIR image of a human buccal epithelial cell on a polyimide microloop holder. Voxel spectra reconstructed with FBP. The **red** and **blue** arrows point to a spectrum from the core of the polyimide loop and the buccal cell, respectively. The **orange** arrows point to spectra from the edges of the polyimide loop. Spectra are false-coloured for intensity of absorbance (not integrated).The 2D FTIR image was rotated 180° prior to spectral export so that the small peaks from the spectrum indicated by the blue arrow are not obscured in the display.

.

The unfiltered back-projected voxel spectra had sloping baselines associated with pixel spectra from both the cell and loop (Figure 6.9). In contrast FBP voxel spectra from the cell had flat baselines (Figure 6.9Ba), and only those from the loop had sloping baselines (Figure 6.9Bb). The FBP amplified the high spatial frequency content, which resulted in increased noise in the reconstructed voxel spectra.

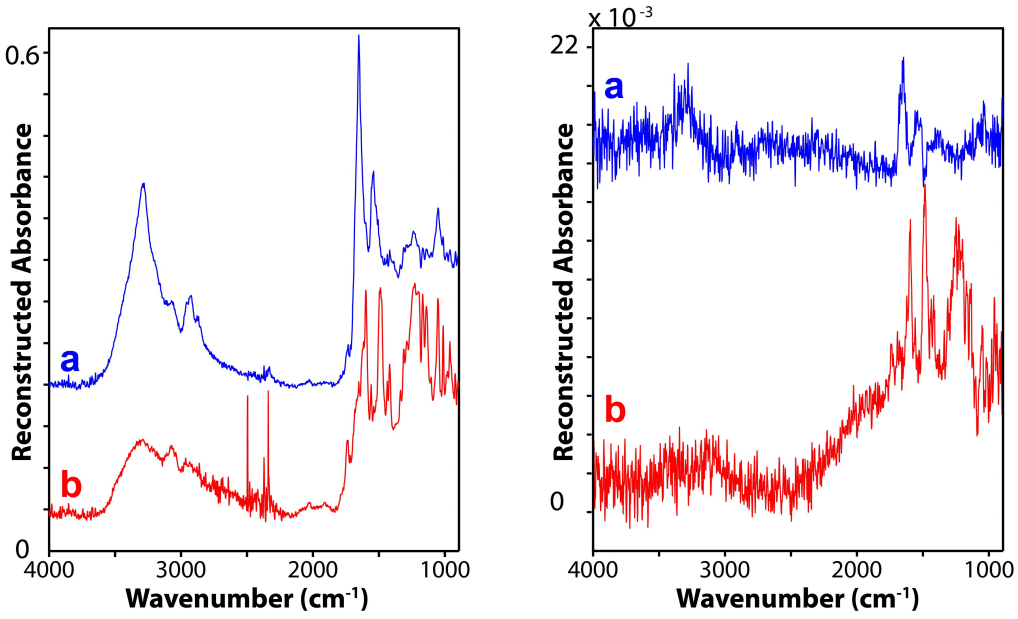

(A) Unfiltered **(B)** Filtered

Figure 6.9: FTIR voxel spectra from human buccal cell held on a polyimide microloop from Figure 6.6. Spectra reconstructed with A) unfiltered back-projection and B) FBP employing the Rak-Lam filter. Common scale, offset for clarity.

6.3.2 Buccal Cell Held by a Fluorocarbon Microloop

2D FTIR images

Buccal cells were visible in the sample of saliva prepared on the fluorocarbon macroloop (Figure 6.10A). Amide I (Figure 6.10B) and II bands (data not shown) were observed in a 2D FTIR image of a single selected buccal cell. The Amide I absorbance reached a maximum at the centre of the cell. An absorbance band at 1050 cm^{-1} arising from a P=O

symmetric stretching mode was noted in the central area of the cell, in pixels corresponding to the cell nucleus.

Pixel spectra varied across a cell. Pixel spectra from areas on the cell without nucleus (Figure 6.11A) had a lower absorbance at 1050 cm^{-1} than those with the nucleus (Figure 6.11B). Pixels from areas corresponding to the film of dried saliva that was providing physical support had very low absorbance at all wavenumbers (Figure 6.11C).

Voxelated FTIR images

The macroloop was well out of focus during tomographic data set acquisition and afforded uninterrupted 360 ° views. The Amide I band had strong absorbance throughout the cell while the 1050 cm^{-1} band was associated with voxels from the cell nucleus in the tomographic image (Figure 6.12).

The voxel spectra reconstructed with unfiltered back-projection from the volumes of the cell with and without the nucleus were similar (Figure 6.13A). The same voxels had improved spectral contrast when reconstructed with FBP (Figure 6.13B). The spectral baselines were similar but the FBP spectra from the nucleus had a larger absorbance at 1050 cm^{-1} (Figure 6.13Ba) than a voxel 7.7 μm (i.e. 7 pixels) distant, (Figure 6.13Bb, black arrow). The FBP amplified the high spatial frequency content and increased noise in the reconstructed voxel spectra.

6.4 Discussion

Though a nucleus is apparent in some buccal cells (e.g Figure 6.1) it is not in others. This could possibly be due to karyolysis, which occurs in mitotic cells as the dissolution of the cell nucleus or in dying cells as the result of enzymatic degradation of the chromatin by endonucleases (Campbell et al., 2000). Karyolysis may explain the absence of a visible nucleus in the human buccal epithelial cell mounted on a polyimide loop shown in Figure 6.2.

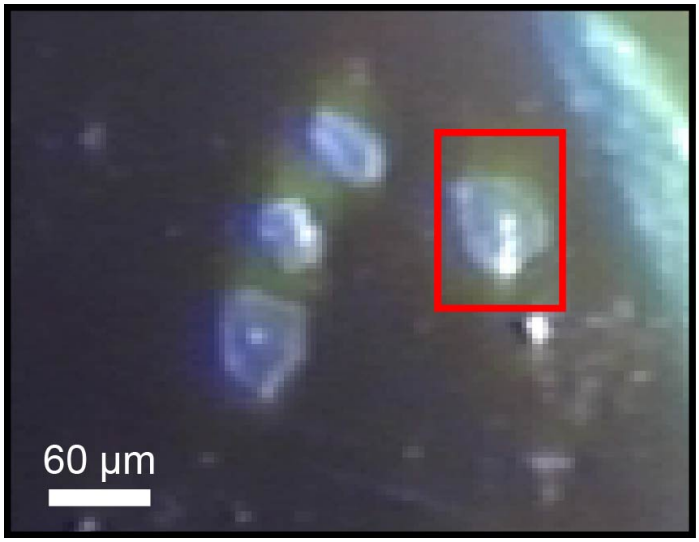

(A) Visible

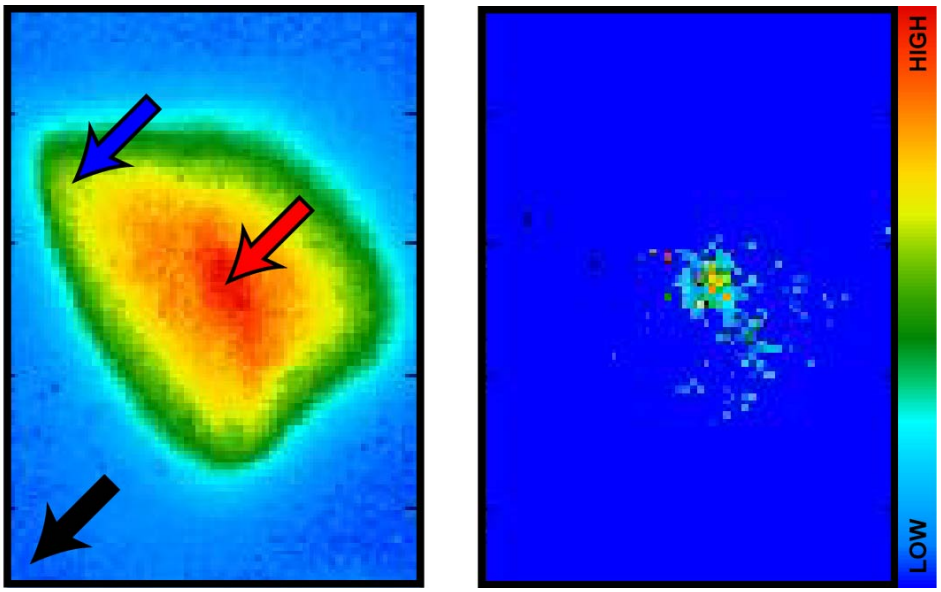

(B) 1650 cm^{-1} **(C)** 1050 cm^{-1}

Figure 6.10: 2D FTIR imaging of human buccal epithelial cells. **(A)** Visible reflectance-mode image of four buccal cells in a dried film of saliva. The red box indicates the area where a 2D FTIR image was acquired of a single cell. The image was cropped (64 $\times$ 90 pixels, 1.1 $\times$ 1.1 μm^2 per pixel) and false-colour processed for baseline-corrected integration of the **(B)** Amide I band at 1650 cm^{-1} and **(C)** the band at 1050 cm^{-1}. Colored arrows denote locations corresponding to the pixel spectra in Figure 6.11. The (**red**) arrow points to the nucleus of the cell.

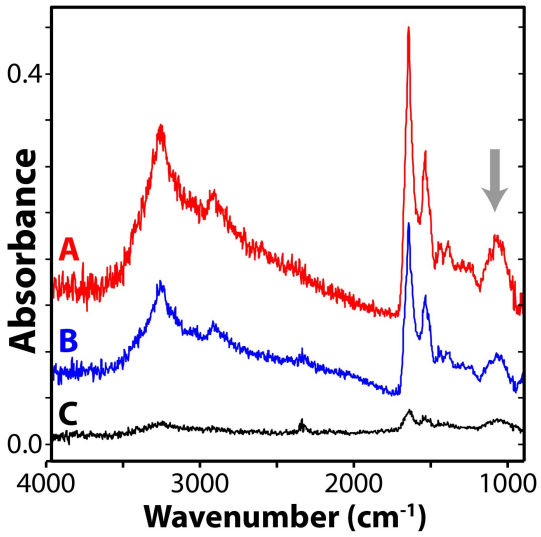

Figure 6.11: Spectra from spatially 2D FTIR images of human buccal epithelial cells. The pixel spectra were selected from locations **(A, red)** on an area of the cell with nucleus **(B, blue)** an area of the cell and **(C, black)** the saliva film holding the buccal cell in place. Common scale, offset for clarity. **Grey** arrow indicates a band of interest. Locations of spectra are marked with solid colour-corresponding arrows on Figure 6.11

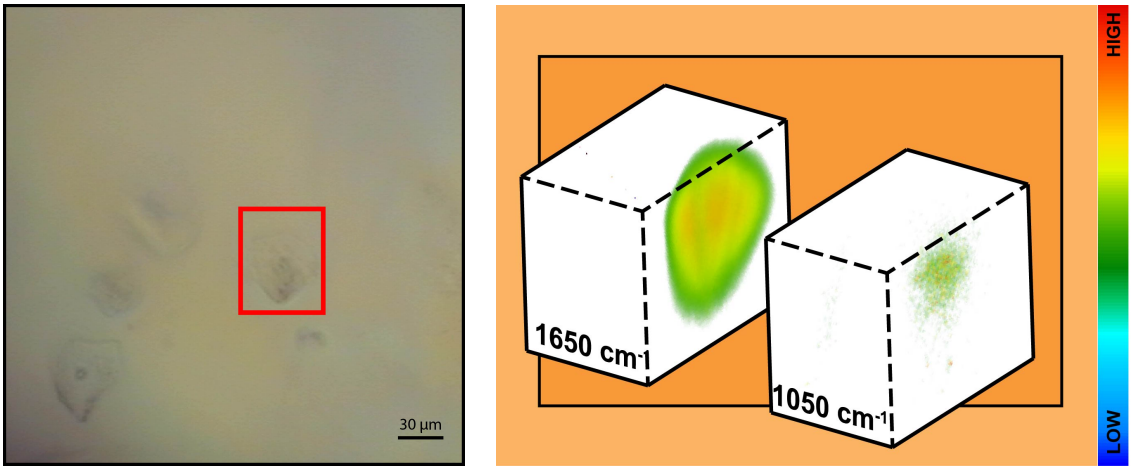

(A) Visible **(B)** FTIR

Figure 6.12: FTIR tomographic imaging of a human buccal epithelial cell suspended in a film from a fluorocarbon macroloop. **(A)** Transmission-mode visible light image. **Red** box indicates location were a FTIR tomographic data set (25 views, $\Delta\theta = 7.2°$, 3 tiles and 8 scans per view) was acquired. **(B)** A display of the reconstructed FTIR image with empty voxels at the periphery of the image cropped ($64 \times 90 \times 90$ voxels, $1.1 \times 1.1 \times 1.1$ µm^3 per voxel) for clarity.

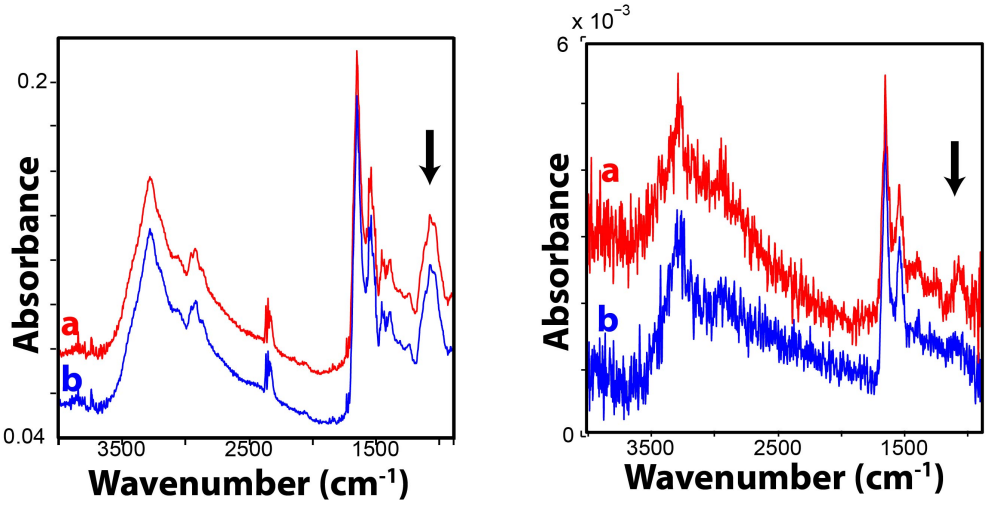

(A) Unfiltered **(B)** Filtered

Figure 6.13: Reconstructed voxel spectra from a human buccal epithelial cell held on a fluorocarbon macroloop. Spectra were back-projected **(A, Red)** without filtration and **(B, Blue)** with filtration. Voxels positioned **(a)** on the nucleus (x = 35; y = 147; z = 93) and **(b)** nearby but off the nucleus (x = 35; y = 140; z = 92). Spectra are on a common scale offset for clarity.

The buccal cell spectra were dominated by the presence of polyimide absorbances. This was true for both the 2D (Figure 6.3, 6.4, 6.5) and 3D (Figure 6.6, 6.7, 6.8, 6.9) images. The scatter and strong absorbances from the polyimide are better isolated to the loop voxels when FBP is applied (Figure 6.9). The FBP also had the effect of degrading the S/N to a disruptive degree, making it an ineffective solution for this particular image. The filter has removed some of the low spatial frequency signal at the cost of image brightness. The noise level stays the same as the signal strength decreases, causing a decrease in the overall S/N.

By comparison, the preparation of a thin film of saliva on a fluorocarbon macroloop improves FTIR tomographic imaging. The polyimide-air-interface is eliminated. The nucleus of the selected cell on the fluorocarbon macroloop is visible as the supporting saliva film is transparent to visible light (Figure 6.10A).

Proteins are found throughout the cell, thus the cell volume is well defined by the proxy Amide I band (Figure 6.10B). The nucleus of the cell is rich in phosphate groups, due to the phosphate backbone of deoxyribonucleic acid (DNA). The co-location of the phosphate

stretching band at 1050 cm^{-1} with the nucleus is attributable to the rich concentrations of DNA (Figure 6.10C, 6.11). The 3D FTIR images (Figure 6.12) and spectra (Figure 6.13) are in total agreement with their correlated 2D counterparts, but provide unique volume data.

The superior sensitivity of volume (rather than area) to size increase can be explained with Euclidean geometry. While area increases with the square of radius for a spherical object, volume increases with the cube of the radius (Figure 6.14). Nuclei are not always perfectly spherical in morphology (Thomas et al., 2009). Round, globular or ovoid objects, such as some nuclei, can have different areas depending on the angle from which they are viewed.

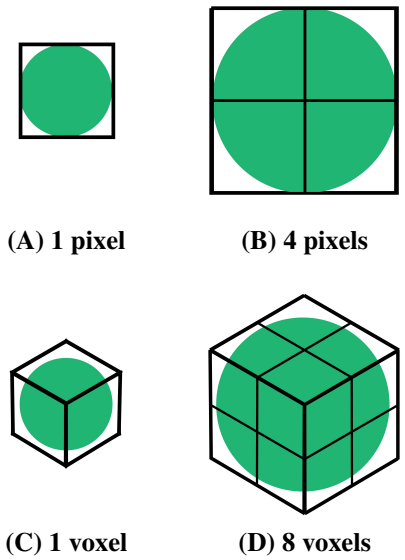

Figure 6.14: A spherical imaging subject doubles in diameter. The overlaid **(TOP, AB)** 2D and **(BOTTOM, CD)** 3D grids indicate the positions of pixels, and voxels, respectively.

6.5 Conclusions

Human buccal epithelial cells collected via non-invasive saliva collection can be measured in a non-destructive fashion, without the need for staining or other treatments that distort

morphology. A fluorocarbon macroloop holder for the cell permitted FTIR imaging without a polyimide microloop. The main advantage was the size, rather than the composition of the loop. The diameter of the loop greatly exceeded the FTIR focus, and it did not appear in the tomographic data set. Hence, unlike the polyimide microloop, it did not leave discernible artifacts in the collected images. The first 3D spatially resolved FTIR imaging of buccal cells was performed. Nuclear signatures were detected in voxels within the cell. The utilization of a filter with back-projection improved the image, but decreased the signal to noise ratio (S/N) of the voxel spectra.

Chapter 7. Thesis Conclusions

FTIR imaging is an established technique, based on fundamental principles, and the optical and chemical phenomena underlying it are well understood. Modern variations on past techniques, namely 1) the use of high magnification optics for increasing spatial resolution and 2) spatially 3D resolved microtomography, extend the resolution capabilities of classical FTIR spectroscopy.

Developments to sample preparation, image acquisition and analysis have been implemented and assessed, and have been shown to significantly improve the quality of FTIR tomographic images. The results from two functional tomography accessory prototypes suggest that there is potential for refinement of prototypes, industrial designs and a production level version of tomography accessories for infrared microscopes.

FTIR microtomography has commonalities with FTIR microspectroscopy, its mother technique. Some notable shared properties are 1) that trace quantities of sample can be captured in spectrochemical images 2) the non-destructive nature of both techniques permits further testing or correlated imaging and 3) S/N ratio can be improved through co-addition of scans. 4) Baseline correction employed in 3D FTIR, as well as 2D FTIR, de-emphasizes edge scattering in images.

However, only tomography resolves FTIR spectra along the 3rd spatial dimension. Volumes within micro-samples that are occupied by a particular macromolecular class of biochemicals (e.g. biogenic silica, fatty-acids, protein, DNA) can be detected and quantified in spatially 3D resolved FTIR images. The presence of multiple superimposing microstructures, (e.g. overlapping diatom cells) indicates that 3D FTIR images can be utilized and that FTIR images in 2D may not be sufficient.

Though validation and development of this technique is currently in an early stage, novel information about either elongated or globular micro-samples can be provided by

FTIR microtomography. FTIR tomographic imaging aided in studying the 3D nature of imaging phantoms, biological objects of interest (sea ice diatoms, spider silk, buccal cells) and related polymers (PVA, polystyrene, polyimide, teflon).

Theoretical models, simulation and experimental data suggest that samples with Beer-Lambert behavior evident in their spectroscopic signatures are relatively more compatible with the simplest non-diffractive models of tomography. Scattering is disruptive to FTIR imaging and the minimization of imaging artifacts is necessary. Scattering is inconsistent with simple models of reconstruction such as the iRadon. Obtaining optimal 3D images requires samples with matched refractive indexes across interfaces between media and low amounts of scattering, such as is the case with human buccal epithelial cells. If matching indexes are not naturally present, a coating can be applied to improve the optical properties of a micro-sample. In this thesis, quality transmission FTIR spectra from a fibre that normally scatters infrared light badly, i.e. spider silk, were acquired without physical force being applied, by employing such a coating. The double strand structure of artificial spider silk was uniquely resolvable with 3D FTIR, due to a refractive index matched coating that corrects scatter.

The buccal cell preparation demonstrated here shows that the polyimide microloop holders, a source of scattering in 3D FTIR images, can be further eliminated with the use of modified methods, e.g. a teflon macroloop sample-holder.

Overall, the FTIR micro-tomography methods that are described in this thesis are practical and realistic and accommodate or reduce scattering effects. The resources and skills required to apply infrared microtomography can be made very feasible. Further validation and experiments would allow scientists to better visualize the value of this budding technique.

Chapter 8. Future Work

Modern FTIR microscopes can capture 2D spectrochemical images in a few minutes, with resolution high enough to discern the biochemistry of cellular structures. Cutting edge advances have made 2D FTIR imaging more viable and practical as a tool for diagnostics. Globally, there is a strong drive toward creating rapid, non-invasive diagnostic tests based on 2D FTIR imaging (Byrne et al., 2015).

In contrast, 3D FTIR is not suitable for diagnostics in its current state. The hurdles that exist between the development of FTIR tomography and use in basic scientific study, much less diagnostic applications, are largely technological in nature.

The time efficiency of data acquisition is an issue that could be resolved with software-based solutions. A more robust software control of the microscope and tomography accessory is needed. Software systems with automation would save time and make tomographic imaging more accessible. Other forms of tomography use auto-focus and image recognition to determine whether the sample is aligned properly, and what adjustments are necessary. Live image recognition and processing software could prescribe calibrated adjustments of sample and facilitate the motorized centering of the sample after automated rotation. Collaboration between the FTIR tomography community and microscope software coders is highly desirable to achieve these improvements.

Further validation through phantom design and imaging is needed. Diffractive models for reconstruction exist and can be tested on simulated hyperspectral image data. The extent of the impact of scatter on FTIR reconstructions has yet to be quantified. The principal component analysis that is routinely used on 2D spectral data could be applied to FTIR tomographic data.

Increasing the S/N of the reconstructed spectra would allow a more thorough analysis by spectroscopists. The descriptions of silk by Weatherbee-Martin et al. (2016) suggests

that both β-sheet and α-helix protein secondary structure conformations should exist in the strand of quadruple-drawn artificial spider silk. These conformations are detectable in published FTIR pixel spectra Ling et al. (2011). Due to limited acquisition speed and time constraints, the reconstructed spider silk spectra in this thesis are too noisy to discern these fine details. As hydration affects the secondary structure of silk (Blackledge et al., 2009), humidity control may be required for a more thorough analysis of beta-sheet and alpha-helix content using FTIR signatures.

Future practical imaging of biochemicals would employ normalization of data to concentration standards. The ability to resolve concentrations of biochemicals to the inside of cells may be useful to cultured samples of diatoms and other microorganisms. Growth media with varying concentrations of nutrients would be resolved to the outside of the cell. A long-term, time-lapsed tomographic study of a live non-locomotive microorganism in growth medium has not yet been undertaken, but is conceivable.

Thin films of different materials, such as agar, could be used to hold cells and provide nutrients. While saliva was appropriate for use with buccal cells, there are other infrared-transparent materials that can be employed. Thin films of salt could be useful in cases where dehydration is not an issue. Micro-samples of the desired imaging subject would be mixed into a salt solution. Droplets would then be allowed to dry into thin films on loops or be scraped off clean flat surfaces to form flakes. These could then be mounted to the tomography accessory and held in the field-of-view for imaging.

The teflon macroloop is an example of an alternative method for mounting cells for tomographic imaging, but others are possible. Suction from a micro-pipette could be used to select and hold a particular cell for imaging. Most of the cell would hang free off the end of the pipette, if a light suction was employed and an infrared transparent material could be used to build the pipette, such as chalcogenide described by Martin et al. (2013).

The term FTIR microtomography encompasses tomography achieved via FTIR imaging, but there exist related infrared techniques that do not employ the Fourier Transform,

such as quantum cascade laser (QCL) source IR microspectroscopic imaging (Bassan et al., 2014). QCL light-sources are more brilliant than globar light sources and may increase the speed of data acquisition for tomography. These experiments have not been performed as of the date of this thesis, but could be used to achieve 'infrared microtomographic' imaging, rather than 'FTIR microtomographic' imaging.

Variations and combinations of imaging subject preparations and imaging techniques have yet to be conceived. From the plurality of infrared tomography methods that will exist in the future, it is clear that those which are direct, simple, efficient and effective will become seminal.

Chapter 9. Appendices

(A) Before **(B) After**

Figure 9.1: Visible images of cryosectioned 3xTg murine brain tissue sample before and after light contact with Ge crystal. Due to their raised topology, only the plaque cores (dark and circular in image) have adhered to the crystal, causing their removal after the Ge crystal is lifted off when ATR FTIR imaging is completed.

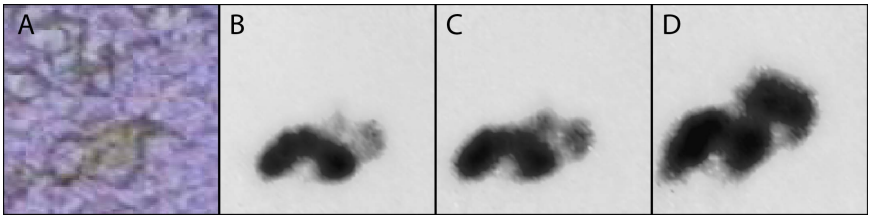

Figure 9.2: a) Visible light image of cryosectioned brain tissue from the cortex of a 3xTg mouse-model of Alzheimer's disease. A low-contrast creatine deposit in the unstained tissue is visible before ATR imaging. Thermal source ATR FTIR false-colour images of integrated creatine band at 1305 cm^{-1} for b) light c) medium d) heavy contact with Ge ATR crystal. Distribution of creatine distorts with increase in contact. Black indicates high and white indicates low peak area. All FTIR images displayed with equal color mapping and integration parameters.

Table 9.1: Tomography accessory prototype Mark I parts.

Rotation System Hardware			
No.	Component	Supplier	Description
1	Stepper Motor	Pololu	An electric motor. (NEMA 8-sized, 200 steps per rev.) rotating its output shaft between a plurality of different angular positions about the output axis.
2	Arduino Uno - R3	SparkFun	A microcontroller for the operation of the stepper motor. Widely used, compatible with open source software.
3	L293D Motor Drive Shield	BangGood	For Arduino Duemilanove Mega / UNO. Has a bi-polar H-bridge circuit. Compatible with the Adafruit code repository.
4	USB Cable A to B	SparkFun	Cable to connect Arduino Uno to computer. 6 Foot.
5	Wall Adapter	Sparkfun	Alternative power supply for the Arduino UNO. 9VDC 650mA.
5	Computer	Dell	Can power and send instructions to the Arduino UNO via USB. Also has connection to the FTIR microscope.
Adjustment Assembly			
No.	Component	Supplier	Description
1	Mounting Hub	Polulu	Allows attachment of the motor to a U50-P. Aluminum, low momentum during spinning. 5 mm. Universal.
2	U50-P Ultima Platform Optical Mount	Newport	fitted with high tpi screws for fine translation and rotation. 1.0 x 1.0 in., (3) 80-TPI Allen-Keys
3	0.70 mm collet	Pentel	Salvaged component from Pentel P207 Mechanical Drafting Pencil, 0.7mm. . Hold sample mounted on wire. Reusable, firm grip, no adhesive req. Short arm length means less sample wobble with vibration.
4	Screws	Sparkfun	Phillip Head (M3 x 12mm, 3 pack). Fasteners to secure the mounting hub to the motor.

Table 9.2: Tomography accessory prototype Mark II parts.

Rotation System Hardware			
Index No.	Component	Supplier	Description
1	Stepper Motor	Pololu	An electric motor. (NEMA 8-sized, 200 steps per rev.) rotating its output shaft between a plurality of different angular positions about the output axis.
Sample Holding and Alignment Hardware			
Index Number	Component	Supplier	Description
1	Universal Mounting Hub	Polulu	See Table 9.1 for part description.

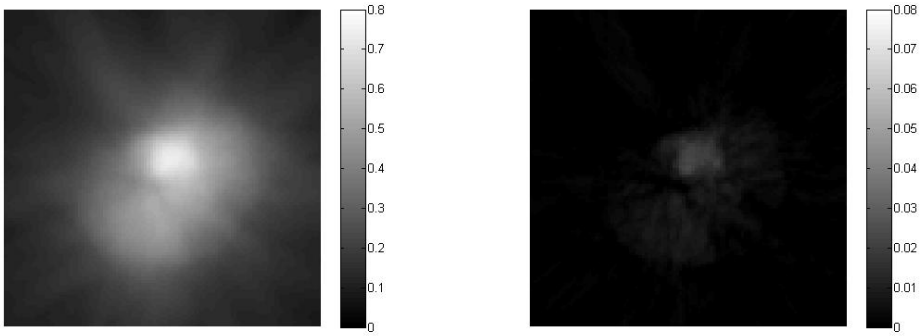

(A) Unfiltered. **(B)** Filtered.

Figure 9.3: Results of **A)** back-projection and **B)** filtered back-projection of simulated objects (100 views, $\Delta\theta = 1.8°$) when projected tomographic data set has $\pm 5000\%$ of a step angular error.

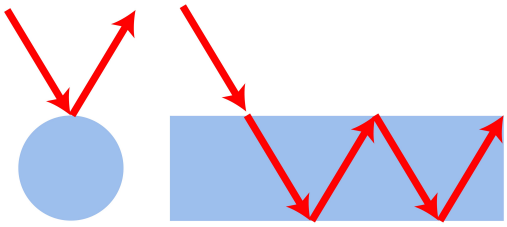

Listing 9.1: Matlab Code Snippet – Retrieve wavenumber list

```
function [ WN ] = getWNfromHDR(  )
%GETWNFROMHDR A function that retrieves the wavenumber axes information
%from the ENVI header files of exported FTIR data.
    header = uigetfile('*.hdr'); %find file with the header extension
    info1 = envihdrread(header); %get the header information from  file
    %trim brackets off of the info
    str1  = info1.wavelength;
    str1 = regexprep(str1, '{', '');
    str1 = regexprep(str1, '}', '');
    %convert the info to numbers
    WN = str2num(str1);
    %if the WNlist is upsidedown, fix it by flipping
    if verifyWNlist(WN) == 0
    disp('Flipping wavenumbers.');
    WN = flipud(WN); %flip here
    end
end

function [WNlistAnswer ] = verifyWNlist( WN )
%VERIFYWNLIST A function that checks whether the list of wavenumbers
%is ordered from lowest to highest.
    WNlistAnswer = 1;
    if WN(1) < WN(end)
    WNlistAnswer = 1;
    else
    error('IntImage:ParameterProblem', ...
        'your wavenumbers are ordered from largest to smallest.');
    WNlistAnswer = 0;
    end
end
```

9.1 Procedure for Data Set Acquisition

1. Initialize the FTIR spectrometer, microscope, FPA, stage controller and data acquisition computer as per the manufacturers instructions.
2. Install the tomography accessory.
    - Unscrew and remove the stage plate from FTIR microscope.
    - Place the plate screws in a secure container
    - Move the stage all the way to the left with the joy stick of the stage controller.
    - Clamp the tomography accessory to the stage.
    - Use a USB-A to USB-B cable to connect the micro-controller of the tomography accessory to the data acquisition computer.
3. Install an empty sample holder on the tomography accessory.
    - Pick up object with tweezers by the sample holder
    - Retract the outer sleeve of the tip of the tomography accessory.
    - Insert holder into tip.
    - Release the sleeve.
4. Perform a coarse position alignment.
    - Swing the 4x objective lens into place
    - Perform the steps in §9.2
5. Load a mounted sample onto the tomography accessory.
    - Pick up a sample mounted on wire using tweezers.
    - Perform step 7 parts b,c,d, and e.

    NOTE: The sample must be secure, with no visible wobble or looseness.
6. Perform a fine position alignment.
    - Swing the 4x objective lens into place
    - Perform the steps in §9.2
    - Swing the 15x Swarzchild objective lens into place
    - Repeat the steps in §9.2
7. Move sample out of the way
    - translate stage toward and sample toward the top of the microscope FOV (joystick up).
    - Stop when FOV is clear.

8. Perform FTIR microscope calibration as per manufacturers instructions.

   NOTE: For microscope calibration: Use transmission mode, and high magnification method files and settings. Do not change focus. LN2 tank may require top-up.

9. Acquire and save an FTIR background image. NOTE: Use more background scans (e.g. 1024 scans) than you normally would for use with signal co-addition data sets with few scans (e.g. 8 scans per view).

10. Move sample back into place

    - Joystick down
    - Stop when sample is centred in the FOV.

11. Confirm alignment is ok.

    - Rotate sample
    - View rotation under visible light
    - If sample does not stay centred, repeat step 6.

12. Prepare computer for the acquisition of a tomography data set.

    - Arrange windows such that multiple programs visible on screen.
      - Res. Pro.
      - Arduino IDE
      - Windows explorer window with subfolder for tomography files
      - Window with AutoHotKey file
    - Prepare the data acquisition subfolder.
      - Create an empty subfolder for the data files
      - Delete or remove any numbered files in the format '#.dat'
    - Prepare the Res. Pro program
      - Set the Res. Pro Experimental folder to be the data acquisition folder.
      - Select imaging setup
      - Set up the acquisition of what will be one view of the tomography. data set. Specify the number of scans, boost mode, spectral resolution, etc.
      - Abort the acquisition immediately after it starts. NOTE: The aborted acq. will cause this version of Res. Pro. to store the parameters.
      - Close all sub-windows in Res. Pro.

13. Start the macro script for automated Resolutions Pro data set acquisition.

    - Execute Autohotkey file. ('*.ahk', §9.4)

14. Monitor the data set acquisition process.

- for Res. Pro errors
- for changes to the Videum Capture live visible window
- to ensure proper focus at intervals

NOTE: Avoid extra mouse movement or keyboard input to the computer when the data acquisition is in progress in order to prevent error messages. If Res. Pro. crashes or a data file is skipped, the macro script must be reset.

9.2 Sample Position Alignment

1. View the empty sample holder wire under the microscope.
2. Open Videum Capture program and Arduino IDE on the data acquisition computer.
3. Maximize window to full screen.
4. Use joystick to move the target object to the centre of the box marked on the screen in previous step.
5. Enter the serial command '180' into the Arduino IDE. Sample will turn 180 degrees.
6. Note the new position.
7. Use the joystick to move the target object to the point between the new position and the centre of the box.
8. Use an Allen wrench on the tomography accessory to move the target object to the centre of the box.
9. Repeat steps 4 to 8 until target object stays on the centre of the screen when rotated 180 degrees.
10. Rotate 90 degrees.
11. Repeat steps 4 to 8 until target object stays on the centre of the screen when rotated 180 degrees.
12. Repeat all steps as needed until sample is fully aligned to the axis of rotation of the tomography accessory motor.

9.3 Arduino Uno Sketch

Listing 9.2: Arduino Uno Sketch For Tomography Accessory

```
// Requires the AFMotor library
// (https://github.com/adafruit/Adafruit-Motor-Shield-library)
```

```
#include <AccelStepper.h>
// And AccelStepper with AFMotor support
// (https://github.com/adafruit/AccelStepper)
#include <AFMotor.h>

// Stepper motor has 200 steps per revolution
AF_Stepper Stepper1(200, 2);

boolean running1 = false;
int turningstate = LOW;
long previousMillis = 0; // stores time
long interval = 5000; // millisecond interval betweeen steps
long setcount = 0; // step count
int num_steps_per_interval = 3; //5.4 degree interval.
int max_num_intervals = 100; // maximum number of steps
int motor_speed = 2;

//runs when first powered up
void setup() {
  Serial.begin(9600);
  Serial.write("Power On\n");
  Stepper1.setSpeed(motor_speed);  // Set motor 1 speed
  running1 = false;
}

void loop()
{
  unsigned long currentMillis = millis();

  if (Comp("m1 on") == 0) {
    //the user typed in the text "m1 on"
    Serial.write("Motor 1 -> Online\n");
    //enable motor holding torque by
    //stepping forwards, CCW
    Stepper1.onestep(FORWARD, DOUBLE);
    //and stepping backwards, CW
    Stepper1.onestep(BACKWARD, DOUBLE);
  }
  if (Comp("m1 off") == 0) {
    //the user typed in the text "m1 off"
    // stop rotation and turn off holding torque.
    Stepper1.release();
    Serial.write("Motor 1 -> holding torque released. \n");
  }
  if (Comp("180") == 0) {
    //the user typed in the text "180"
    //command motor to perform a 180 degree turn CCW
    Serial.write("Motor 1 -> 180 degree turn\n");
    Stepper1.step(100, FORWARD, DOUBLE)  ;
  }
  if (Comp("-180") == 0) {
    //the user typed in the text "-180"
    //command motor to perform a -180 degree turn, CW
    Serial.write("Motor 1 -> -180 degree turn\n");
```

```
    Stepper1.step(100, BACKWARD, DOUBLE)  ;
  }
  if (Comp("90") == 0) {
    Serial.write("Motor 1 -> 90 degree turn\n");
    Stepper1.step(50, FORWARD, DOUBLE)  ;
  }
  if (Comp("-90") == 0) {
    Serial.write("Motor 1 -> -90 degree turn\n");
    Stepper1.step(50, BACKWARD, DOUBLE)  ;
  }
  if (Comp("Go") == 0) {
    running1 = true;
    previousMillis = currentMillis;
    setcount = 0;
    Serial.write("Go!\n");
  }
  if (Comp("Stop") == 0) {
    running1 = false;
    setcount = 0;
    Serial.write("Stop! (User requested) \n");
  }
  if (Comp("Step") == 0) {
    Serial.write("Motor 1 -> Perform one turn\n");
    Stepper1.onestep(FORWARD, DOUBLE);

  }
  if (Comp("-Step") == 0) {
    Serial.write("Motor 1 -> Perform one turn\n");
    Stepper1.onestep(BACKWARD, DOUBLE);
  }
  if (Comp("Set parameters") == 0) {
    setparameters();
  }
  if (Comp("IntervalSteps") == 0) {
    Serial.write("Motor 1 -> Perform one interval turn\n");
    Stepper1.step(num_steps_per_interval, FORWARD, DOUBLE);
    setcount = setcount + 1;
    Serial.print("IntervalSteps.  Count: ");
    Serial.print(setcount);
    Serial.print(". STEP ");
    Serial.print(num_steps_per_interval);
    Serial.print(" TIME(S).");
    Serial.println("");
  }
  if (Comp("IntervalSteps") == 0) {
    Serial.write("Motor 1 -> Perform one interval turn\n");
    Stepper1.step(num_steps_per_interval, FORWARD, DOUBLE);
    setcount = setcount + 1;
    Serial.print("IntervalSteps.  Count: ");
    Serial.print(setcount);
    Serial.print(". STEP ");
    Serial.print(num_steps_per_interval);
    Serial.print(" TIME(S).");
    Serial.println("");
```

```
  }
  if (Comp("-IntervalSteps") == 0) {
    Serial.write("Motor 1 -> Perform one interval turn in reverse\n");
    Stepper1.step(num_steps_per_interval, BACKWARD, DOUBLE);
    setcount = setcount - 1;
    Serial.print("IntervalSteps.  Count: ");
    Serial.print(setcount);
    Serial.print(". REVERSE STEP ");
    Serial.print(num_steps_per_interval);
    Serial.print(" TIME(S).");
    Serial.println("");
  }
  if (Comp("Reset count") == 0) {
    setcount = 0;
    Serial.println("Count reset.");
  }
  Serial.flush();
  if (running1 == true) {
    if (currentMillis - previousMillis > interval) {
      previousMillis = currentMillis;
      setcount = setcount + 1;

      Serial.print(setcount);
      Serial.print(". running -> STEP ");
      Serial.print(num_steps_per_interval);
      Serial.print(" TIME(S).");
      Serial.println("");
      Stepper1.step(num_steps_per_interval, FORWARD, DOUBLE)  ;
    }
  }
  if (setcount == max_num_intervals) {
    running1 = false;
    Serial.write("Stop!  (count done)  \n");
    setcount = 0;
  }
}

void setparameters () {
  Serial.println("\n Set Parameters.");

  //Prompt User for input
  Serial.println("Enter millisecond interval between rotations: ");
  //Wait for user input
  while (Serial.available() == 0) { }
  //Read user input into interval
  interval = Serial.parseInt();

  //Prompt User for input
  Serial.println("How many rotational intervals? ");
  while (Serial.available() == 0)  { }
  //Read user input
  max_num_intervals = Serial.parseInt();

  //Prompt User for input
```

```
  Serial.println("How many steps per interval? ");
  while (Serial.available() == 0)  { }
  //Read user input
  num_steps_per_interval = Serial.parseFloat();

   Serial.println("What motor speed?");
  while (Serial.available() == 0)  {  }
  motor_speed = Serial.parseInt();
  Stepper1.setSpeed(motor_speed);

  //Print out nicely formatted summary.
  Serial.print("\n ");
  Serial.print("interval: ");
  Serial.print(interval);
  Serial.print(" milliseconds. \n ");

  Serial.print("max_num_intervals: ");
  Serial.print(max_num_intervals);
  Serial.print(". \n ");

  Serial.print("num_steps_per_interval: ");
  Serial.print(num_steps_per_interval);
  Serial.print(". \n ");

  Serial.print("motor speed: ");
  Serial.print(motor_speed);
  Serial.print(". \n");
  Serial.println("");
}

// character comparison subroutine
char Comp(char* This) {
  char data [21];
  int number_of_bytes_received;
  while (Serial.available() > 0) // Serial will not be read unless
  { //  there is data input
    // read bytes (max. 20) from buffer, untill <CR> (13).
    // store bytes in data. count the bytes recieved.
    number_of_bytes_received = Serial.readBytesUntil (13, data, 20);
    // add a 0 terminator to the char array
    data[number_of_bytes_received] = 0;
  }
  bool result = strcmp (data, This);
  // strcmp returns 0; if inputs match.
  // http://en.cppreference.com/w/c/string/byte/strcmp
  if (result == 0)
  { return (0); } // Characters match
  else
  { return (1); } // Characters do not match
} //end of character comparison subroutine
```

9.4 AutoHotKey Script

Listing 9.3: AutoHotKey Script

```
;TOMOGRAPHIC DATA SET ACQUISITION SCRIPT - AutoHotKey
;For use with UofM Agilent FTIR data acquisition computer.

#NoEnv ; Compatibility with future AutoHotkey releases.
 #Warn ; Enable warnings to assist with detecting common errors.
SendMode Input; Superior speed and reliability.
;#NoEnv ; Performance and compatibility with future AutoHotkey releases.
#SingleInstance force ; Only have one instance running at a time

viewNumber := 1 ; start with the first view
Loop, 100 ; Do the following for each of 100 viewing angles
{
     Gosub, stepAccessory ; Command the tomo accessory to step forward
     Gosub, startFTIR ; Start acquisition of FTIR data in Res Pro
     Gosub, waitforacq ; Wait for the acquisition of FTIR data files.
     Gosub, saveFTIR ; Save the data files.

     Gosub, waitforprocessing ; Allow Res Pro to process the data.
     Gosub, exportENVI ; Export the data to ENVI format
     Gosub, closeFiles ; Close data files open in Res Pro
     viewNumber := viewNumber + 1 ; Iterate to the next view number
}
return ; Finish after 100 repeats.

; SUBROUTINES

stepAccessory:  ;subroutine that causes the tomo accessory to step
     WinActivate COM6 ;Activates the COM6 window
     Send IntervalSteps ;enters the text 'IntervalSteps' into com6
     Sleep, 1000
     Send {Enter}
return

startFTIR:
     ;Start acquisition of FTIR mosaic
     WinActivate Resolutions Pro ;Activates the res pro window
     Send !c
     Send i
     Send r
     Sleep, 2000
     WinWaitActive, Imaging
     sleep 100
     Send !n
return

waitforacq:
```

```
     sleep 5000
     WinWaitActive, Image Acquisition
     WinWaitNotActive, Image Acquisition
return

saveFTIR: ;Save FTIR mosaic
     Sleep 5000
     WinActivate Save As
     Send %viewNumber%
     Send {Enter}
     Sleep, 5000
     Send {Enter} ;close the Centerburst may be invalid msgbox
return

waitforprocessing:
     Sleep, 10000
     processingwindow = %viewNumber%.dat
     WinWait,Resolutions Pro, %processingwindow%
return

exportENVI: ;export to envi
     WinActivate Resolutions Pro ;Activates the res pro window
     Send !f
     Sleep, 100
     Send e
     Sleep, 100
     Send e
return

closeFiles: ;close the file
     Send !f
     Sleep, 100
     Send l
     Sleep 500
     Send {Enter} ; do not save changes to the files.
         ;close the message box that asks for this;
return
```

9.5 Summary of Silk Manufacturing Protocol

Fibre manufacture by Nathan Weatherby-Martin took place in the laboratory of Prof. Jan Rainey (Dalhousie University, Nova Scotia) with methodology modified from that published by Weatherbee-Martin et al. (2016). Artificial spider silk was produced using a core domain consisting of a repetitive 200 amino acid sequence motif (W) found in aciform spidroin of *Argiope trifasciata*, as described previously by Xu et al. (2012). Recombi-

nant H_6-SUMO-W_3 was constructed as contiguous genes in a modified pET32 plasmid, expressed and cleaved using SUMO protease before undergoing reverse HIS-tag purification. The tag-free W_3 protein was used as a dope for wet-spinning. A dope comprising 10% (w/v) W_3 in 60 % trifluoroacetic acid (TFA) / 20% 2,2,2-trifluoroethanol (TFE) / 20% H_2O (v/v/v) promoted shearing forces upon extrusion into a dehydrating bath and served to amalgamate the W_3 protein into a fiber. The spun fiber was spooled and underwent four rounds of manual post-spin stretching.

(A) Orientation 1. **(B) Orientation 2**

Figure 9.4: Two cylindrical objects (one gray, one blue) are physically positioned for viewing such that (A) the first cylindar is overlaid on the second cylindar or (B) the two cylindars are not blocked and have optimal contrast from each other.

References

Alavi, Z. (2015). *Hyperspectral Tomographic FTIR Imaging Using Two Illumination Geometries for Polymer Phantoms*. PhD thesis, University of Wisconsin-Milwaukee.

Atkins, P. and de Paula, J. (2007). *Physical Chemistry*. W. H. Freeman.

Bailey, D. L., Townsend, D. W., Valk, P. E., and Maisey, M. N. (2005). *Positron emission tomography*. Springer.

Barrett, H. H. and Swindell, W. (1996). *Radiological imaging: the theory of image formation, detection, and processing*, volume 2. Academic Press.

Bassan, P., Byrne, H. J., Lee, J., Bonnier, F., Clarke, C., Dumas, P., Gazi, E., Brown, M. D., Clarke, N. W., and Gardner, P. (2009). Reflection contributions to the dispersion artefact in ftir spectra of single biological cells. *Analyst*, 134(6):1171–1175.

Bassan, P., Weida, M. J., Rowlette, J., and Gardner, P. (2014). Large scale infrared imaging of tissue micro arrays (tmas) using a tunable quantum cascade laser (qcl) based microscope. *Analyst*, 139(16):3856–3859.

Berry, K. J., Johnston, J. E., and Mielke Jr, P. W. (2014). A chronicle of permutation statistical methods. *Springer International Publishing, Cham. doi*, 10:978–3.

Bhargava, R. and Levin, I. W. (2008). *Spectrochemical analysis using infrared multichannel detectors*. John Wiley & Sons.

Blackledge, T. A., Boutry, C., Wong, S.-C., Baji, A., Dhinojwala, A., Sahni, V., and Agnarsson, I. (2009). How super is supercontraction? persistent versus cyclic responses to humidity in spider dragline silk. *Journal of Experimental Biology*, 212(13):1981–1989.

Byrne, H. J., Baranska, M., Puppels, G. J., Stone, N., Wood, B., Gough, K. M., Lasch, P., Heraud, P., Sulé-Suso, J., and Sockalingum, G. D. (2015). Spectropathology for the next generation: Quo vadis? *Analyst*, 140(7):2066–2073.

Campbell, N., Reece, J., and Meyers, N. (2005). *Biology*. Pearson Education Australia.

Campbell, N. A., Mitchell, L. G., Reece, J. B., and Taylor, M. R. (2000). *Biology: concepts & connections*. Benjamin/Cummings, 11 edition.

Chan, K. A. and Kazarian, S. G. (2012). Correcting the effect of refraction and dispersion of light in ft-ir spectroscopic imaging in transmission through thick infrared windows. *Analytical chemistry*, 85(2):1029–1036.

Cole, J. H., Dowthwaite, J. N., Scerpella, T. A., and van der Meulen, M. C. (2009). Correcting fan-beam magnification in clinical densitometry scans of growing subjects. *Journal of Clinical Densitometry*, 12(3):322–329.

Cota, G. F. and Smith, R. E. (1991). Ecology of bottom ice algae: Ii. dynamics, distributions and productivity. *Journal of Marine Systems*, 2(3-4):279–295.

De Gussem, K. (2009). Gstools. MATLAB Central File Exchange, MathWorks, Natick, MA, USA. Retrieved Aug 19th, 2009.

Deopura, B. (1999). Split fiber production. In *Polypropylene*, pages 769–775. Springer.

Eckhard, T. (2013). hyperspectral image cube slicer. MATLAB Central File Exchange, MathWorks, Natick, MA, USA. Retrieved September 16th 2013.

Egan, C., Jacques, S., Wilson, M., Veale, M., Seller, P., Beale, A., Pattrick, R., Withers, P., and Cernik, R. (2015). 3d chemical imaging in the laboratory by hyperspectral x-ray computed tomography. *Scientific reports*, 5:15979.

Findlay, C., Morrison, J., Mundy, C., Sedlmair, J., Hirschmugl, C. J., and Gough, K. M. (2017). Thermal source fourier transform infrared microtomography applied to arctic sea ice diatoms. *Analyst*, 142(4):660–669.

Findlay, C., Wiens, R., Rak, M., Sedlmair, J., Hirschmugl, C., Morrison, J., Mundy, C., Kansiz, M., and Gough, K. (2015). Rapid biodiagnostic ex vivo imaging at 1 μm pixel resolution with thermal source ftir fpa. *Analyst*, 140(7):2493–2503.

Findlay, C. R. J. and Gough, K. M. (2016). Tomography accessory device for microscopes. US Patent No. US20160266363 A1.

Gallant, M., Rak, M., Szeghalmi, A., Del Bigio, M. R., Westaway, D., Yang, J., Julian, R., and Gough, K. M. (2006). Focally elevated creatine detected in amyloid precursor protein (APP) transgenic mice and Alzheimer disease brain tissue. *Journal of Biological Chemistry*, 281(1):5–8.

Gosline, J. M., DeMont, M. E., and Denny, M. W. (1986). The structure and properties of spider silk. *Endeavour*, 10(1):37–43.

Gough, K. M., Zelinski, D., Wiens, R., Rak, M., and Dixon, I. (2003). Fourier transform infrared evaluation of microscopic scarring in the cardiomyopathic heart: Effect of chronic at1 suppression. *Analytical biochemistry*, 316(2):232–242.

Griffiths, P. and De Haseth, J. A. (1986). *Fourier transform infrared spectrometry*. Wiley, New York.

Hanssen, L. M. and Zhu, C. (2002). Wavenumber standards for mid-infrared spectrometry. *Handbook of Vibrational Spectroscopy*.

Holman, H.-Y. N., Hao, Z., Martin, M. C., and Bechtel, H. A. (2010). Infrared spectromicroscopy: Probing live cellular responses to environmental changes. *Synchrotron Radiation News*, 23(5):12–19.

Imtiaz, A. (2015). *Scattering correction methods of infrared spectra using graphics processing units*. PhD thesis, The University of Wisconsin-Milwaukee.

Jennings, A. (2013). Create video of rotating 3d plot. MATLAB Central File Exchange, MathWorks, Natick, MA, USA. Retrieved April 03th 2013.

Jevtić, P., Edens, L. J., Vuković, L. D., and Levy, D. L. (2014). Sizing and shaping the nucleus: mechanisms and significance. *Current opinion in cell biology*, 28:16–27.

Jitian, S. (2011). Determination of optical constants of polystyrene films from ir reflection-absorption spectra. *Analele Universităţii Eftimie Murgu Reşiţa*, 18:41–48.

Kak, A. C. and Slaney, M. (1988). *Principles of computerized tomographic imaging*. IEEE press.

Kirk, J. T. (1994). *Light and photosynthesis in aquatic ecosystems*. Cambridge university press.

Leu, E., Søreide, J., Hessen, D., Falk-Petersen, S., and Berge, J. (2011). Consequences of changing sea-ice cover for primary and secondary producers in the european arctic shelf seas: timing, quantity, and quality. *Progress in Oceanography*, 90(1):18–32.

Liao, C., Piercey-Normore, M., Sorensen, J., and Gough, K. (2010). In situ imaging of usnic acid in selected cladonia spp. by vibrational spectroscopy. *Analyst*, 135(12):3242–3248.

Lindfors, P. and Lundberg, U. (2002). Is low cortisol release an indicator of positive health? *Stress and Health*, 18(4):153–160.

Ling, S., Qi, Z., Knight, D. P., Shao, Z., and Chen, X. (2011). Synchrotron ftir microspectroscopy of single natural silk fibers. *Biomacromolecules*, 12(9):3344–3349.

Lock, J. A. (1997). Scattering of a diagonally incident focused gaussian beam by an infinitely long homogeneous circular cylinder. *JOSA A*, 14(3):640–652.

Martin, M. C., Dabat-Blondeau, C., Unger, M., Sedlmair, J., Parkinson, D. Y., Bechtel, H. A., Illman, B., Castro, J. M., Keiluweit, M., and Buschke, D. (2013). 3D spectral imaging with synchrotron Fourier transform infrared spectro-microtomography. *Nature methods*, 10(9):861–864.

Mathar, R. J. (2007). Refractive index of humid air in the infrared: model fits. *Journal of Optics A: Pure and Applied Optics*, 9(5):470.

Mock, T. and Gradinger, R. (2000). Changes in photosynthetic carbon allocation in algal assemblages of arctic sea ice with decreasing nutrient concentrations and irradiance. *Marine Ecology Progress Series*, 202:1–11.

Nasse, M. J., Bellehumeur, B., Ratti, S., Olivieri, C., Buschke, D., Squirrell, J., Eliceiri, K., Ogle, B., Patterson, C. S., Giordano, M., et al. (2012). Opportunities for multiple-beam synchrotron-based mid-infrared imaging at IRENI. *Vibrational Spectroscopy*, 60:10–15.

Nasse, M. J., Mattson, E. C., Reininger, R., Kubala, T., Janowski, S., El-Bayyari, Z., and Hirschmugl, C. J. (2011a). Multi-beam synchrotron infrared chemical imaging with high spatial resolution: Beamline realization and first reports on image restoration. *Nuclear Instruments and Methods in Physics Research Section A: Accelerators, Spectrometers, Detectors and Associated Equipment*, 649(1):172–176.

Nasse, M. J., Walsh, M. J., Mattson, E. C., Reininger, R., Kajdacsy-Balla, A., Macias, V., Bhargava, R., and Hirschmugl, C. J. (2011b). High-resolution fourier-transform infrared chemical imaging with multiple synchrotron beams. *Nature methods*, 8(5):413–416.

Peabody, A. (1977). Diatoms in forensic science. *Journal of the Forensic Science Society*, 17(2):81–87.

Pettersen, E. F., Goddard, T. D., Huang, C. C., Couch, G. S., Greenblatt, D. M., Meng, E. C., and Ferrin, T. E. (2004). Ucsf chimeraa visualization system for exploratory research and analysis. *Journal of computational chemistry*, 25(13):1605–1612.

Pogorzelec, N. M., Mundy, C., Findlay, C. R., Campbell, K., Diaz, A., Ehn, J. K., Rysgaard, S., and Gough, K. M. (2017). Ftir imaging analysis of cell content in sea-ice diatom taxa during a spring bloom in the lower northwest passage of the canadian arctic. *Marine Ecology Progress Series*, 569:77–88.

Quaroni, L., Obst, M., Nowak, M., and Zobi, F. (2015). Three-dimensional mid-infrared tomographic imaging of endogenous and exogenous molecules in a single intact cell with subcellular resolution. *Angewandte Chemie International Edition*, 54(1):318–322.

Rak, M. (2007). *Synchrotron infrared microspectroscopy of biological tissues: brain tissue from TgCRND8 Alzheimers disease mice and developing scar tissue in rats*. PhD thesis, University of Manitoba.

Rao, S. (2014). Fraunhofer diffraction of light by a circular aperture. MATLAB Central File Exchange, MathWorks, Natick, MA, USA. Retrieved July 24th 2014.

Rattey, P. and Lindgren, A. (1981). Sampling the 2-d radon transform. *IEEE Transactions on Acoustics, Speech, and Signal Processing*, 29(5):994–1002.

Rech, E. and Arber, W. (2013). Biodiversity as a source for synthetic domestication of useful specific traits. *Annals of applied biology*, 162(2):141–144.

Romeo, M., Mohlenhoff, B., and Diem, M. (2006). Infrared micro-spectroscopy of human cells: Causes for the spectral variance of oral mucosa (buccal) cells. *Vibrational Spectroscopy*, 42(1):9–14.

Round, F. E., Crawford, R. M., and Mann, D. G. (1990). *Diatoms: biology and morphology of the genera*. Cambridge University Press.

Scheibel, T. (2004). Spider silks: recombinant synthesis, assembly, spinning, and engineering of synthetic proteins. *Microbial cell factories*, 3(1):14.

Schmidt, D. and Odland, R. (2004). Mirror-image reversal of coronal computed tomography scans. *The Laryngoscope*, 114(9):1562–1565.

Schrek, R. (1936). A method for counting the viable cells in normal and in malignant cell suspensions. *The American Journal of Cancer*, 28(2):389–392.

Seeram, E. (2015). *Computed tomography: physical principles, clinical applications, and quality control*. Elsevier Health Sciences.

Stitt, D. M., Kastyak-Ibrahim, M. Z., Liao, C. R., Morrison, J., Albensi, B. C., and Gough, K. M. (2012). Tissue acquisition and storage associated oxidation considerations for ftir microspectroscopic imaging of polyunsaturated fatty acids. *Vibrational Spectroscopy*, 60:16–22.

Stuart, B. H. (2004). *Infrared Spectroscopy: Fundamental and Applications*. John Wiley & Sons, Ltd.

Szeghalmi, A., Kaminskyj, S., and Gough, K. (2007). A synchrotron FTIR microspectroscopy investigation of fungal hyphae grown under optimal and stressed conditions. *Analytical and bioanalytical chemistry*, 387(5):1779–1789.

Thomas, P., Holland, N., Bolognesi, C., Kirsch-Volders, M., Bonassi, S., Zeiger, E., Knasmueller, S., and Fenech, M. (2009). Buccal micronucleus cytome assay. *Nature protocols*, 4(6):825.

Totir, F. (2010). Envi file reader/writer. MATLAB Central File Exchange, MathWorks, Natick, MA, USA. Retrieved July 26th, 2010.

Vining, R. F., McGinley, R. A., Maksvytis, J. J., and Ho, K. Y. (1983). Salivary cortisol: a better measure of adrenal cortical function than serum cortisol. *Annals of clinical biochemistry*, 20(6):329–335.

Weatherbee-Martin, N., Xu, L., Hupe, A., Kreplak, L., Fudge, D. S., Liu, X.-Q., and Rainey, J. K. (2016). Identification of wet-spinning and post-spin stretching methods amenable to recombinant spider aciniform silk. *Biomacromolecules*, 17(8):2737–2746.

Wiens, R., Findlay, C. R., Baldwin, S. G., Kreplak, L., Lee, J. M., Veres, S. P., and Gough, K. M. (2016). High spatial resolution (1.1 μm and 20 nm) ftir polarization contrast imaging reveals pre-rupture disorder in damaged tendon. *Faraday discussions*, 187:555–573.

Woodford, O. (2011). 3–d volume (voxel) rendering. MATLAB Central File Exchange, MathWorks, Natick, MA, USA. Retrieved December 18th, 2011.

Woodward, L. A. (1972). *Introduction to the theory of molecular vibrations and vibrational spectroscopy*. Oxford at the Clarendon Press.

Xu, L., Rainey, J. K., Meng, Q., and Liu, X.-Q. (2012). Recombinant minimalist spider wrapping silk proteins capable of native-like fiber formation. *PLoS One*, 7(11):e50227.

Zeng, G. L. (2015). Revisit of the ramp filter. *IEEE transactions on nuclear science*, 62(1):131–136.